

The Auditory Transduction Chain

Identification of the Functional Modules Involved in Sound Encoding

DISSERTATION

zur Erlangung des akademischen Grades

doctor rerum naturalium

(Dr. rer. nat.)

im Fach Biophysik

eingereicht an der

Mathematisch-Naturwissenschaftlichen Fakultät I

der Humboldt-Universität zu Berlin

von

Herrn Dipl.-Phys. Tim Gollisch

geboren am 18. September 1973 in Bad Oeynhausen

Präsident der Humboldt-Universität zu Berlin:

Prof. Dr. Jürgen Mlynek

Dekan der Mathematisch-Naturwissenschaftlichen Fakultät I:

Prof. Dr. Michael Linscheid

Gutachter:

1. Prof. Dr. Andreas V. M. Herz
2. Prof. Dr. Hanspeter Herzog
3. Prof. Dr. Bernhard Ronacher

eingereicht am: 19. März 2004

Tag der mündlichen Prüfung: 24. Juni 2004

...close to his ear, deeply, softly, like a mellow organ, but with a roughness in her voice like a grasshopper's, which rasped his spine deliciously and sent running up into his brain waves of sound which, concussing, broke.

– Virginia Woolf (*Mrs. Dalloway*)

CONTENTS

About this Thesis	1
1 Auditory Transduction	5
1.1 Sequential Processing	5
1.2 Temporal Signals	6
1.3 Resolution and Accuracy	7
1.4 Stimulus Integration	8
1.5 Mechanosensitivity	9
2 The Grasshopper Ear	11
2.1 Behavioral Relevance	11
2.2 Anatomy	12
2.3 Electrophysiology	15
2.4 Complementary Experiments	18
2.5 Comparison with the Mammalian Ear	21
3 Nonlinear Systems Analysis	23
3.1 Survey of Principle Approaches	23
3.2 Nonlinear Cascade Models	24
4 The Iso-Response Method	29
4.1 IRS – Iso-Response Sets	29
4.2 CIRS – Comparison of Iso-Response Stimuli	32
4.3 DIRS – Disequilibrating Iso-Response Stimuli	33
4.4 Conceptual Discussion	36
5 Spectral Integration	37
5.1 Relevant Stimulus Attribute	37
5.2 Three Hypotheses	38
5.3 IRS in a Two-Dimensional Stimulus Space	41
5.4 Influence of Adaptation	45
5.5 IRS in a Three-Dimensional Stimulus Space	47
5.6 Test of Model Predictions for Noise-Like Stimuli	49
5.7 Discussion of the Model	51

6	Temporal Integration	55
6.1	Spike-Triggered-Ensemble Analysis	55
6.2	IRS at Different Time Scales	60
6.3	Cascade Model for Integrating Click Stimuli	64
6.4	Temporal Characteristics of Stimulus Integration	65
6.5	Test of Predictions for Three-Click Stimuli	69
6.6	Discussion of the Experimental Approach	69
7	Generalized Cascade Model	73
7.1	Generalization of the Model to Arbitrary Stimuli	73
7.2	Derivation of Stationary Model Version	75
7.3	Derivation of Click Model Version	78
8	Separating Adaptation Sources	83
8.1	Input-Driven versus Output-Driven Adaptation	83
8.2	Assessing Input-Driven Adaptation	84
8.3	Characterizing Input-Driven Adaptation	85
8.4	Correlations with Stimulus Parameters	88
8.5	Discussion of the Experimental Approach	90
8.6	Mechanistic Foundation	91
8.7	Possible Functions	92
	Conclusion and Outlook	95
	Appendices	101
A	Electrophysiology	101
B	Solutions for the Adaptation Model	102
C	Measurement Directions for Iso-Response Sets	103
D	Least Squares Method for Fitting Iso-Response Sets	104
E	Bayesian Estimate of Hypotheses Probabilities	106
F	Shifts of the Rate-Intensity Functions	107
G	Shortcut to the Stationary Effective Sound Intensity	110
	Bibliography	111
	Summary in German – Deutschsprachige Zusammenfassung	123

Acknowledgements

This work was only possible with the help and support of many people. Most importantly, I would like to express my gratitude towards Andreas Herz for the opportunity to work in his research group, all the scientific and non-scientific discussions, the words of motivation, the support I experienced in many different ways, and the freedom to let the project evolve into sometimes unforeseen directions.

The background for performing the experiments was taught to me by Hartmut Schütze who also built the wonderfully robust experimental setup. I am very grateful to him for all his help and for sharing his knowledge on grasshoppers with me. The OEL software, which I used for controlling stimuli and data acquisition, had been developed by Jan Benda and Christian Machens. I thank them for all their explanations regarding the software as well as many concepts of data analysis and much beyond. During learning how to do experiments, I received much appreciated help from Fredrik Edin.

Many of my questions about insect physiology and behavior were answered by Astrid Franz, Matthias Hennig, Bernd Ronacher, and Sandra Wohlgemuth. I would also like to thank them for many an advice regarding the experiments and for helping me out whenever I had problems with the electrode puller. I am very grateful to Undine Schneeweiß for providing the different chemical solutions needed in the laboratory.

The ITB was a wonderful place for my scientific work. Especially, I would like to thank Susanne Schreiber and Inés Samengo for discussing with me many aspects of this thesis in particular and of life in general. To Martin Stemmler, I am particularly indebted for answering all my questions about the English language and for being a reliable source of feedback when it comes to writing manuscripts. I also very much enjoyed a great variety of discussions with Irina Erchova, Robert Gütig, Hanspeter Herzel, Richard Kempter, Christian Leibold, Raphael Ritz, Thomas Voegtlin, Laurenz Wiskott, and Christian Zemplin.

Many other people helped in shaping the line of reasoning in this work with their questions and comments. I would like to express my particular gratitude towards Maurice Chacron, Peter Heil, Georg Klump, Konrad Körding, and Idan Segev, who all spent much time discussing certain parts of this work with me. I am also very thankful to David Hansel for his hospitality, which allowed me to spend a wonderful time at the Laboratoire de Neurophysique in Paris.

Over the last few years, I enjoyed working together with a number of students whose projects and discussions have influenced my thinking and my work considerably. For this, I would like to thank Felix Creutzig, Olga Kolesnikova, Ariel Rokem, Roland Schaeffe, and Sebastian Watzl.

I am very grateful to Boehringer Ingelheim Fonds for supporting my work. Especially, I would like to thank Monika Beutelspacher, Hermann Fröhlich, and Claudia Walther for creating such a warm and personal atmosphere within the “B.I.F. family”. Last, but not least, I would like to express my deep appreciation for the support that my parents have given me throughout all these years.

Figure Acknowledgements

The permission to adapt and reproduce the following figures is gratefully acknowledged: Figure 2.2 from (Michelsen, 1971b), copyright 1971 by Springer-Verlag; Figure 2.3 from (Gray, 1960), copyright 1960 by the Royal Society; Figures 2.5, 5.1, 5.2, 5.3, 5.4, 5.5, 5.6, and 5.7 from (Gollisch et al., 2002), copyright 2002 by the Society of Neuroscience.

ABOUT THIS THESIS

While you, Reader of this thesis, work your way through these pages, amazing processes will happen in your brain. Complex patterns of electrical activity will be evoked in your nerve cells, triggered by the light reflected from the paper in front of you. These patterns will, in some abstract way, correspond to meanings, concepts, and ideas, which the author of these lines “had in mind”. Simultaneously, specialized cells all over your body will send electrical signals to your brain reporting the position and tension of the many joints and muscles in your body, thus enabling you to retain your posture while reading. And every sound reaching your ears will be translated into electrical activity, which is quickly used to determine how disturbing the sound was and whether you should divert your attention to the ringing of the telephone or the singing of the birds outside.

In fact, our nervous system constantly performs amazing tasks of receiving and processing diverse sensory information – whether we are just reading a scientific text about these processes or not. Our senses allow us to see, hear, feel, smell, taste, and thus construct an internal representation of the world around us. Every sensation begins with the conversion of external stimuli into responses of receptor cells. These form specialized interfaces between the environment and the nervous system. Receptor cells detect sensory information in various forms – light, sound, etc. – and *transduce* them into electrical signals, which form the basis of all computations in the brain. No sensory information is processed that was not picked up by a receptor neuron. If we are to understand how any nervous system acquires information about the environment, we must know what happens at this first stage where external stimuli are encoded into the “language of the brain”.

The particular demands for sensitivity, accuracy, and speed have led to a large variety of highly sophisticated sensory systems (Hudspeth and Logothetis, 2000). Yet, a common feature is the sequential signal processing in the receptor cells. The external signal initiates a sequence of several biophysical steps, which successively transform the signal’s representation and eventually lead to electrical potentials, which are passed on for higher-level processing in the nervous system. A sound stimulus, for example, causes mechanical vibrations, which lead to the opening of mechanosensory ion channels in the receptor cell’s membrane, followed by the accumulation of charge and the possible generation of an action potential. The individual steps and their interactions in such *transduction chains* shape the relationship between environmental stimuli and the responses of a receptor neuron. For understanding how receptor neurons react to sensory stimulation and how they *encode* different aspects of the environment, it therefore suggests itself to pay particular attention to the sequential processing characteristics.

With increasing knowledge about the *physical substrates* of biological systems – their molecules, cells, and anatomical composition – new emphasis has been given to questions

about the related *functional characteristics*. For example, how do individual system components contribute to the system's function such as the recognition of a particular sensory signal? Investigating these questions requires "the recognition of functional 'modules' as a critical level of biological organization" as argued by Hartwell and colleagues (1999), who distinguish between *molecular* and *modular* approaches to biology. Pursuing such a line of investigation, as Nurse (2003) points out, requires the development of new methods for "the identification, characterization and classification of the logical and informational modules that operate in cells". For a genuine understanding of the investigated systems, of course, biophysical as well as functional insights are required and need to be linked together.

This thesis deals with the encoding of sound into electrical potentials by the transduction chain in auditory receptor neurons. It is aimed at identifying and characterizing the functional steps involved in the processing of acoustic signals. Two questions stand in the center of the investigation:

1. What are the functional modules that constitute the auditory transduction chain?
2. How can we extract the characteristic features of these modules from electrophysiological experiments?

In order to answer these questions, we aim at describing the sound encoding in auditory receptor cells by a mathematical model, which is based on experimental data and yields a framework for determining the functional characteristics of the transduction chain. Particular problems investigated in this context include the questions about how auditory receptor cells integrate over the typically high-dimensional space of possible sound signals and how they reach the high temporal resolution required to encode fast temporal features of sounds.

The vulnerability of mechanical structures involved in hearing makes it difficult to access the auditory periphery directly under *in vivo* conditions. This calls for methods based on neurophysiological measurements from a remote downstream location, such as the auditory nerve, so that the ear itself remains largely undisturbed. One goal of this thesis is therefore to devise suitable methods for experimentally analyzing such data in a framework of nonlinear systems theory.

All studies in this work, experiments as well as models, are based on the auditory system of grasshoppers, a model system that combines a rich repertoire of signal-processing capabilities with a reduced complexity of the anatomical structure as compared to mammalian ears.

In Chapter 1, we begin our investigations with a survey of general questions connected to the encoding of acoustic signals. The temporal structure of sound, the concept of stimulus integration, and the sequential nature of the auditory transduction chain are highlighted, and background information concerning mechanosensitivity as the basis for sound reception is provided.

The particular characteristics of the auditory system of grasshoppers are introduced in Chapter 2. The relevance of hearing for these animals and the anatomical and electrophysiological knowledge about their auditory periphery, as relevant for this study, are summarized. This is complemented by new data from our own studies regarding some basic characteristics of temporal resolution and phase resetting.

The theoretical foundations, on which the methodological ideas of this work are based, are presented in Chapter 3. General concepts of nonlinear systems identification are explained with particular emphasis on cascade models, which are naturally linked to the study of processing chains. Temporal linear filters and static nonlinear transformations are introduced as the principal building blocks of these models.

In Chapter 4, we develop the methods used in this thesis for studying nonlinear cascades. The approach is based on combining the framework of cascade models with experimental measurements of *iso-response sets (IRS)*, i.e., sets of different stimuli that lead to the same output of the system. In particular, *Comparison of Iso-Response Stimuli (CIRS)* and *Disequilibrating Iso-response Stimuli (DIRS)* are introduced as new techniques for studying nonlinear systems.

The detailed experimental investigations begin in Chapter 5 with a characterization of spectral integration in grasshopper auditory receptor cells. The central question of this chapter concerns the identification of the relevant stimulus attribute, which is directly encoded in the cells' firing rates. The study thus connects to an ongoing debate about the proper stimuli and the threshold characterization for auditory sensory neurons. IRS measurements are used to study how different spectral contributions of a sound stimulus are combined by the neurons. This results in an accurate model description of the cells' input-output relation under stationary stimulation.

In Chapter 6, we switch from the frequency domain to the time domain and investigate temporal integration of acoustic signals. By measuring iso-response sets for different combinations of acoustic clicks, the vibration of the ear drum and the accumulation of electrical charge are identified as the relevant integration processes. Applying the CIRS method reveals integration time windows well below one millisecond for both processes, which are characterized with a precision of a few microseconds.

Chapter 7 presents a theoretical investigation of the experimentally obtained model structures. A generic cascade model is presented that captures the results obtained with stationary as well as click stimuli. The two corresponding model versions of the previous two chapters are formally derived from the more general model, and the applicability of the required mathematical approximations is discussed.

In Chapter 8, we leave the fast processes of the primary signal-transduction chain and turn to the slower dynamics of spike-frequency adaptation. Particularly, we focus on experimentally investigating the functional origin of adaptation. Application of the DIRS method reveals a substantial contribution of an adaptation component that is driven by the sensory input. This adaptation component is thus distinguished from the more common output-driven components, and the measurements are used to characterize the corresponding features of input-driven adaptation.

Finally, we conclude this work by summarizing the central findings of this study and by discussing the picture we have obtained about auditory transduction. Furthermore, an outlook is given suggesting continuative investigations of the transduction chain as well as presenting limitations and possible extensions of the new systems identification techniques introduced with this thesis. Technical details of the electrophysiological experiments, the modeling, and the data analysis are left to the appendices.

CHAPTER 1

AUDITORY TRANSDUCTION

Hearing begins with the conversion of the air-pressure fluctuations underlying sound into electrical signals. This transduction process takes place in mechanosensitive receptor cells, which are generally found in conjunction with a mechanically resonating structure. A sequence of several biophysical processes is involved in the transduction. The information about the acoustic stimulus is thus encoded into electrical signals – usually in the form of action potentials that propagate along the fibers of the auditory nerve – and sent on to higher-level processing areas of the nervous system.

In this chapter, we will highlight some of the characteristics of auditory transduction. First, we will introduce the different steps in the biophysical sequence of sound encoding. Subsequently, the temporal structure of acoustic signals will be discussed. This leads to questions regarding the temporal resolution of auditory receptor cells in order to allow encoding of fast components of acoustic signals with high temporal accuracy. The vastness of possible acoustic signals gives rise to the problem of signal integration. Finally, particular attention is paid to the mechanosensitive properties of the receptor cells.

1.1 Sequential Processing

The mechanosensory transduction is embedded in a sequence of several biophysical processes. Step by step, these processes convert the air-pressure fluctuations, which constitute sound, into a series of action potentials in the auditory nerve. Initially, the fluctuating air pressure induces oscillations of mechanical resonators such as ear drums, basilar membranes, or hair sensilla (Robeles and Ruggero, 2001; Schiolten et al., 1981; French, 1988; Robert and Göpfert, 2002). These oscillations then cause the opening of mechanosensory ion channels in auditory receptor cells (Hudspeth, 1985; Hill, 1983; Gillespie and Walker, 2001). The resulting electrical currents change the cell's membrane potential. This, in turn, activates voltage-dependent ion channels that eventually trigger action potentials. Figure 1.1 schematically depicts this *auditory transduction chain*.

The sequential nature of processing is a fundamental characteristic of all sensory transduction systems and many other signal-processing structures, and it lends itself to investigations based on models that explicitly incorporate this cascade structure. Formally, each processing step can be viewed as a module that induces a transformation of

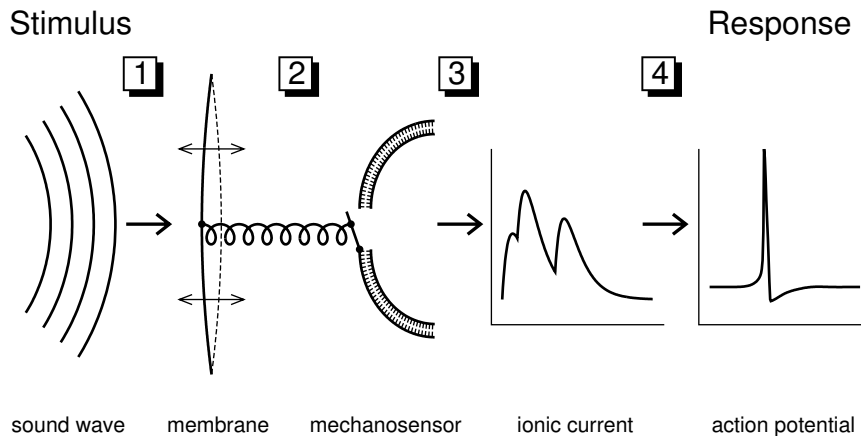


Figure 1.1: Sequential processing in the auditory transduction chain. A sequence of several steps transforms a stimulus sound wave into a neural spike response. **1. Mechanical coupling.** The acoustic stimulus induces vibrations of a mechanical membrane (basilar or tympanic membrane). **2. Mechanosensory transduction.** The deflections cause the opening of mechanosensory ion channels in the cell membrane of a receptor neuron. Many details of this transduction process are still unknown. The depicted schematic coupling follows the gating-spring model proposed for mechanosensory transduction in hair cells (Markin and Hudspeth, 1995). **3. Electrical integration.** The electrical charge accumulates at the cell membrane. **4. Spike generation.** Action potentials are triggered by voltage-dependent currents and travel down the auditory nerve. Each of these steps transforms the signal in a specific way, which may be nearly linear (as for the ear-drum response) or strongly nonlinear (as for spike generation, which is subject to thresholding and saturation). The illustrated steps may contain further sub-processes such as cochlear amplification or synaptic transmission between hair cells and auditory-nerve fibers.

the stimulus representation. Such transformations may include rectification, saturation, and temporal filtering and contain linear as well as nonlinear aspects of signal processing. As will become apparent later, such formalization of the individual processing steps can be done in a generic framework provided by nonlinear systems theory.

1.2 Temporal Signals

The input signals for auditory receptor neurons are air-pressure fluctuations that reach mechanically resonating structures. A key feature of these signals lies in the fact that most of their information is contained in their temporal structure. Whereas, for example, a visual object is primarily identified by its spatial relations and odors obtain their identity from their relative molecular composition, an auditory object, such as a spoken word, is characterized by the temporal sequence of air-pressure fluctuations. Even the information about the direction of a sound is represented in the temporal structure of the received sound stimulus; many animals rely on analyzing inter-aural time differences, i.e., the difference in arrival time of a sound at the left and right ear, to determine sound direction (Grothe and Klump, 2000). Furthermore, the information of a sound signal involves a large range of characteristic time scales. For extracting direction, composition, and meaning of a spoken word, the air-pressure waves have to be analyzed on scales from microseconds to seconds.

All this makes the auditory system particularly suited for studying the processing of *time* in nervous systems. Receptor neurons, e.g., have to be sensitive to sub-millisecond features of the sound and simultaneously transmit information reliably over seconds. How is this temporal information encoded, processed, and read out? Answers to these questions are also relevant for other sensory systems. The changing properties in a visual scene may give the nervous system information about the movement of external objects or of the organism itself. Even for the analysis of a static scene, it is suggested that active movements of the receiver (e.g., “whisking”, the active movement of rodent whiskers, and small-amplitude movements of the eye during “fixation”) enforce a temporal structure during stimulus reception, which is used for a temporal code (Ahissar and Arieli, 2001). Furthermore, in any natural, nonstatic stimulus environment, the nervous system faces a constant influx of information; sensory input therefore needs to be processed “on the fly”, while more input is being received, and must provide the relevant information “just in time” to result in a timely behavioral response.

Such considerations lead to questions about how *external time*, which carries stimulus information, is represented in nervous systems and how it corresponds to *internal time*, which is used by the nervous system itself for performing computations. These questions have received a growing amount of attention lately (Hopfield, 1996; Hopfield and Brody, 2001; Van Rullen and Thorpe, 2001; Maass et al., 2002; Hahnloser et al., 2002; Herz, 2004).

1.3 Resolution and Accuracy

Specific sounds are identified by their temporal composition. The characteristics of the receiver must therefore be suited to follow the relevant structure. When the important information lies in quick changes of the acoustic stimulus or in the exact timing of certain sound features, the receptor cells must show correspondingly high temporal sensitivity. Sound localization, echolocation, and acoustic communication often require a resolution in the millisecond range or below. Striking examples of such high sensitivity are found, e.g., in the ability of barn owls to locate sound sources with a precision that corresponds to an inter-aural time difference of few microseconds (Knudsen, 1980; Köppl et al., 2000). Similarly, to detect the small time differences in the delay of their sonar system, bats have a comparable resolution for their echolocation system (Neuweiler and Schmidt, 1993).

The ability to read out stimulus structures on such small time scales defines the high temporal resolution of auditory receptor cells. On the other hand, these cells may also show high temporal accuracy of their output by evoking precisely timed electrical responses. Often, there seems to be a natural connection between temporal sensitivity to the stimulus (the resolution of external time) and temporal accuracy of the response (internal time); after all, accurate responses are a simple way to conserve the timing information of the input signal.

An impressive example for the correspondence of resolution and accuracy is the auditory system of the parasitoid fly *Ormia ochracea*. This species relies on precise timing information on the order of few microseconds to locate its host, the field cricket *Gryllus rubens*, on the basis of the cricket’s communication calls. Correspondingly, the auditory receptor cells are found to produce remarkably reliable spikes with a jitter of only 70 μ s

(Mason et al., 2001; Oshinsky and Hoy, 2002). Similar examples of such extraordinary temporal accuracy are also found in several other auditory systems (Grothe and Klump, 2000).

Such accurate responses are noteworthy especially in the light of typical neural-membrane time constants around several milliseconds. An action potential itself has a width of about one millisecond, which often leads to the naive notion that a millisecond is the smallest relevant time scale in nervous systems. We here see that at least specialized systems reach values of accuracy far below. Intracellular recordings from isolated hair cells indicate that this is accompanied by exceptionally small membrane time constants. Measuring the low-pass-filter properties of these cells in response to sinusoidal stimulation, one can deduce that time constants lie in a range from about 0.4 to 2 ms (Russell and Sellick, 1983; Geisler, 1998).

Although an accurate output often serves to encode the input with high resolution, it is important to note that resolution and accuracy need not be connected in this way, and we may indeed find one without the other. Especially for higher-level brain structures, temporal accuracy can carry information about non-temporal stimulus aspects. A well studied example is found in the hippocampus of rats where the spikes' phase relative to internal oscillations significantly contributes to the coding of space (Jensen and Lisman, 2000). Such temporal codes may be particularly suited for solving complex recognition tasks (Hopfield, 1995).

On the other hand, high resolution may be used by neurons to read out fine structures of a stimulus, but the presence of a specific feature can still be signaled with non-accurate spikes. A simple explanation would be the occurrence of temporal jitter due to noise sources in the spike generation or propagation. The distinction between resolution and accuracy will be important when we attempt to investigate the signal-integration characteristics of a neuron on time scales smaller than that of its output accuracy.

1.4 *Stimulus Integration*

Acoustic stimuli are convenient for handling. With suitable loudspeakers, the signals can be well controlled in intensity and exactly timed. Conceptually, a single one-dimensional function (or time series in the discretized version) describing the sound pressure suffices to identify the stimulus – at least as long as the sound direction is held fixed. Yet, all constraints taken into account, the possibilities for different acoustic stimuli are still gigantic. An ordinary music CD, e.g., contains sound frequencies up to approximately 20 kHz. Loosely speaking, this means that a new sound pressure is produced every 25 μ s. Within a small fraction of a musical piece, let us say of one millisecond length, this amounts to the possibility of choosing 40 different intensity values. Given the typical CD digitization of 16 bit, each value can be chosen from 2^{16} possibilities. This amounts to the astronomical number of $2^{16 \cdot 40}$ (a number with more than 190 digits) possible acoustic signals in this one millisecond – so to speak merely a “moment” of music.

A neuron that encodes this piece of music, on the other hand, usually responds with only a single spike with limited temporal precision, often also in the range of one millisecond. Effectively, all the different acoustic signals are thus mapped onto just two different response symbols, “spike” or “no spike”. Intrinsic noise sources may smooth this classi-

fication and lead to a description of the neural output by a single spike probability. For longer observation times, the output is even more constrained due to neural refractoriness.

It is thus clear that the dimensionality of possible signals is vastly decreased when going from the space of stimuli to that of responses. This *dimensional reduction* can be viewed as a *stimulus integration*; in order to “determine an output symbol”, e.g., a firing rate or a spike probability, the neuron needs to combine several aspects (“dimensions”) of the stimulus. At the heart of this integration process lies the question which subclasses of the vast number of possible signals are encoded “as equal”, a question to which we will return when introducing the experimental approaches for studying transduction in this work.

How can we even hope to discover suitable descriptions to handle the vastness of possible input-output relations? The reason is that, in the end, not all thinkable relations are biophysically realizable. Knowledge about the principle setup of the signal processing in sensory systems thus guides our search towards models whose constituents perform fairly simple, generic, biophysically plausible functions. In the simplest scenario, the transduction machinery might be set up to extract a single physical variable out of the signal. Identifying this variable tells us what the relevant stimulus attribute is that the neuron encodes.

1.5 Mechanosensitivity

The transduction process in auditory receptor cells is mediated by mechanosensitive ion channels. These open in response to mechanical deformations such as stretch, compression, shear, or bending. The resulting influx of ionic charge leads to a change of the electric potential across the cell membrane, usually a depolarization. Many details about the functioning of these ion channels are still lacking. In most cases, their number, conductivity, and location as well as their molecular composition remain unknown. Three principal reasons seem to be responsible for the difficulties in characterizing these ion channels. First, these channels are scarce. Apparently, very few channels per cell suffice for transduction (Hudspeth, 1989; Gillespie, 1995). Second, mechanosensory transduction is fast and immediate. No second-messenger signals are involved, which could help identify the channels (Hudspeth and Logothetis, 2000; Gillespie and Walker, 2001). Third, hearing systems are delicate and vulnerable. It is often exceedingly difficult to access the transduction sites directly without damaging essential mechanical parts and interfering with natural signal transduction.

For these reasons, indirect approaches, which deduce information about the transduction process from the stimulus-response relations of auditory nerve fibers, often constitute promising alternatives. Mathematical modeling and data-analysis tools from nonlinear-systems identification are then required to relate the observed phenomena to details of the biophysical machinery.

Recently, however, important genetic advances have led to the cloning of a mechanosensory transduction channel expressed in the sensory bristle of *Drosophila* (Walker et al., 2000). We may thus hope that, in the future, genetic manipulations lead to new ways for investigating the features of mechanotransduction, thus complementing electrophysiological studies.

Different sensory systems rely on mechanosensitivity, e.g., hearing, balance, touch, and proprioception. The early appearance of mechanosensitivity in evolution suggests that many of these systems are genetically linked (Martinac, 2001; Martinac and Kloda, 2003). The common mechanosensory basis allows us to draw analogies between these different sensory systems, among which are the well-studied examples of the Pacinian corpuscle (Loewenstein, 1971; Horch, 1991) and of muscle stretch receptors (Proske and Gregory, 2002).

CHAPTER SUMMARY:

Acoustic signals are characterized by the time course of air-pressure fluctuations and can vary on many different time scales. Analyzing the responses of auditory nerve cells is therefore naturally connected to questions concerning stimulus integration and the neural representation of time. The generation of electrical signals in auditory receptor cells is triggered by a mechanosensitive transduction process. As in many other sensory processing systems, transduction is part of a sequence of several biophysical processes that are involved in stimulus encoding.

CHAPTER 2

THE GRASSHOPPER EAR

Our model system for investigating the transduction of acoustic signals in this study is the auditory periphery in grasshoppers (Orthoptera, Acrididae). All electrophysiological recordings presented in this study were performed with migratory locusts (*Locusta migratoria* L.), an acridid grasshopper species commonly used in anatomical and electrophysiological investigations. Details of the experimental procedure applied in this study are left to Appendix A.

Several reasons make the grasshopper ear a suitable model system for studying auditory transduction. First, its anatomy is well described (Schwabe, 1906; Gray, 1960; Stephen and Bennet-Clark, 1982). Second, the experimental preparation is simple and robust and allows fairly long, reliable recordings of activity in the auditory nerve and the metathoracic ganglion, to which the receptor neurons send their axons. Third, the coupling of the cells to an ear drum suggests functional similarities with mammalian hearing; yet, the simpler mechanical structure (e.g., lack of cochlear amplification) allows more concise analyses of the basic processes. Fourth, a large background of behavioral studies on acoustic communication for different grasshopper species demonstrate the major importance of hearing for these animals and provides us with knowledge about the characteristics of behaviorally relevant sound stimuli.

This chapter provides a short description of results from behavioral studies with grasshoppers and summarizes anatomical and physiological knowledge about the grasshopper ear. Since the tympanic hearing organ appears to be highly conserved among acridid grasshoppers (see, e.g., Meyer and Elsner, 1996), we will draw on results obtained with different species. To round off the background for the present study, new experimental data are described, complementing earlier studies on temporal resolution and phase locking.

2.1 Behavioral Relevance

Hearing provides important sensory information for many grasshopper species. Similar to many other animals, grasshoppers need to recognize particular sounds and localize the corresponding sources in space, mainly in order to recognize predators and identify mating partners. The latter is most elaborate for gomphocerine grasshoppers (Acrididae,

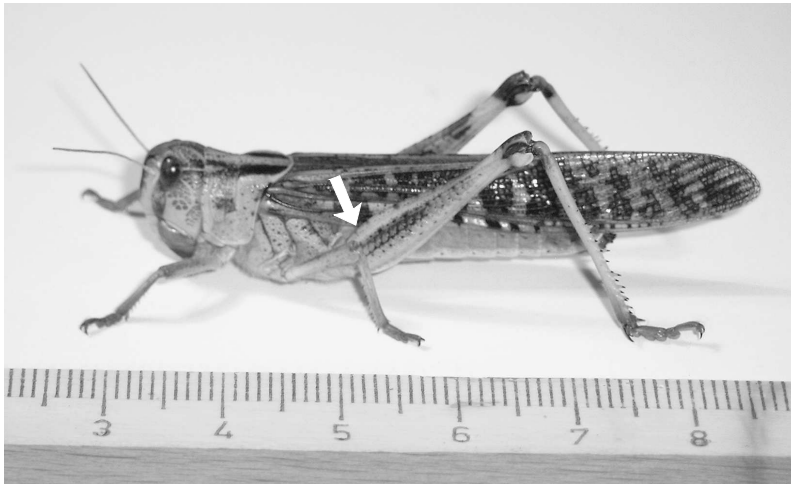


Figure 2.1: Photograph of an acridid grasshopper belonging to the species *Locusta migratoria*. The scale in the foreground is in centimeters. The ear is located in the first abdominal segment just above the coxa of the hindlegs (white arrow).

Gomphocerinae), which use bidirectional acoustic communication (von Helversen and von Helversen, 1994). The species-specific acoustic signals are produced by moving the hindlegs across the forewings (*stridulation*) leading to a rhythmical sound, a “song”. If a female grasshopper has identified a song from a potential male partner, she may respond in a similar fashion – if she has identified the male as belonging to her own species and if she is willing to mate with him (von Helversen, 1972).

Behavioral studies have led to profound knowledge about those parameters in the male’s song that are most relevant for the decision by the females in some grasshopper species. The males’ songs of the gomphocerine grasshopper *Chorthippus biguttulus*, e.g., consist of rhythmical patterns with alternating loud and quiet parts (*syllables* and *pauses*) for a total length of 1–3 s. The syllables are around 100 ms long and the pauses around 10 ms. These two temporal parameters are primarily important for the “attractiveness” of the song, as judged by the response probability of the female, and intriguingly, it is their ratio that appears to be of major importance (von Helversen, 1972). Furthermore, the female’s response in *Ch. biguttulus* is suppressed if the syllables are interspersed with short gaps of about 2 ms or more (von Helversen, 1972). This corresponds to naturally occurring situations when a male grasshopper has lost a hindleg due to predators or complications during molting. We thus know from the outset that the auditory periphery must be able to reliably transmit information over time scales from few to hundreds of milliseconds.

2.2 Anatomy

Anatomical studies on insect tympanic hearing organs have a long tradition; an early cornerstone was set by Schwabe with a seminal anatomical characterization nearly 100 years ago (Schwabe, 1906). A number of studies has since led to a detailed picture of the fine structure in the grasshopper ear (Gray, 1960; Michelsen, 1971b; Stephen and Bennet-Clark, 1982; Breckow and Sippel, 1985; Jacobs and Lakes-Harlan, 1999).

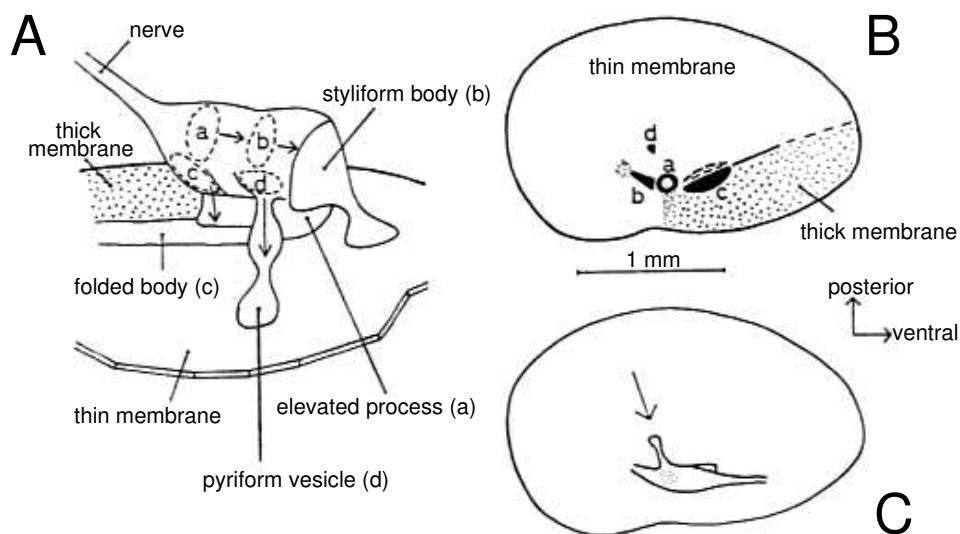


Figure 2.2: Schematic drawings of the tympanum and the auditory ganglion for the locust *Schistocerca gregaria*. (A) The auditory ganglion is located on the interior side of the tympanum. It is connected to the tympanum via four processes (a–d). The auditory nerve projects medially to the metathoracic ganglion. (B) View onto the tympanum. Thin and thick parts of the membrane and the four attachment sites of the auditory ganglion are marked. (C) View onto the tympanum showing the location of the auditory ganglion. The arrow indicates the viewing angle for panel A. Figure adapted from (Michelsen, 1971b) with permission.

The two ears of grasshoppers are located in the first abdominal segment, just above the coxa of the hindlegs, where the leg is attached at each side of the body (Fig. 2.1). The tympanum, the animal's ear drum, is located in a small cavity and vibrates in response to incident sound as has been observed under stroboscopic illumination (Stephen and Bennet-Clark, 1982; Breckow and Sippel, 1985) and with laser interferometric measurements (Michelsen, 1971b; Michelsen, 1979; Schiolten et al., 1981). Sound signals can act on both sides of each tympanum; the space between the tympana is filled with air sacs, allowing the air pressure to pass through the animals body. In contrast to the description of ear drums in mammalian ears as pressure receivers, the grasshopper tympanum thus functions as a pressure-difference receiver (Autrum, 1940; Michelsen, 1994), at least for lower sound frequencies. This “mechanical subtraction” is an essential aspect of sound localization for insects, which due to their size have to cope with extremely small differences of intensity and arrival time between the two ears.

On the inner side of the tympanum lies the auditory ganglion, also called Müller's organ, which contains the somata of about 60 to 80 bipolar receptor cells. As schematically depicted in Fig. 2.2, four attachment processes connect the auditory ganglion with the tympanum, each containing the dendrites from a distinct group of receptor cells. The axons of the cells leave the ganglion via the auditory nerve. They are ensheathed in glia, and Gray (1960) denotes their diameter with 0.3 to 1.5 μm for *Locusta migratoria*. However, more recent stainings by Jacobs and Lakes-Harlan (1999) show many axons with 2 to 3 μm in diameter and even up to 8 μm in single cases. These studies were performed on the closely related locust *Schistocerca gregaria*, and the picture is expected to be very

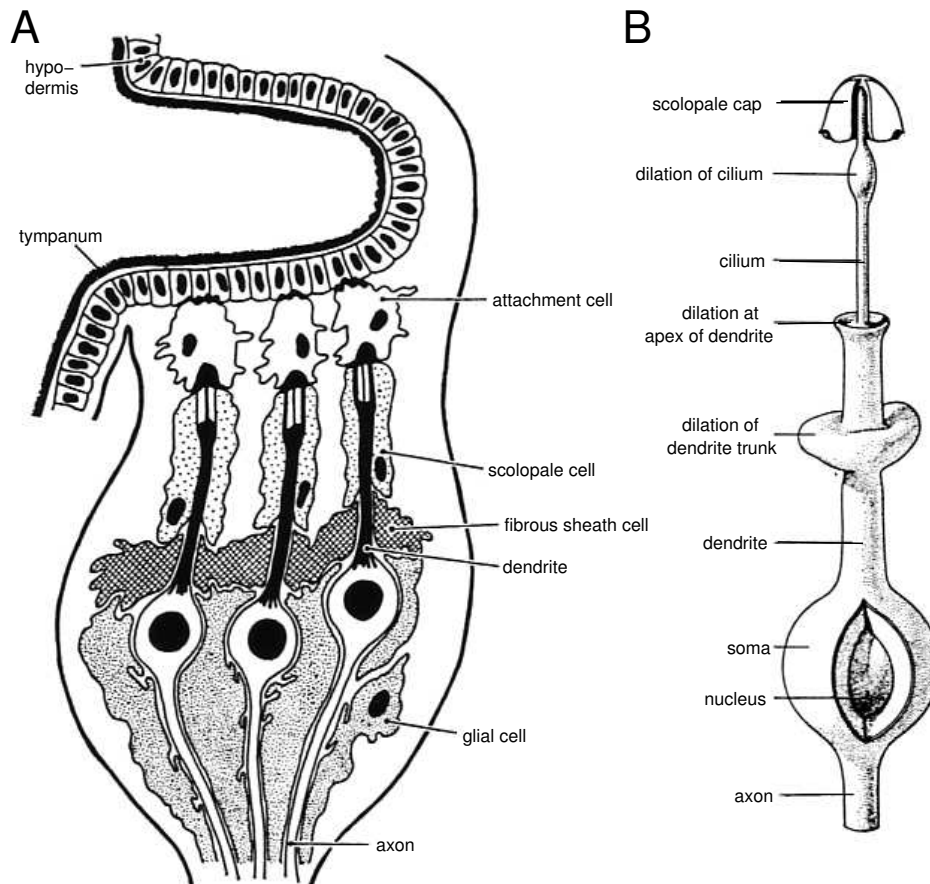


Figure 2.3: Anatomy of locust auditory receptor neurons (*L. migratoria*). (A) Sensilla in the auditory ganglion. Three receptor cells are depicted, surrounded by satellite cells – glial cells (Gray (1960) identifies these with Schwann cells), fibrous sheath cells, and scolopale cells – and connected to a fold (*elevated process*) of the tympanum via attachment cells. (B) Dendritic structure of a receptor neuron. From the dendrite's apex, a cilium protrudes, whose tip is surrounded by a small scolopale cap. Dendrite and cilium show prominent dilations whose function and relevance for transduction are still unclear. Figure adapted from Gray (1960) with permission.

similar to that of *L. migratoria*. The axons project into the metathoracic ganglion where they branch off and connect to different types of secondary auditory neurons (Stumpner and Ronacher, 1991; Stumpner et al., 1991).

The organization of the auditory ganglion in *L. migratoria* is described in detail by Gray (1960). Together with three satellite cells and an attachment cell, each receptor cell forms a sensory unit, a *sensillum* (Fig. 2.3). The cells' dendrites are approximately 100 μm long and enclosed by the satellite cells. A single cilium runs down most of the dendrite's length and protrudes from its apex. The cilium is connected to the hypodermis of the tympanum via the attachment cell. A vibration of the tympanum thus leads to forces on the cilium and the apical dendrite. Whether it is compression, stretch, or twisting that is responsible for the transduction is not known, mostly because the tympanum contains folds and inhomogeneities that lead to complex local movements at the attachment site of the receptor cell (Breckow and Sippel, 1985). Furthermore, it has been shown that the auditory ganglion itself is not static during the mechanical vibration, but moves and

displays resonance properties different from those of the tympanum (Stephen and Bennet-Clark, 1982; Breckow and Sippel, 1985). As hypothesized by Michelsen (1971a;b), it appears to be the relative movement of tympanum and auditory ganglion that leads to receptor-cell activation.

2.3 Electrophysiology

When the tympanum vibrates, mechanosensory ion channels in the receptor cell's membrane open and lead to a depolarization of the membrane potential. The mechanical structures at the ear are delicate and vulnerable, and intracellular recordings of the potentials in the soma or dendrites are difficult; hence data are scarce. Nevertheless, Hill (1983a) noted that in auditory receptor neurons of *L. migratoria* sound-induced depolarizations are composed of small unitary events, which can superimpose to yield a plateau depolarization for prolonged stimulation. He also provided evidence that already in the basal part of the dendrite spikelets of about 20 mV are formed, which trigger "full-blown" action potentials in the axon. From the cut-off frequency in the spectrum of the recorded voltage fluctuations, he deduced an order-of-magnitude approximation of 10 ms for the time constant of the receptor neurons, but the difficulties in obtaining reliable recordings and the noisy data leave ample room for alternative interpretations. Other studies, based on the analysis of spike timing in response to sinusoidally modulated stimuli, have led to estimates near 1 ms of the time over which the receptor cells integrate the stimulus (Prinz and Ronacher, 2002). To complement these studies, we will in Section 2.4 present a new investigation of integration times in locust auditory receptor neurons based on the commonly used technique of spike-triggered averages (Rieke et al., 1997).

In response to sounds of sufficient intensity, the receptor neurons produce series of action potentials. These can be reliably recorded from the axons in the auditory nerve, which is accessible without destruction of the ear's mechanical components. Figure 2.4 shows an example of a spike train recorded from one receptor-cell axon in *L. migratoria*. The neuron fires continuously during stimulation. At the onset of a stimulus, firing rates can reach values as high as 300 to 400 Hz (at room temperature) or 500 to 600 Hz (at 30 °C). Spike-frequency adaptation decreases the firing rate during the first few hundred milliseconds. Eventually, the activity settles in a steady state of tonic spiking with a maximal rate around 200 Hz (at room temperature) or 300 Hz (at 30 °C).

The dependence of the firing rate on stimulus intensity is captured in the *rate-intensity function*. In Fig. 2.5A, an exemplary measurement of a rate-intensity function shows how the receptor cell's activity increases with stimulus intensity in a sigmoidal fashion. Below a threshold intensity, there are virtually no spikes. Only in few cases, a small amount of spontaneous activity is observed. For high intensities, the firing rate saturates at a maximum value. The dynamic regime between threshold and saturation usually spans about 15–30 dB (Römer, 1976).

The exact shape of the rate-intensity function (its threshold, saturation level, and steepness) varies considerably between individual neurons (Römer, 1985). Measuring rate-intensity functions for many different sound frequencies from a single cell, though, reveals another general property of the receptor neurons; to good approximation, the rate-intensity functions are shifted versions of one another along the intensity axis, where

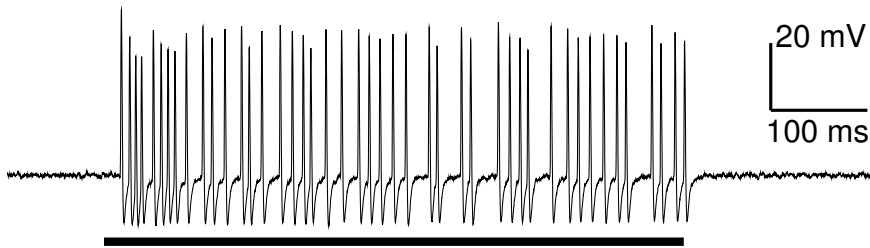


Figure 2.4: Voltage trace recorded from a receptor-cell axon in the auditory nerve of a locust. The stimulus was a 4-kHz pure tone of constant intensity played for 600 ms, as indicated by the black bar below the voltage trace. The stereotyped spikes are clearly visible and can easily be detected automatically by suitable computer programs. Before and after stimulation, no activity is seen.

intensity is measured in the logarithmic units of sound-pressure level, dB SPL.¹ This phenomenon has been reported before for *L. migratoria* by Suga (1960) and Römer (1976). A detailed example from our own measurements with frequencies spanning the whole sensitivity range of a single receptor cell can be seen in Fig. 2.5B. The generic shape of the rate-intensity functions becomes even clearer when they are shifted relative to each other so that they meet at 250 Hz firing rate (Fig. 2.5C).

The frequency-resolved sensitivity of a single receptor cell is commonly characterized by a threshold curve, i.e., the dependence of the threshold on the sound frequency. Fig. 2.5D shows the threshold curve together with curves denoting the intensities that lead to firing rates of 150 and 300 Hz. The curves are all approximately parallel to each other, which is a consequence of the generic shape of the rate-intensity functions. Instead of measuring threshold curves, the tuning characteristics of the neuron can thus also be assessed by recording such curves that lead to some fixed firing rate. This approach was followed within this thesis, usually for a fixed rate of 150 Hz; threshold curves are sometimes difficult to obtain accurately under limited recording time, as the rate-intensity functions often flatten out near the threshold and are corrupted even by small background activity (Michelsen, 1971c).

The absolute sensitivities vary between individual neurons (Römer, 1985); but generally, the receptor cells respond to sound frequencies in the range of 1 to 30 kHz and can be characterized by their frequency-tuning characteristics into two groups. *Low-frequency receptor cells* have a *characteristic frequency* (sound frequency of highest sensitivity) of around 5 kHz; *high-frequency receptor cells* of around 15 kHz. Using details about the location of the sensitivity maximum and the absolute sensitivity, the receptor neurons of *Locusta migratoria* and *Schistocerca gregaria* were grouped into three (Jacobs et al., 1999) or four classes (Michelsen, 1971a; Römer, 1976), which also holds for gomphocerine grasshoppers (Stumpner and Ronacher, 1991). This physiological classification can

¹Sound-intensity differences are commonly measured in the logarithmic dB scale; the difference in dB for two sound pressures A_1 and A_2 is $\text{dB} = 20 \log_{10} A_1/A_2$. For stationary signals, A_1 and A_2 are taken as the root-mean-square values over the time course of the sound-pressure fluctuations. For short stimuli, we will often state the dB values corresponding to the peak pressure. All absolute values of intensity in this work are denoted in dB sound-pressure level (dB SPL), which is measured relative to a sound pressure of 20 μPa , the average human hearing threshold at 1 kHz.

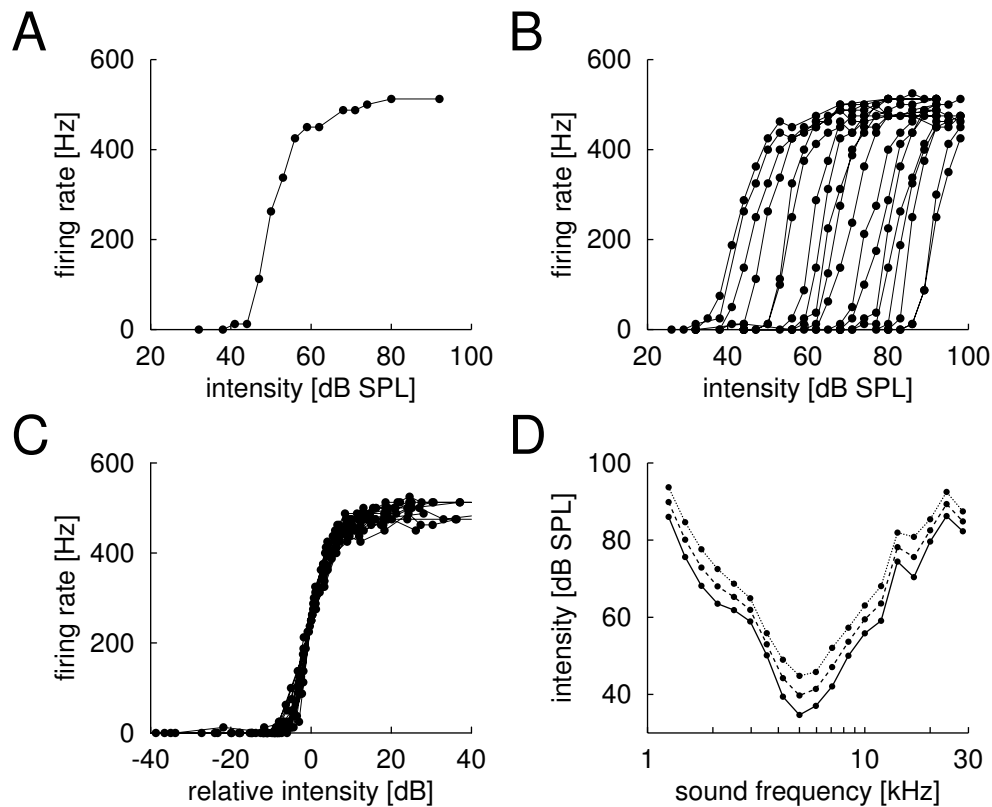


Figure 2.5: Firing-rate responses of a locust auditory receptor cell. (A) Rate-intensity function for a 7-kHz pure tone. The observed sigmoidal shape of the rate-intensity function is typical for many sensory neurons. (B) Rate-intensity functions of the same neuron for many different pure tones between 1.25 and 28 kHz. Connected points belong to the same sound frequency. Curves further to the left correspond to frequencies where the cell is more sensitive. Although there are large differences concerning the intensity range where the individual rate-intensity functions rise from threshold to saturation, their overall shape is very similar. For example, all measured rate-intensity functions have approximately the same slope in the rising part of the curves and saturate at around the same level. (C) The same rate-intensity functions as in B, now shifted along the dB-axis such that they align at a firing rate of 250 Hz. This demonstrates the generic shape of the rate-intensity functions. (D) Curves denoting equal firing rates at different sound intensities for the same cell. The threshold curve (solid line) and the intensities corresponding to constant firing rates of 150 Hz (dashed line) and 300 Hz (dotted line) are shown for pure tones between 1.25 and 28 kHz. The three curves are approximately parallel to each other reflecting the similarity of the rate-intensity functions for different frequencies. Figure adapted from (Gollisch et al., 2002) with permission.

be identified with the morphological classification according to the four attachment sites of the auditory ganglion to the tympanum with two morphological classes showing nearly identical physiology (Jacobs et al., 1999). The receptor neurons thus obtain their tuning properties largely from the local resonance characteristics of the tympanum (Michelsen, 1971b; Schiolten et al., 1981). Information about sound frequency is therefore contained in a *place code* reminiscent of the one that is discussed for vertebrate ears (Zwislocki, 1991).

In auditory nerve fibers of vertebrates, spike timing is often found to lock to the phase of the carrier frequency in the sub-kilohertz range and even up to a few kilohertz (Geisler, 1998). In grasshopper receptor cells, which are only sensitive in the kilohertz range,

phase locking has not been observed. Suga (1960) mentioned the absence of phase locking anecdotally, and Hill (1983) reported that the power spectrum of the intracellularly recorded membrane potential shows no peak at the carrier sound frequency. Data on this are scarce, though, and Section 2.4 will therefore present a new systematic investigation of phase locking in auditory receptor neurons of locusts.

The amplitude of a sound's carrier frequency, also called the *stimulus envelope*, may be modulated in time. In contrast to the absence of phase locking, this temporal structure leaves its imprints on the pattern of spiking activity. For modulations up to several hundred hertz, the receptor cells reliably track the time course of the stimulus envelope. Linear reconstruction techniques allow to retrieve this aspect of the acoustic signal with high signal-to-noise ratio from the recorded spike trains of single locust receptor cells (Machens et al., 2001), and information rates for strongly modulated signals can reach up to 380 bits/s (Watzl et al., 2003). These high information rates partially rely on the cell's ability to accurately lock to fast and strong rises in intensity with an accuracy down to a few hundred microseconds. It has been shown that, based on a spike-train metric, the responses of single receptor neurons can be used to discriminate between different instances of mating songs of *Ch. biguttulus* (Machens et al., 2003). Furthermore, the trial-to-trial variability of spike trains under repeated stimulation with the same acoustic signal can be captured by a generic model based on an inhomogeneous Poisson process equipped with a recovery function that incorporates the neuron's refractoriness (Schaeffe et al., 2004). In order to connect these studies concerning the sound-encoding properties of the receptor neurons to the biophysical properties of the cells, one needs to study how the constituents of the auditory transduction chain influence the generation of spikes.

2.4 Complementary Experiments

In order to gain a better understanding of the temporal resolution of locust auditory receptor neurons, we analyzed their integration times by a standard spike-triggered-average analysis. To do so, we presented a rapidly varying acoustic signal, a 5-kHz tone whose envelope is a low-pass-filtered Gaussian white noise with a cut-off frequency of 2.5 kHz. Figure 2.6 shows an example of spike trains recorded from a single receptor neuron in response to such a stimulus. The experiment was performed while keeping the animal at a temperature of around 30°C. Sharp intensity peaks lead to reliable and precise spike timing. The spike-triggered average, Fig. 2.6D, which is calculated by averaging all stimulus sections preceding a spike (Rieke et al., 1997), shows that the spikes of this neuron in general followed high-intensity excursions that occurred around 4 to 5 ms before the spike. This tells us that the stimulus part responsible for triggering a response was generally contained in this temporal window before the spike. The integration time in this case was thus at most around 1 ms. We tested this for a few more receptor cells and generally found similar peaks of approximately 1 ms, sometimes up to 2 ms width.

However, these values can only be viewed as upper bounds for the integration time, i.e., the time span over which input is combined to contribute to the response. The true temporal window of stimulus integration could be even smaller. The spike jitter, which for the receptor neurons is also around one millisecond, smoothes out any structure of the spike-triggered average below this time scale. The jitter thus limits the resolution

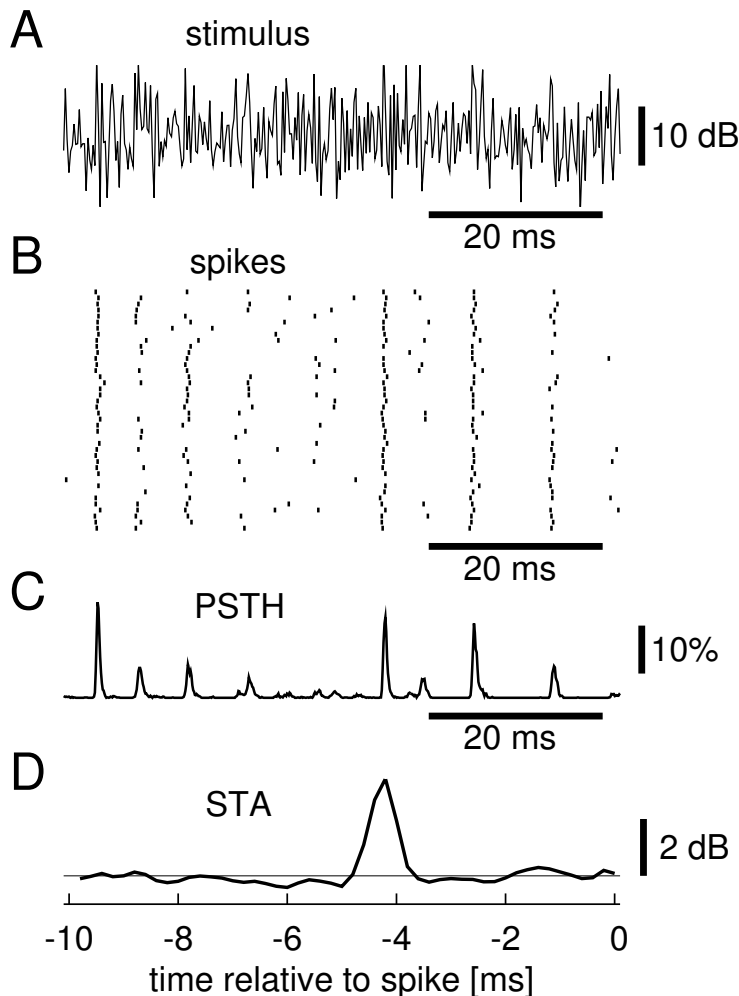


Figure 2.6: Response examples of a locust auditory receptor cell to noise-modulated sound. (A) The stimulus consisted of a 5-kHz tone whose envelope was high-pass-filtered Gaussian white noise with a cut-off frequency of 2.5 kHz. The mean and standard deviation of the stimulus envelope were 58 dB SPL and 5 dB, respectively. The stimulus duration was two seconds; shown is a 60-ms excerpt of the stimulus envelope. (B) Raster plot of spike times corresponding to the stimulus section shown above for 40 exemplary stimulus presentations. (C) Peri-stimulus time histogram (PSTH) for the same stimulus section showing the spike-occurrence probability for 0.1-ms bins calculated from a total of 555 stimulus presentations. (D) Spike-triggered average (STA) obtained by averaging all 10-ms stimulus parts that preceded a spike for the complete two-second stimulus of all presentations. The mean value of the stimulus envelope was subtracted.

of this correlation method to around 1 ms. Furthermore, the limited resolution does not allow us to draw conclusions about the shape of the temporal integration window, i.e., how different stimulus parts are weighted relative to each other. The symmetrical and nearly Gaussian shape of the peak in the spike-triggered average is typical of a structure that is smoothed out by noise. We will return to the question of temporal integration in Chapter 6 and analyze it in more detail with a new experimental technique.

We now come back to the question whether spike trains in receptor neurons phase lock to the stimulus carrier frequency. To test this hypothesis systematically, we gathered the timing of many spikes to a pure tone played at constant intensity. In vertebrate auditory-nerve fibers, phase locking of spikes is usually found only for sound frequencies below a few kilohertz and more pronounced at higher sound intensities (Geisler, 1998). Furthermore, the action-potential duration of about 1 ms in the grasshopper auditory nerve makes it nearly impossible to obtain high enough precision to test for phase locking at frequencies higher than 2 kHz. For these reasons, we chose to stimulate the neurons with a sound frequency of 1 kHz, which approximately marks the lower limit of the frequency sensitivity range.

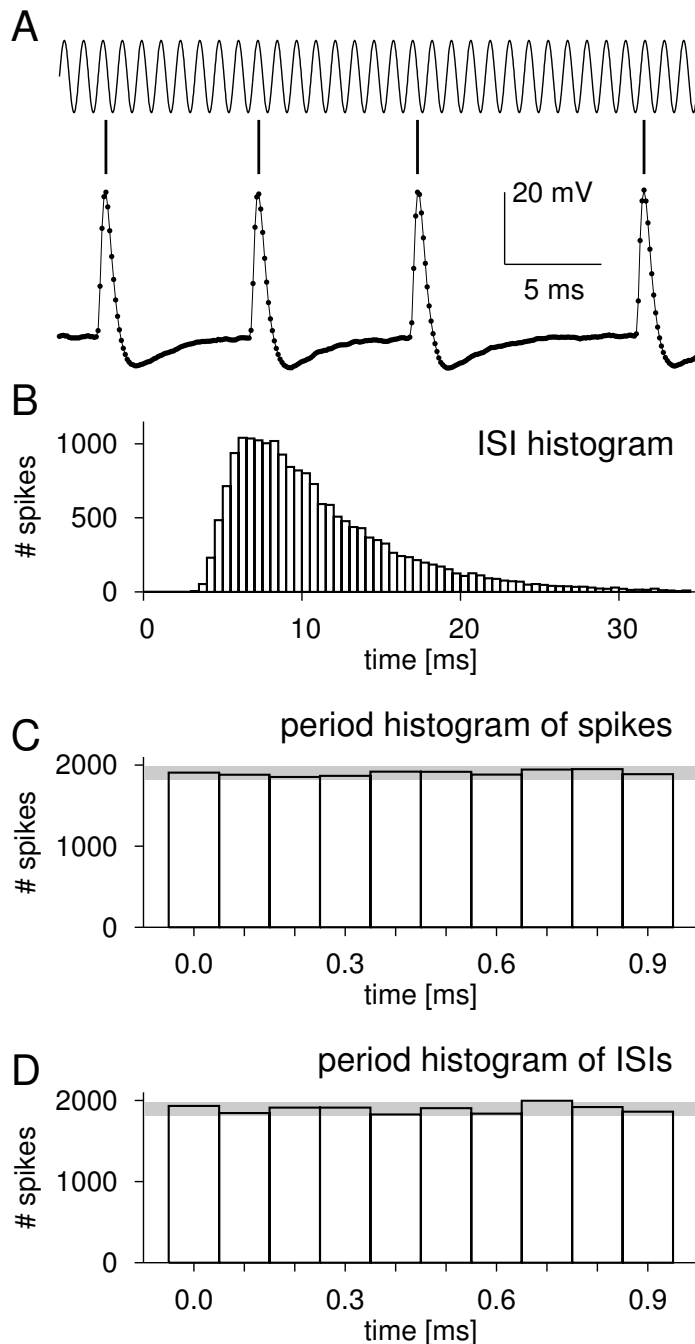


Figure 2.7: Experimental test of phase locking in a locust auditory receptor cell. **(A)** The acoustic stimulus was a 1-kHz tone, played for 4 s at a constant intensity of 100 dB SPL and repeated 60 times. The first 0.5 s of the responses were discarded to minimize adaptation effects; the resulting average firing rate was 90.5 Hz. A 30-ms excerpt of the stimulus is shown (top) as well as the corresponding voltage trace recorded from the axon (bottom). The data-acquisition rate was 10 kHz, and the dots on the current trace show the individual sample points. The spike times were determined as the local maxima of voltage episodes that reached a threshold of 10 mV above the baseline. The acquired times of four spikes are indicated by the bars above the voltage trace. **(B)** Histogram depicting the number of measured inter-spoke intervals (ISIs) in bins of 0.5 ms. **(C)** Period histogram of spike times relative to the stimulus. The spikes were grouped in 10 bins of equal width (0.1 ms) according to the phase at which they occurred in the stimulus cycle. The total number of spikes was 19,006. **(D)** Period histogram of phase differences between successive spikes. The inter-spoke intervals were grouped in 10 bins of 0.1 ms according to the phase difference between the two spikes. The zero bin thus captures all inter-spoke intervals that are an integer multiple (up to 0.1 ms) of the 1-ms stimulus cycle. The total number of inter-spoke intervals was 18,946. The gray bars in **C** and **D** denote the area where deviations from a binomial distribution are not significant at the 5% level.

For the analysis, we measured spike times with a resolution of 0.1 ms and determined their relation to the stimulus phase (Fig. 2.7A). The distribution of inter-spoke intervals displays a large spread (Fig. 2.7B). Locking to the stimulus carrier frequency can be investigated with period histograms, where spikes are counted according to the phase at which

they occurred within the one-millisecond stimulus period. This is shown in Fig. 2.7C. The spikes are nearly equally distributed over all bins and thus show no preference for a particular stimulus phase. The small deviations from the mean count can be tested for significance by comparing the data to a binomial distribution with probability 0.1 for each bin. The gray area denotes the region of $m \pm 2\sigma$, where m and σ are mean and standard deviation of the binomial distribution, respectively. This corresponds very closely to the 5% significance level of deviations from the binomial distribution for a single bin. The analysis shows that the observed small differences of the counts per bin can be attributed to random fluctuations.

Figure 2.7D displays a different analysis; here the inter-spike intervals are grouped according to the phase difference between the timing of two successive spikes. Spike pairs that occur at the same stimulus phase thus contribute to the “zero” bin in the histogram. This way of investigating stimulus locking has the advantage that it is independent of slow drifts in the absolute relation between stimulus phase and spike time, which might occur if the latency of spike occurrence changes over the course of the experiment. However, this plot also shows no preference for spikes to occur at the same stimulus phase. The gray bar again denotes the 5% significance level of the deviations from the mean count.

The same general result was found for two other receptor neurons investigated under this paradigm. The picture also did not change if only a subset of the trials was included in the analysis. This was tested to minimize the possibility that phase locking is simply covered by slow changes of the neural properties during the long course of the experiment. In conclusion, we therefore find that spike timing contains no information about the phase of the carrier frequency, which is in agreement with the earlier observations presented in the previous section.

2.5 Comparison with the Mammalian Ear

Sound transduction in mammalian and insect ears conceptually involve the same sequence of processes, the coupling of the sound-pressure wave to a mechanical resonator, the gating of mechanosensitive transduction channels, the accumulation of charge in the receptor cells, and the encoding into spike trains in the auditory-nerve fibers. There exist, however, essential differences in the biophysical constitution of these basic steps.

In mammalian hearing systems, auditory receptor cells are hair cells in the organ of Corti between the basilar and the tectorial membrane of the cochlea. The cochlea itself has complex mechanical properties. Together with the ability of outer hair cells to actively produce movements (Martin and Hudspeth, 1999), this leads to nonlinear signal amplification (Eguíluz et al., 2000). This mechanism appears to be absent in insect receptor cells, although measurements of otoacoustic emissions are a sign of small nonlinear mechanical effects in locust ears (Kössl and Boyan, 1998a; Kössl and Boyan, 1998b). In hair cells, transduction currents are triggered by the relative deflections within an ordered bundle of cilia (Gillespie and Walker, 2001), whereas insect auditory receptor cells generally only have a single cilium. Furthermore, the signal transduction in the mammalian ear involves a chemical synapse between hair cells and the auditory-nerve fibers, whereas the auditory receptor cells of grasshoppers possess axons themselves, which can be found in the auditory nerve.

Despite the fact that the complete processing chain in the mammalian ear is apparently more complex, several studies suggest that mammalian and insect hearing are based on similar transduction mechanisms. Both systems, e.g., have in common that the transduction sites are exposed to an unusually potassium-rich extracellular solution (French, 1992; Thurm, 1996; Geisler, 1998), which suggests that the auditory transduction currents are generally mediated by potassium ions. Similarities in the biophysical machinery of transduction are also suggested by the discovery of related developmental pathways. The *Drosophila* gene *atonal* and its mouse homolog *Math1* are required for the development of chordotonal auditory organs in the fly and mammalian hair cells, respectively (Bermingham et al., 1999; Eberl, 1999). Furthermore, the same genetic developmental program forms the basis for the generation of sensory patches in the chick inner ear and of sensory bristles in *Drosophila* (Adam et al., 1998). It is thus natural to aim at generalizing the results obtained from specific hearing systems. In view of the above mentioned differences, however, the validity of the generalization and the limitations of their applicability to particular systems should be tested by comparative studies. For example, as mentioned earlier, auditory-nerve fibers in mammals often display phase locking of spikes to the carrier frequency, whereas in grasshoppers they do not. For high-frequency signals above a few kilohertz, though, mammalian auditory nerve-nerve fibers also do not phase lock, and a comparison of methods and results may therefore focus on this stimulus regime.

CHAPTER SUMMARY:

The model system in this study of the transduction of acoustic signals is the auditory periphery of grasshoppers. This system combines detailed knowledge about the behavioral relevance of specific sound signals, well characterized anatomy, and accessibility for electrophysiological recordings. A spike-triggered-average analysis showed that the integration times of auditory receptor cells are presumably smaller than 1 ms, and the spike times show no trace of phase locking to the stimulus carrier frequency. The common evolutionary and developmental background of different mechanosensory and auditory systems suggests that insight gained in a particular system may contribute to a general understanding of auditory transduction.

CHAPTER 3

NONLINEAR SYSTEMS ANALYSIS

Auditory receptor neurons encode the incoming sound into a series of action potentials. From a signal-processing perspective, this encoding corresponds to a nonlinear operation performed on the acoustic input. The individual components of this operation define the functional modules of the auditory transduction chain. In order to identify and characterize the modules from experimental data, we require a suitable conceptual framework. In this chapter, we will therefore shortly review selected aspects of nonlinear systems analysis (Marmarelis and Marmarelis, 1978), which provides a set of modeling approaches and corresponding analysis tools to tackle similar systems identification tasks.

3.1 Survey of Principle Approaches

A primary focus of nonlinear systems analysis is to find a model of the system's input-output relation. For establishing this relation, one relies on sample sets of input and output, and if this is indeed the only available information about the system, the analysis has a *black-box* characteristic. In some cases, on the other hand, prior knowledge about the system's basic structure, e.g., its biophysical composition, may guide the setup of a model framework, in which case one may speak of a *gray-box* approach. Depending on how such prior knowledge is included, the models can conceptually be classified. Following Billings (1980) as well as Korenberg and Hunter (1986), we discuss three principal approaches to the identification of nonlinear systems.

1) The *functional series approach*, also called *nonparametric kernel approach*, is a true black-box technique. The input-output relation is approximated by a functional expansion with terms of increasingly higher order. The most basic form of this expansion is the *Volterra series*, which relates the system's input $s(t)$ to its output $r(t)$ by a baseline output r_0 and input-dependent convolution integrals containing nonlinear kernels $h_n(\tau_1, \dots, \tau_n)$:

$$r(t) = r_0 + \sum_{n=1}^N \int_{-\infty}^{\infty} \dots \int_{-\infty}^{\infty} h_n(\tau_1, \dots, \tau_n) \prod_{i=1}^n s(t - \tau_i) d\tau_i. \quad (3.1)$$

Here, N defines the order of the approximation. In application, one often finds a variant of this expansion, the *Wiener series*, which differs slightly in the composition of the

expansion terms. Well-established experimental techniques estimate the expansion terms successively from increasingly higher-order correlations between the output and random input signals. The advantage of this approach lies in its independence of assumptions about the mechanisms, but it works well only for low-order nonlinearities and often requires huge amounts of data measured under stationary conditions.

2) In the *parametric approach*, the functional dependence of the system's output on the history of inputs and previous outputs (and possibly noise terms) is captured in a suitable parametrization. For example, in the *NARMAX* approach (Nonlinear AutoRegressive Moving Average model with eXogenous inputs), the relation between time series of inputs s_k , outputs r_k , and unobservable noise e_k is given by the general form

$$r_k = F\left(r_{k-1}, \dots, r_{k-m}, s_k, \dots, s_{k-n}, e_{k-1}, \dots, e_{k-l}\right) + e_k, \quad (3.2)$$

where m , n , and l stand for the maximum lags of the corresponding time series (Aguirre and Billings, 1995; Billings and Chen, 1998). The nonlinearity $F(\cdot)$ is typically chosen to take a polynomial or rational form, or a particular $F(\cdot)$ may be suggested by prior knowledge about the system's structure. General techniques exist that estimate the parameters based on *prediction error algorithms* for random inputs. The dependence on an explicit parametrization is the advantage as well as the disadvantage of this approach. While allowing to model special types of nonlinearities that may be particularly suited for a given system, the search for a suitable functional form generally relies on intuition, trial-and-error, and luck. Furthermore, for nonlinearities with many parameters and long lags of the system, the computational load of the method quickly increases, thus limiting the applicability.

3) The *block-oriented* or *cascade-model approach* explicitly assumes that the input-output function is composed of standard building blocks that operate in sequence. The individual constituents of the sequence perform simple standard operations, which are often restricted to temporal linear filters and static nonlinear transformations. Combining such functional modules leads to a multitude of different model classes with increasing complexity. For sequences containing only one nonlinearity, generic methods exist to identify the individual components directly from input-output correlations in response to random stimuli (Korenberg and Hunter, 1986; Hunter and Korenberg, 1986). As a gray-box approach, the applicability of cascade models relies heavily on prior knowledge about the structure of the processing chain, e.g., from anatomical studies in biology. On the other hand, this direct connection of the functional modules to the biophysical substrate allows straight-forward interpretation of the measured model characteristics unmatched by the previous two, more abstract approaches. For this reason, cascade models seem particularly suited for modeling transduction chains where the correspondence of the functional modules with the individual steps of the biophysical sequence may often be directly established. Let us therefore take a closer look at the details of this approach.

3.2 Nonlinear Cascade Models

The typical building blocks of cascade models are *temporal linear filters* and *static nonlinear transformations*. Consider a stimulus given by a one-dimensional time-dependent

variable $s(t)$, e.g., the sound-pressure of an acoustic signal. The response $r(t)$ may generally also be time dependent. The effect of a linear filter is then given by the convolution integral

$$r(t) = \int_{-\infty}^{\infty} d\tau k(\tau) \cdot s(t - \tau), \quad (3.3)$$

where $k(\tau)$ is the kernel that characterizes the filter. An important aspect of this filter operation is that it mixes stimulus contributions from different time points to determine the output $r(t)$. Such a filter is sometimes also referred to as *dynamic linear filter*. In order to guarantee that the response is only influenced by previous stimulus parts, not by future ones, the kernel must satisfy a causality condition, i.e., $k(\tau) = 0$ for $\tau < 0$. The lower limit of the integral in Eq. (3.3) can then be set to 0. For future use, let us add that an analogous formula describes the linear filter if the input signal is not given as a time-dependent function, but as a discrete set of values s_n . The response r_m , which may denote the response at a certain time point t_m , then simply follows from the convolution

$$r_m = \sum_{n=1}^N k_n \cdot s_{m-n}, \quad (3.4)$$

where the k_n , $n = 1 \dots N$, denote the components of a filter with length N . If we are only interested in a single response component $r = r_0$, we can simplify the notation by setting $m = 0$ and substituting s_n for s_{-n} . We thus formally obtain a scalar product of two vectors $\vec{s} = (s_1, \dots, s_N)$ and $\vec{k} = (k_1, \dots, k_N)$,

$$r = \vec{k} \cdot \vec{s} = \sum_{n=1}^N k_n \cdot s_n. \quad (3.5)$$

A static nonlinear transformation, on the other hand, is defined by

$$r(t) = g(s(t)), \quad (3.6)$$

where $g(\cdot)$ stands for some one-dimensional nonlinear function. Since the response $r(t)$ depends only on the stimulus $s(t)$ at a single point in time, the transformation is called an *instantaneous* or *static transformation*.

By putting these model building blocks in sequence, an arbitrarily large variety of different models can be created. A special case, e.g., is the Wiener system (not to be confused with the Wiener series of the previous section), which consists of a temporal linear filter followed by a static nonlinearity, also known as *LN cascade* (Hunter and Korenberg, 1986). The general form of a Wiener system is thus

$$r(t) = g\left(\int_{-\infty}^{\infty} d\tau k(\tau) \cdot s(t - \tau)\right). \quad (3.7)$$

Another example, which has found similar interest in the literature, is the Hammerstein system (Hunter and Korenberg, 1986), an *NL cascade* of the form

$$r(t) = \int_{-\infty}^{\infty} d\tau k(\tau) \cdot g(s(t - \tau)). \quad (3.8)$$

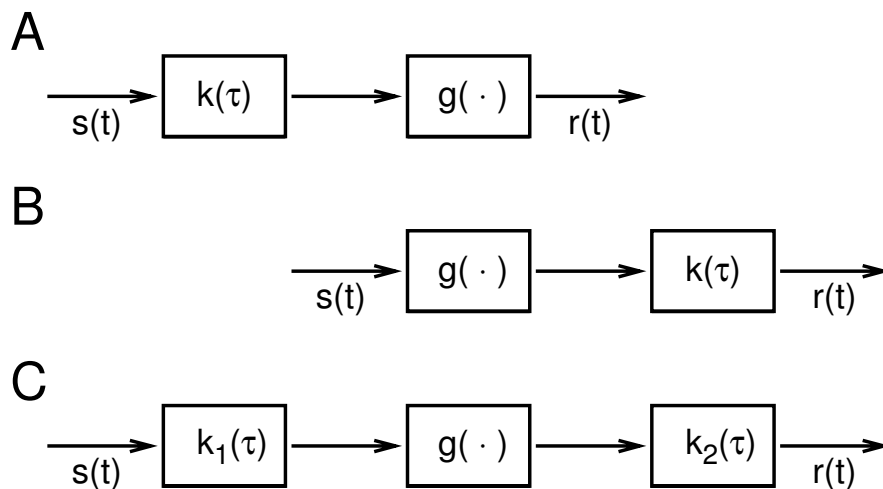


Figure 3.1: Diagrams of cascade models. **(A)** Wiener system. The convolution with the linear filter $k(\tau)$ is followed by a nonlinear transformation $g(\cdot)$. **(B)** Hammerstein system. The nonlinear transformation $g(\cdot)$ is followed by a convolution with the linear filter $k(\tau)$. **(C)** General LNL cascade. The single nonlinear transformation $g(\cdot)$ is sandwiched between two convolution integrals with linear filters $k_1(\tau)$ and $k_2(\tau)$.

Most systematic approaches for matching data to cascade models deal with systems that contain (at most) one nonlinear transformation. The general form of such a cascade is a generalization of Wiener and Hammerstein systems, an *LNL cascade*, which contains two linear filters $k_1(\tau_1)$ and $k_2(\tau_2)$ and a static nonlinearity $g(\cdot)$:

$$r(t) = \int_{-\infty}^{\infty} d\tau_2 k_2(\tau_2) \cdot g \left[\int_{-\infty}^{\infty} d\tau_1 k_1(\tau_1) \cdot s(t - \tau_1 - \tau_2) \right]. \quad (3.9)$$

These three model structures are schematically depicted in Fig. 3.1. One of the first attempts to identify a physiological system that could be approximated by an LNL cascade was the investigation of the primary visual pathway, comprising receptor cells, bipolar cells, and ganglion cells (Spekreijse, 1969; Spekreijse and Oosting, 1970; Marmarelis and Naka, 1972). Korenberg (1973b) later developed general methods to extract the individual components of LNL cascades from cross correlations in white-noise experiments and also developed theoretical techniques to determine the linear filters of higher-order cascades from the kernels of a Volterra expansion (Korenberg, 1973a). As discussed earlier, however, the determination of the Volterra kernels requires large amounts of experimental data, and the experimental application of this approach for higher-order cascades is usually not feasible.

In neuroscience, Wiener systems have found wide applications for modeling single-cell properties. The linear integration is reminiscent of the summation of synaptic currents in a neuron, and the nonlinear transformation may capture the properties of spike generation transforming the currents into firing rates or spike probabilities (Chichilnisky, 2001). The discussion of Wiener systems brings us back to the question of stimulus integration in Section 1.4. Here, the stimulus space is defined by the set of stimulus values at all previous points in time. Stimulus integration manifests itself in the convolution integral of Eq. (3.3) or the summation of Eq. (3.4), respectively. The equations can be viewed as

projections of the high dimensional stimulus s onto the kernel k ; all stimulus components in directions orthogonal to k are suppressed. The kernel k thus marks the single *relevant direction in stimulus space*. The non-zero components of the kernel can be interpreted as the neuron's *receptive field*.

Several studies explicitly deal with the development of techniques that match Wiener systems to electrophysiological data from single neurons. A prevalent technique is the measurement of spike-triggered averages in response to Gaussian white-noise signals (Rieke et al., 1997; Chichilnisky, 2001). In a slightly more elaborate analysis, the measurement of spike-triggered covariance yields multiple linear filters corresponding to different relevant dimensions of stimulus space (Schwartz et al., 2002; Touryan et al., 2002; Bialek and de Ruyter van Steveninck, 1998). A newly developed information-theoretic technique (Sharpee et al., 2004), which allows the extraction of relevant stimulus directions from experiments with non-Gaussian signals, e.g., natural stimuli, is also based on a Wiener-system model. An interesting extension to the studies based on Wiener and Hammerstein models was introduced by an investigation of fly photoreceptor cells (French et al., 1993); from the system's Volterra kernels, which were experimentally determined by a correlation analysis, it was deduced that an NLN cascade captures the cells' input-output relation.

Let us note that the temporal resolution of all these approaches based on correlation analyses is generally limited by the jitter of the output signal, i.e., the spike jitter. The reason is that in order to deduce the contribution of a specific stimulus feature to producing the response, a fixed temporal relation is required between the feature and the response. Spike jitter washes out this relation. This fact obstructs the straight-forward application of these standard techniques to fast processing sequences such as auditory transduction, where the relevant processing time scales are of the same order of magnitude as the temporal jitter of the output or even shorter.

CHAPTER SUMMARY:

A primary goal in nonlinear systems theory is to accurately capture a system's input-output relation by a functional model description. Depending on how prior knowledge about the system's structure is included in the applied model framework, different principal approaches to estimate this relation can be distinguished. For systems known to involve sequential processing chains, cascade models form a suitable framework to analyze the system in a "gray-box" approach. General methods to identify cascade models focus on model structures with at most one nonlinear transformation. The techniques are commonly based on correlation analyses, whose temporal resolution is limited by the jitter of the output.

CHAPTER 4

THE ISO-RESPONSE METHOD

As seen in the previous chapter, cascade models form a suitable model framework for investigating processing sequences such as the auditory transduction chain. However, many of the analysis tools for cascade models provided by nonlinear systems theory are limited to cascades with only one nonlinear transformation and are plagued by limited temporal resolution if the system's output is jittered by noise.

Both these aspects are severe limitations for applying these methods to the auditory transduction chain. For this system, we can easily make out two potentially nonlinear transformations, the gating of the transduction channels by the mechanical vibration as well as the process of spike generation. Furthermore, the involved biophysical processes are fast and act on similar time scales as the output jitter as seen by the simple spike-triggered-average analysis in Section 2.4. To overcome these limitations, a new methodological framework is presented in this chapter. It is aimed at analyzing cascade models that may contain two nonlinear transformations, and it is not based on analyzing temporal correlations of input and output and may thus reach a considerably higher resolution. Particular aspects of this methodology have also been emphasized in (Gollisch and Herz, 2003a;b).

4.1 *IRS – Iso-Response Sets*

The key ingredient of the approach presented in this chapter is to experimentally identify sets of different stimuli that cause the same response. These *iso-response sets (IRS)* are subsets of the stimulus space and characterize the invariances of the system. As we have already seen in the discussion of stimulus integration (Section 1.4), the high dimensionality of the input space lets us expect that such invariances exist and that we will generally be able to find many stimuli leading to the same response.

The measurement of iso-response sets in itself is not new; such concepts are commonly used in electrophysiological investigations by measuring threshold curves (Evans, 1975), i.e., sets of stimuli that yield a minimal response, and in psychophysics by applying equivalence criteria (Jameson and Hurvich, 1972), i.e., determining stimuli that share some perceptual component such as brightness or loudness. We here extend these methods by explicitly combining them with the cascade-model framework.

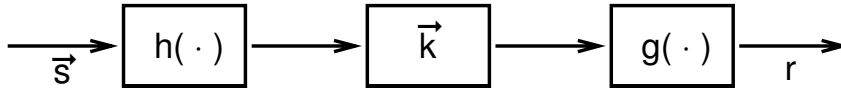


Figure 4.1: NLN cascade. The multi-dimensional signal \vec{s} is transformed by the nonlinearity $h(\cdot)$, subsequently integrated by scalar multiplication with the filter \vec{k} , and finally transformed by $g(\cdot)$ into the one-dimensional response r .

Let us investigate a simple example system to see how iso-response sets can be used in analyzing cascade models. Consider a stimulus with N components s_1, s_2, \dots, s_N . The components could represent a time series, sampled from a stimulus $s(t)$, $s_n = s(t_n)$; alternatively the components could represent the spatial distribution of a stimulus (such as the intensity of light on a screen) or different stimulus features (such as the molecular concentrations in a composite odor). In fact, any division of the stimulus into individual components suffices to define such a stimulus space. For notational simplicity, the stimulus can be written as a vector $\vec{s} = (s_1, s_2, \dots, s_N)$.

In the simplest case, the response is given by a one-dimensional output variable r , e.g., a firing rate or a spiking probability of a single neuron. A simple way to model the reduction from the N -dimensional stimulus \vec{s} to the one-dimensional response r is the application of a linear filter $\vec{k} = (k_1, k_2, \dots, k_N)$, which yields the scalar product

$$\vec{k} \cdot \vec{s} = \sum_{n=1}^N k_n \cdot s_n. \quad (4.1)$$

As in the previous chapter, the filter \vec{k} determines the characteristics of stimulus integration by defining the relevant direction in stimulus space. Adding an output nonlinearity $g(\cdot)$, we obtain a Wiener system or LN cascade,

$$r = g(\vec{k} \cdot \vec{s}). \quad (4.2)$$

Such systems are often used to model single-cell behavior (see Chapter 3), and their components can be identified by standard correlation methods such as spike-triggered average (Chichilnisky, 2001). The latter is not true any longer if one allows for an additional input nonlinearity $h(\cdot)$,

$$r = g(\vec{k} \cdot h(\vec{s})), \quad (4.3)$$

where $h(\cdot)$ acts on the individual components of \vec{s} ,

$$h(\vec{s}) = (h(s_1), h(s_2), \dots). \quad (4.4)$$

This can be viewed as a redefinition of the stimulus variable, e.g., a nonlinear change of units. In fact, there may be no reason to assume *a priori* that the system actually integrates over the stimulus variable \vec{s} that is handled by the experimenter, and not some transform $h(\vec{s})$ of it. We can thus give the following interpretation for the building blocks that lead to Eq. 4.3: The input nonlinearity $h(\cdot)$ determines “what” the system integrates, whereas the filter \vec{k} determines “how” this integration is performed (Gollisch and Herz, 2003c);

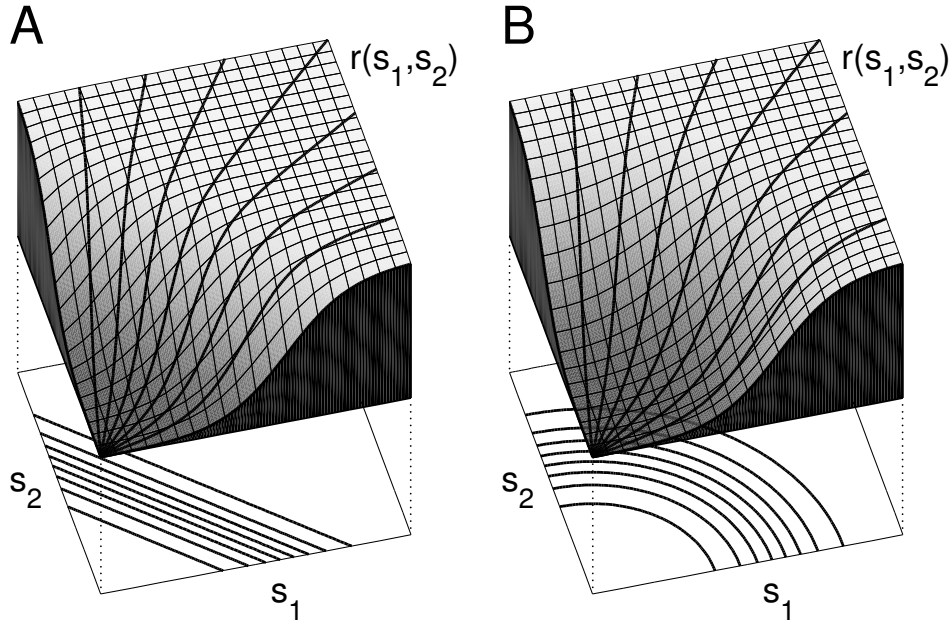


Figure 4.2: Effect of an input nonlinearity in an NLN cascade. A two-dimensional stimulus space is parametrized by the variables s_1 and s_2 , and the depicted surfaces represent the resulting response $r(s_1, s_2)$ for two alternative models, which take the linear (A) and the quadratic sum (B) as the argument of a sigmoidal nonlinearity. Although the two scenarios are fundamentally different, they both produce exactly the same one-dimensional response functions $r(s_1)$ and $r(s_2)$, respectively, as seen by the black areas at the sides of the surface blocks. Furthermore, any measurement along a radial direction, as is common in experimental practice, will produce similar sigmoidal response curves in both cases as seen by the thick black lines running along the surfaces. The contour lines drawn below the surface plots, however, give a clear signature of the different underlying processes. These lines can be traced out by measuring iso-response sets.

the output nonlinearity $g(\cdot)$, on the other hand, can be viewed as a mere recoding of the integration result. The full model of Eq. (4.3) is an NLN cascade, which explicitly contains two nonlinear transformations, as shown in Fig. 4.1.

Figure 4.2 exemplifies the effect of an input nonlinearity. Two models with just two input components s_1 and s_2 are compared. The first model is an LN cascade, the second contains an additional quadratic nonlinearity. The output nonlinearities are $g(x) = \tanh(x)$ for the first model and $g(x) = \tanh(\sqrt{x})$ for the second. The two models thus read

$$1) \quad r(s_1, s_2) = \tanh(s_1 + s_2), \quad (4.5)$$

$$2) \quad r(s_1, s_2) = \tanh(\sqrt{s_1^2 + s_2^2}). \quad (4.6)$$

If there is only a single input component, e.g. if $s_2 = 0$, the square root cancels the square of the input nonlinearity so that the response curves $r(s_1)$ are identical for both models. Measuring such one-dimensional response functions is thus not sufficient to test for input nonlinearities.

The question how such nonlinearities can be directly determined is answered by viewing the projections of the contour lines below the response surfaces. The contour lines of

the first model are straight lines, those of the second model are segments of circles. These lines thus contain clear signatures of the relevant variable on which the linear filter (in this case the simple summation) operates. Tracing out such contour lines experimentally by measuring iso-response sets is thus suited to identify input nonlinearities.

The reason why IRS are so sensitive to input nonlinearities lies in their independence of the output nonlinearity. Assume that we measure the IRS for a response \bar{r} for which the output nonlinearity $g(\cdot)$ is injective, i.e., there exists a unique x so that $g(x) = \bar{r}$. The output nonlinearity $g(\cdot)$ then acts on all stimuli within the IRS in the same way. In other words, the iso-response condition $g(\vec{k} \cdot h(\vec{s})) = g(\vec{k} \cdot h(\vec{s}^*))$ for two stimuli \vec{s} and \vec{s}^* in the IRS directly implies $\vec{k} \cdot h(\vec{s}) = \vec{k} \cdot h(\vec{s}^*)$. This equation determines the composition of the IRS independently of $g(\cdot)$. If the output nonlinearity is not injective for the measured response, the IRS may contain several branches corresponding to different values of $\vec{k} \cdot h(\vec{s})$. This may complicate the interpretation, but does not preclude it, as long as these branches are distinct in stimulus space. On the other hand, if $g(\cdot)$ maps large regions onto the same value, such as onto the value zero if $g(\cdot)$ contains a threshold rectification, then such values are apparently not suited to identify input nonlinearities.

To apply such an analysis in an experimental situation, we therefore need to determine different stimuli that lead to the same response. A typical way how this can be achieved is to fix all but one degree of freedom of a stimulus and tune the remaining free parameter until the desired response is reached. This free parameter defines the direction of search for iso-response stimuli. Efficiency of the experiment is vastly increased if online analysis of the responses and direct feedback to the stimulus generation are possible. In situations where the response depends monotonically on the free parameter at least over a fairly large range, simple algorithms such as interval bisection or gradient descent should suffice. How this is applied in practice to experimental data is shown in Chapter 5. In the next two sections, we will investigate two extensions of IRS measurements.

4.2 CIRS – Comparison of Iso-Response Stimuli

After having analyzed an input nonlinearity in the previous section, we now focus on the involved linear filters of a cascade. The fact that each stimulus in an IRS leads to the same response directly translates into a set of equations that can be used to extract model parameters such as the filter components. Consider again the NLN cascade introduced in Section 4.1 and assume that the input nonlinearity $h(\cdot)$ has been successfully identified by observing the shape of a particular measured iso-response set. Assume further for simplicity that the output nonlinearity $g(\cdot)$ is injective. For two stimuli $\vec{s}^{(1)}$ and $\vec{s}^{(2)}$ within the IRS, the iso-response condition then yields

$$\vec{k} \cdot h(\vec{s}^{(1)}) = \vec{k} \cdot h(\vec{s}^{(2)}). \quad (4.7)$$

This equation constrains one degree of freedom for the filter \vec{k} , and by including further stimuli from the IRS, \vec{k} can be completely determined. Essentially, this amounts to a quantitative comparison of the parameters of different iso-response stimuli. As shown in the following, comparing the measurements for N stimuli of the IRS is, in fact, sufficient to determine \vec{k} up to a multiplicative constant. We can formalize the procedure for

determining \vec{k} by writing the equations in matrix form

$$\mathbf{H} \cdot \vec{k} = c \cdot \vec{1}, \quad (4.8)$$

where $\vec{1}$ is the vector $(1, 1, \dots, 1)$, c is the undetermined value of $\vec{k} \cdot h(\vec{s})$ within the IRS, and \mathbf{H} is the matrix with components $H_{mn} = h(s_n^{(m)})$ obtained from the n -th component of the m -th stimulus in the IRS; $m, n = 1 \dots N$. The free parameter c could in principle be absorbed into the definition of either $h(\cdot)$, \vec{k} , or $g(\cdot)$. In the analysis of the LNLN cascade in Chapter 6, however, it will reappear as a significant model parameter. If the matrix \mathbf{H} has full rank, i.e., the inverse \mathbf{H}^{-1} exists, Eq. (4.8) can be solved for \vec{k} . Whether this is the case need not be a question of luck; it can be achieved by restricting the search of iso-response stimuli to particular directions which are independent in the transformed stimulus space, i.e., in the space spanned by the components $h(s_n)$. An example of such a choice of the search directions leading to a system of equations with simple solutions is presented in Chapter 6.

Note that mathematically the simplest solution is to perform measurements with single stimulus components, i.e., where always a different s_n is the only non-zero component of the stimulus. Practically, though, this may often not be possible. For example, such extremely “peaked” stimuli may be difficult to generate. More fundamentally, it may not be possible to achieve the required output with specific single components. For example, if the IRS for a neural system is defined by the occurrence of a spike in a certain time window after the stimulus, an early single intensity peak may already lead to a spike before the end of the stimulus and cause the neuron to go into refractoriness.

The experimental acquisition of suitable data for applying the CIRS method will be detailed in Chapter 6. In this chapter, the method will be used to dissect an LNLN cascade and to extract the components of *two* linear filters. The slightly more complicated calculation in this particular situation is based on the same generic idea as presented here.

4.3 DIRS – Disequilibrating Iso-Response Stimuli

Let us now turn to a method that takes iso-response stimuli in a steady state as a starting point and disequilibrates the dynamic processes in the system by “jumping” from one such stimulus to another. Imagine, e.g., that we have identified two stimuli for which the steady-state firing rates are equal. The fact that the system’s final output is the same does not mean that all sub-processes take on the same equilibrium states for both stimuli. In fact, they may even have to take on different states in order to compensate different levels of external input. If a process has different equilibrium states for the stimuli, switching between the stimuli will disequilibrate the system until all processes have regained a (possibly new) steady state. Although the final steady-state level of the output is the same as before the stimulus switch (if no hysteresis effects are present), the deviations from equilibrium right after the switch can be used to assess characteristics of the involved sub-processes.

Let us make the scenario discussed above more concrete. The described situation occurs if a neuron contains different adaptation processes that depend on the neuron’s input and output, respectively. To illustrate how disequilibrating iso-response stimuli can

be used to analyze such a system, we investigate a minimal model that contains input-driven as well as output-driven adaptation. In the model, the output activity (firing rate R) is a function of the input intensity I and two adaptation components A_R and A_I . As it has recently been shown that many different types of adaptation can phenomenologically be captured by subtractive contributions to the input current (Benda and Herz, 2003), we describe the model by the following three equations,

$$\begin{aligned} R &= g(k \cdot I - A_R - A_I), \\ \tau_R \cdot \frac{dA_R}{dt} &= A_{R,\infty}(R) - A_R, \\ \tau_I \cdot \frac{dA_I}{dt} &= A_{I,\infty}(I) - A_I. \end{aligned}$$

The function $g(\cdot)$ describes the neuron's tuning curve and may include rectification and saturation. k incorporates the neuron's tuning, i.e., its preference for a particular type of stimuli (such as certain sound frequencies or spatial locations of a visual stimulus) independent of the intensity; if the neuron is more sensitive to a particular stimulus, k will be larger. A_R and A_I are two adaptation components. They have a subtractive influence on the input I . However, this is not essential for the following discussion; different relations, such as divisive effects, lead to a very similar behavior of the model. dA_R/dt and dA_I/dt symbolize the temporal derivatives of A_R and A_I , respectively, leading to first-order differential equations that capture the build-up and decay of adaptation. Note that in this minimal model R is not given by a differential equation, but by an instantaneous function of I , A_R , and A_I . This can be viewed as a quasistatic approximation, which is valid if the time constants of adaptation, τ_R and τ_I , are considerably longer than those governing the dynamics of R , e.g., cell-membrane or synaptic time constants (cf. Shriki et al., 2003).

The important difference between A_R and A_I is that the saturation values $A_{R,\infty}$ and $A_{I,\infty}$ depend on the firing rate R , the neuron's output, and on the intensity I , the neuron's input, respectively. Without losing its essential features, the above general model can be solved analytically by assuming that the input-output relation $g(x)$, and the dependences of the adaptation components on R and I are all linear. The solutions provide insight into the dynamic behavior of the two different adaptation components. For $g(x) = x$, $A_{R,\infty}(R) = \alpha \cdot R$, and $A_{I,\infty}(I) = \beta \cdot I$, with α and β proportionality constants, the mathematical solution is given in Appendix B and shown graphically in Fig. 4.3.

The adaptation terms A_R and A_I have similar effects for constant stimuli. Both tend to decrease the firing rate over time until a steady state is reached. Since input intensity I and output firing rate R are usually tightly coupled (for higher intensity, the firing rate is also higher), both processes tend to work in the same direction. If the time constants τ_R and τ_I are also similar, the two types of adaptation will be hard to distinguish. But for a biophysical interpretation or for understanding the response to dynamic, fluctuating stimulation, such a distinction will be important. How can we test, e.g., if an input-driven adaptation component such as A_I is present?

Two stimuli for which the neuron has different sensitivity (here modeled by using values $k_x = 1$ and $k_y = 0.5$) can elicit the same steady-state firing rate if the intensities are tuned accordingly (Fig. 4.3A). Although the contribution of A_I to the total adaptation is

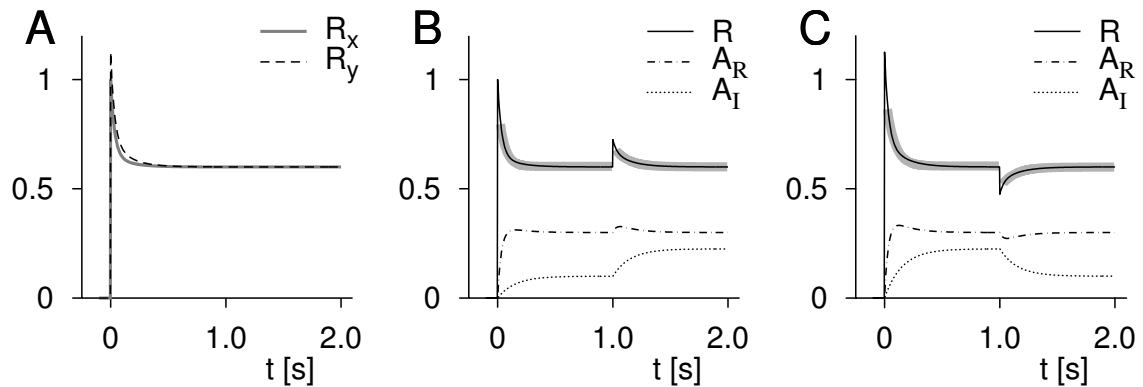


Figure 4.3: Dynamics of a minimal neuron model containing input-driven and output-driven adaptation. The firing rates and adaptation components are calculated according to the model introduced in the main text (solutions can be found in Appendix B) with time constants $\tau_R = 50$ ms, $\tau_I = 150$ ms and constants $\alpha = 0.5$, $\beta = 0.1$. Two stimuli x and y were used for which the model had different sensitivities given by $k_x = 1$ and $k_y = 0.5$. (A) Firing rates R_x and R_y for the two stimuli under constant stimulation. The two intensities are chosen such that the firing rates in the steady state are the same for both stimuli ($I_x = 1$ and $I_y = 2.25$ according to the steady-state equations in Appendix B). The initial firing-rate transients following stimulus onset reveal slight differences between the two curves. (B) Firing rate R and the two adaptation components A_R and A_I for a stimulation where the stimulus is switched from x to y at time $t = 1$ s. A_I approaches its new equilibrium value towards the end of the observation time, whereas A_R only features a slight upward excursion as a secondary effect. The firing rate shows a pronounced upward deflection following the switch that can be used to characterize the dynamic properties of the adaptation component A_I . The thick gray curves underlying the firing rate are exponential fits to the data leading to time constants of 53 ms following stimulus onset and 118 ms after the switch. (C) Same as B, but at time $t = 1$ s, the stimulus is switched in the other direction, from y to x . Consequently, the deflection of the firing rate is in the downward direction. The time constants obtained from the exponential fits are 71 ms following stimulus onset and 118 ms following the switch.

quite different in the two cases due to the difference in intensity, the time courses of the firing rates are very similar. When we include a switch between these iso-response stimuli, however, the A_I component is suddenly disequilibrated, as I takes on a different value. While A_I subsequently approaches its new equilibrium value, the firing rate reacts with a transient upward or downward deflection (Fig. 4.3B and C). Due to this temporary change of the firing rate, the adaptation component A_R also shows a small transient deflection and then resumes its original steady-state value. This is, however, a secondary effect; no deflection of A_R or R would occur without the component A_I .

The upward or downward deflection of the firing rate following switches between iso-response stimuli can be used to identify an input-driven adaptation component A_I . Its particular features, such as strength and time constant, can also be characterized. At the switch, the response transient is mostly determined by the dynamics of A_I , since A_R stays near its equilibrium point all the time. Note, however, that we also see from the model that the small secondary response of A_R does not allow a complete separation of the two adaptation processes. In the model, we used time constants $\tau_R = 50$ ms and $\tau_I = 150$ ms. From exponential fits of the firing-rate transients following onset and switch, we obtained time constants of 53 ms and 71 ms for the two stimulus onsets indicating that initially the faster and stronger adaptation component A_R dominates. Following the switch, we find a time constant of 118 ms in both cases, which still reflects the mixture of the two processes.

However, A_R stays near enough to its equilibrium value that the longer time constant τ_I is revealed and an order-of-magnitude estimate of τ_I is possible.

Experimentally, the DIRS method requires accurate tuning of the steady-state response so that the identified stimuli indeed share the same equilibrium states of the output-driven processes. In the experimental situation, this tuning, of course, relies on noisy data and will therefore never be perfect. An important aspect of the method is thus to develop an understanding of how inaccuracies in the tuning affect the deflections of the response induced by the switch. Chapter 8 contains a detailed experimental study based on the DIRS method where these issues regarding the tuning of stimuli are discussed.

4.4 Conceptual Discussion

The ideas that have been presented in this chapter are based on the ability to determine stimuli causing a predefined response. This requires that the more traditional perspective – a fixed stimulus is set and the resulting response measured – is given up and instead the response is pre-set and the required stimulus is extracted from the measurements. To apply this concept efficiently in an experimental setting, control of the stimulus generator by feedback from the recorded response may be necessary. This includes efficient and reliable tools for automatic online analysis of the response and suitable algorithms for fast tuning of the stimulus. The increasing use of ever-growing computer resources in the laboratory could provide the basis for speedy tracking of more and more complex iso-response sets.

As stated earlier, the measurement of iso-response stimuli in itself is not entirely new, as it is commonly used to measure tuning curves and assess psychophysical performance. Interesting analogies with our framework are also found by comparing it to the technique of *silent substitution* (Estévez and Spekreijse, 1982). Here, the spectral composition of a visual stimulus is varied systematically such that the resulting stimuli always lead to the same activity of one (or more) receptor types in the retina. Fluctuations in visually evoked potentials can then be interpreted as being caused by the remaining receptors. In this case, though, the iso-activity regions of the receptors are not explored, but must be accurately known beforehand.

CHAPTER SUMMARY:

General methods to identify and characterize cascade models so far only exist for specific, fairly simple model structures and are usually limited in temporal resolution. The experimental extraction of iso-response sets in stimulus space, as introduced in this chapter, can help overcome these limitations. The structure of iso-response sets may be directly used to identify an input nonlinearity and separate it from a second nonlinear transformation in the final output step. Extending this concept by quantitatively comparing iso-response stimuli, one can also determine the characteristics of linear filters that are part of a cascade with two nonlinearities. Finally, different dynamic processes in the system can be separated into input-driven and output-driven components by disequilibrating iso-response stimuli, i.e., by switching between different stimuli that have the same steady-state response.

CHAPTER 5

SPECTRAL INTEGRATION

Auditory receptor cells pick up sound. In a loosely spoken sense, their activity reflects “how loud” a sound is. Can we make this statement more precise? To do so, we must ask what it means for the cell that a sound is “loud”. In a way, a receptor cell is a measuring device. When we measure, e.g., “how much electricity” flows through a cable, we do so with specific measuring devices that pick up the voltage along the cable, or the current that flows through it, or possibly the power that is dissipated along the cable. We know which quantity we measure because we (or someone else who handed the information to us) built the measuring device in a specific way to do just this. In order to understand the read-out of the device, it is essential to know which component of electricity is measured.

Similarly for the receptor cell, we must find out which component of sound is measured in order to understand its read-out, i.e., its firing pattern. This question lies at the center of investigating spectral integration. If we can identify how the cell integrates the intensities of different frequency bands in a stationary sound signal, we can determine the relevant stimulus attribute of the sound pressure wave. To do so, we measure iso-response sets of stimuli with different spectral components and compare them with several hypotheses about what in the sound is picked up by the receptor cell.¹

5.1 *Relevant Stimulus Attribute*

The question of the appropriate measure of auditory stimuli has a long tradition. It has mainly been investigated, though, in connection to temporal integration, i.e., how stimulus intensities are combined over time. Several psycho-acoustic studies have analyzed intensity-duration trade-offs in sound perception. The results mostly suggest that the stimulus energy is the crucial variable (Garner, 1947; Plomp and Bouman, 1959; Zwislocki, 1965; Florentine et al., 1988). However, the long time constants required to fit the data (several hundred milliseconds) are difficult to reconcile with the high temporal resolution of the auditory system. This has been expressed in the *resolution-integration paradox* (de Boer, 1985). In electrophysiology, a recent investigation of first-spike latencies in mammalian auditory-nerve fibers finds the time-integrated pressure as the decisive stimulus attribute (Heil and Neubauer, 2001). In insect auditory receptor cells, on the other

¹This chapter is based on (Gollisch et al., 2002).

hand, the differences between thresholds for one- and two-click stimuli and intensity-duration trade-offs have been investigated and found to be consistent with temporal energy integration (Tougaard, 1996; Tougaard, 1998).

If one aims at drawing conclusions about the auditory transduction process, care must be taken in the interpretation of temporal-integration phenomena because several other biophysical processes, such as internal calcium dynamics and spike generation, are involved besides the primary signal transduction. Spectral integration, on the other hand, depends, at least for high-frequency sounds, almost exclusively on the mechanosensory transduction process; any fluctuations on the several-kilohertz scale that were still present after the transduction (i.e., in the cell-membrane conductance) would be highly attenuated by the cell membrane's low-pass-filter properties (Koch, 1999). Looking at spectral integration instead of temporal integration therefore enables us to focus on the site of mechanosensory transduction and analyze the functional properties of this particular module within the auditory transduction chain.

To investigate spectral integration, we focus on stationary stimuli, which can be described by their power spectra and phase spectra. This high-dimensional stimulus space is essentially mapped onto a one-dimensional output variable, the neuron's firing rate. Due to this dimensional reduction, we can expect from the very outset to find different spectral compositions of stationary sounds that yield the same firing rate. We can thus directly apply the measurement of iso-response sets to investigate spectral integration in auditory receptor cells and test hypotheses about the stimulus attribute extracted by this measuring device.

5.2 Three Hypotheses

In order to investigate the effects of potentially relevant stimulus attributes on spectral integration, we first develop a descriptive model for the responses of auditory receptor neurons to stationary stimuli with arbitrary power spectrum. The model comprises a sequence of three steps, which correspond to the coupling, the transduction, and the encoding of the primary signal (Eyzaguirre and Kuffler, 1955; French, 1992). We investigate three alternative hypotheses about which stimulus property governs the transduction process: the maximum amplitude of the stimulus, the stimulus energy, and the average half-wave-rectified signal amplitude.

Let us begin the derivation of the model by recalling that the rate-intensity functions measured in locust auditory receptor cells have a common shape, regardless of the carrier frequency (Fig. 2.5). This finding can be captured by a simple linear filtering mechanism: Let us assume that for all pure tones the firing rate r is given by a single function $r = g(A_n/C_n)$ of the sound pressure amplitude A_n scaled by a filter constant C_n . For two different pure tones, the firing rates $r_1 = g(A_1/C_1)$ and $r_2 = g(A_2/C_2)$ are then the same when $A_1/C_1 = A_2/C_2$, i.e., when the amplitudes take on a constant ratio $A_1/A_2 = C_1/C_2$. Since the intensity I in dB SPL is defined as a logarithmic measure of the amplitude, $I = 20 \log_{10} \left(A / (\sqrt{2} \cdot 20 \mu\text{Pa}) \right)$, this constant amplitude ratio corresponds to a constant intensity difference, $\Delta I = I_1 - I_2 = 20 \log_{10}(C_1/C_2)$. The rate-intensity functions are thus shifted versions of one another separated by ΔI as found in the experiment.

The above reasoning for the presence of a linear filter corresponds well with the biophysical findings regarding the tympanum. Schiolten et al. (1981) observed that the tympanum behaves approximately as a linear oscillator with a short damping time constant of about 100 μ s, and Michelsen and Rohrseitz (1995) noted that the amplitude of the tympanic vibration depends linearly on the sound pressure for pure tones.

Generalizing the linear filtering to stimuli containing more than one frequency leads us to the first step of our model:

Step 1: Coupling to the Stimulus

The sound pressure wave $A(t)$ can be written as a Fourier series

$$A(t) = \sum_{n=1}^N A_n \sin(2\pi f_n t + \varphi_n), \quad (5.1)$$

where the f_n denote the frequencies, φ_n phase offsets, and the A_n the respective amplitudes. This stimulus is initially transformed into a filtered signal $\tilde{A}(t)$:

$$\tilde{A}(t) = \sum_{n=1}^N \frac{A_n}{C_n} \sin(2\pi f_n t + \tilde{\varphi}_n). \quad (5.2)$$

The amplitudes are multiplied by frequency-dependent gain factors $1/C_n$. These describe the frequency-resolved sensitivity, i.e., the tuning of the receptor cell, and correspond directly to the values of the threshold curve at the frequencies f_n . In addition, a putative phase shift turns φ_n into $\tilde{\varphi}_n$.

Step 2: Mechanosensory Transduction

The above filtering describes the coupling of the air-pressure fluctuations to the tympanum. Subsequently, the tympanic oscillations lead to conductance changes in the receptor cells' dendrites that give rise to membrane depolarizations. This is where a spectral integration of frequency-dependent stimulus attributes must occur; voltage fluctuations in the range of the relevant sound frequencies (several kilohertz) cannot be transmitted by the cell membrane due to its low-pass filter properties. Information about the spectral content is therefore lost at the level of the membrane potential, which, instead, is expected to correspond to an integrated stimulus property. This is supported by the observation that the spectrum of the membrane potential following acoustic stimulation contains no trace of the applied sound frequency (Hill, 1983).

Following ideas from the literature concerning temporal integration in auditory receptor cells (Tougaard, 1996; Heil and Neubauer, 2001), we set up three hypotheses for the spectral integration by calculating an "effective sound intensity" J from $\tilde{A}(t)$.

Amplitude Hypothesis (AH): J corresponds to the maximum amplitude of $\tilde{A}(t)$. This is the common view of a threshold; a response occurs once the signal reaches a certain value. In the case of few frequency components, J is given by the sum of the scaled amplitudes:

$$J_{AH} = \sum_{n=1}^N \frac{A_n}{C_n}. \quad (5.3)$$

Energy Hypothesis (EH): J corresponds to the temporal mean of the squared signal (throughout what follows, $\langle x(t) \rangle$ denotes the temporal mean of $x(t)$):

$$J_{EH} = \langle \tilde{A}(t)^2 \rangle. \quad (5.4)$$

From Parseval's Theorem, we see that this expression can be rewritten as the sum of the squares of the scaled amplitudes:

$$J_{EH} = \frac{1}{2} \sum_{n=1}^N \frac{A_n^2}{C_n^2}. \quad (5.5)$$

Since the square of the amplitude of a sinusoidal oscillation is proportional to the energy contained in the oscillation, this hypothesis reflects an energy-integration mechanism.

Pressure Hypothesis (PH): J corresponds to the temporal mean of the absolute value of $\tilde{A}(t)$:

$$J_{PH} = \langle |\tilde{A}(t)| \rangle. \quad (5.6)$$

This hypothesis complies with a pressure-integration mechanism after half-wave rectification.

Step 3: Encoding by Firing Rates

The response of an auditory receptor cell to a signal of constant intensity can be characterized by a mean firing rate r . The rate is obtained from a one-dimensional, nonlinear transformation of the effective sound intensity J :

$$r = g(J). \quad (5.7)$$

Looking at the model structures for the three hypotheses, we see that the amplitude hypothesis mathematically corresponds to an LN cascade (linear summation of the amplitudes followed by the nonlinearity $g(J)$) and that the energy hypothesis corresponds to an LNLN cascade (each component scaled by C_n , then squared before the summation; the nonlinearity $g(J)$ transforms the result). The pressure hypothesis as expressed in the time domain, Eq. (5.6), also corresponds to an LNLN cascade (scaling, rectification, then summation or integration over time, finally transformation by $g(J)$); in the frequency domain, however, the rectification cannot be modeled by a static nonlinear transformation, but becomes a dynamic nonlinear process, as different frequency components are mixed. This does not, of course, preclude its being tested with iso-response sets.

Measured spike-train responses feature strong transients due to adaptation. In a first approach, we averaged over this temporal structure in the response and only consider the

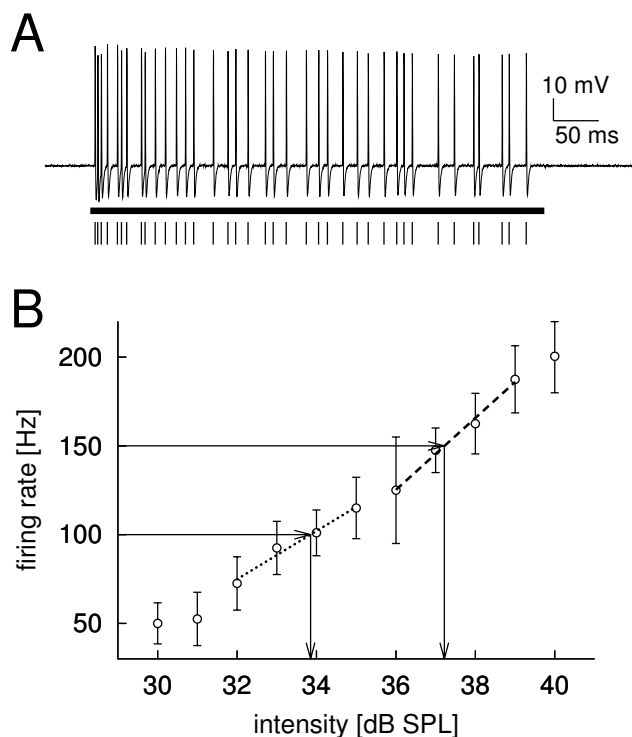


Figure 5.1: Determination of sound intensities corresponding to given firing rates. (A) Example of a spike train recorded intracellularly from an axon of a receptor cell. Scale bars are given to the right. The thick bar below the voltage trace denotes the 500-ms pure-tone stimulus. The vertical bars below show the spike times as determined by a spike-detection algorithm. The firing rate was calculated by counting the spikes and averaging over several stimulus repetitions. (B) Example of the rising part of a rate-intensity function (circles) measured in steps of 1 dB. Each stimulus was repeated multiple times. Vertical bars denote the standard deviation of each measurement. Linear fits through the four points closest to the firing rates of interest, here 100 Hz and 150 Hz, are depicted as dotted and dashed lines, respectively. The arrows indicate the read-out of the corresponding intensities. Figure adapted from (Gollisch et al., 2002) with permission.

total number of spikes elicited by the stimulus. In a second, more detailed analysis, we analyzed individual parts of the response in order to explicitly test how this structure in the spike trains might affect our model description.

5.3 IRS in a Two-Dimensional Stimulus Space

To directly address the question of spectral integration and the hypotheses in Step 2 of our model, we measured iso-response sets in the stimulus space (A_1, A_2, \dots) . The shape of the rate-intensity functions (Fig. 2.5) suggest that the firing rate $r = g(J)$ depends monotonically on the effective sound intensity. Hence, equal firing-rate responses, in terms of our model, imply equal effective sound intensities J and vice versa, independently of the specific shape of $g(J)$. Since the rate-intensity functions are found to be fairly smooth in the rising part between threshold and saturation, extracting iso-response sets can be accurately done by linear interpolation as is shown in Fig. 5.1.

Superpositions of Two Pure Tones

The complete stimulus space of stationary stimuli is, of course, very high-dimensional. We can begin, though, with low-dimensional sub-spaces using only two pure tones and their superpositions. A two-tone stimulus with frequencies f_1 and f_2 ,

$$A(t) = A_1 \sin(2\pi f_1 t) + A_2 \sin(2\pi f_2 t), \quad (5.8)$$

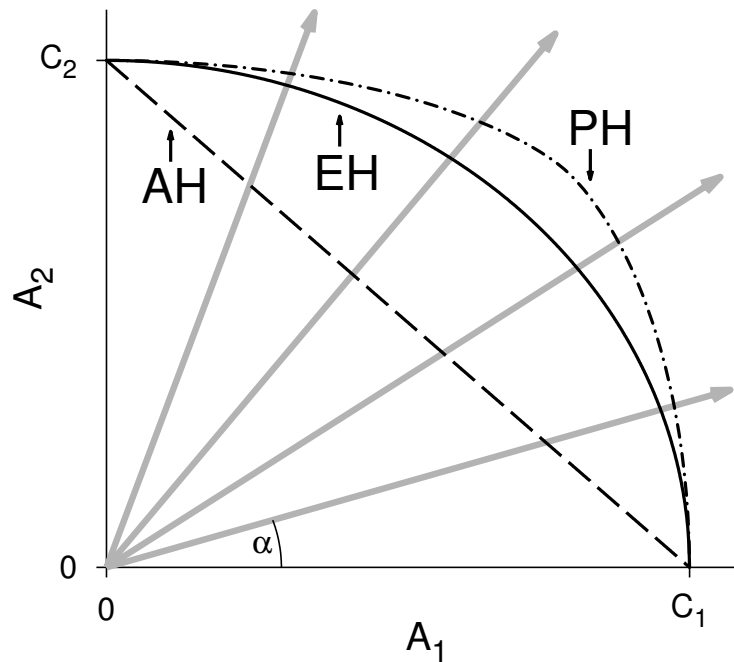


Figure 5.2: Prediction of iso-response sets for the superposition of two pure tones. Depending on the model, the effective sound intensity J as well as the firing rate are expected to be constant along different curves in the two-dimensional space of amplitude combinations. A_1 and A_2 denote the amplitudes of the respective components. According to the amplitude hypothesis (AH), iso-response curves are straight lines (one example shown by the dashed line), according to the energy hypothesis (EH), they are ellipses (solid line), and according to the pressure hypothesis (PH), they are even more strongly bent curves (dash-dotted line), whose exact shape has to be determined numerically. The scale of the axes is given by the filter constants C_1 and C_2 . Note that when the hypotheses are fitted to the data, the obtained filter constants will in general be different for each model, and the intersection points with the axes will not coincide because C_1 and C_2 are free parameters for each model. The gray arrows indicate equally spaced directions along which the rate-intensity curves are measured. In each direction, the intensity increases with increasing amplitudes A_1 and A_2 , whereas A_1/A_2 is kept fixed and determined by the angle α . (One example for this angle is denoted in the figure.) The intersection points of the arrows with the iso-response curves denote the amplitude combinations that are expected to yield the specified firing rate according to each of the three alternative hypotheses. Since the three intersection points on each gray arrow clearly differ from each other, the measurements of the iso-response sets can be used to distinguish between the hypotheses. Figure adapted from (Gollisch et al., 2002) with permission.

is represented by a point in the two-dimensional sub-space (A_1, A_2) . In this space, curves representing the expected iso-response sets for each of the three hypotheses can easily be calculated and are shown in Fig. 5.2. The linear summation of components for the amplitude hypothesis leads to a straight line along which the firing rate is expected to be constant, the summation of squares yields an ellipse for the energy hypothesis, and the corresponding curve for the pressure hypothesis results from numerical calculations. The different shapes of these curves illustrate that experimentally extracting iso-response sets can distinguish between the hypotheses.

Responses to superpositions of two pure tones with frequencies $f_1 = 4$ kHz and $f_2 = 9.55$ kHz and stimulus duration of 100 ms were measured for 17 cells. The frequencies

were chosen to be fairly far apart and incommensurate to avoid that the signal displays beating and depends on the relative phase of the components. For these stimuli, different amplitude combinations leading to the same firing rate were extracted by tuning the total intensity of stimuli with a fixed ratio of A_1 and A_2 . This corresponds to measuring along radial directions of the (A_1, A_2) space as indicated in Fig. 5.2. To make the acquired data most meaningful, these directions should be nearly equally distributed after rescaling the amplitudes by the filter constants C_1 and C_2 . This was achieved by first measuring the required amplitudes for the pure tones alone and taking these values as initial estimates of C_1 and C_2 . The directions for subsequent measurement were then chosen accordingly; the technical details can be found in Appendix C.

Results from four cells are presented in Fig. 5.3, where sets of amplitude combinations (A_1, A_2) are shown that led to a firing rate of 150 Hz. For each of the three hypotheses, the iso-response curves were fitted to the data by obtaining the free parameters C_1 and C_2 from a least-squares fit. Details of the fitting routine are given in Appendix D.

Statistical Analysis

Performing a standard χ^2 test on the fits of the three hypotheses showed that the amplitude hypothesis is rejected at the 1% level for all 17 cells while the energy hypothesis is not rejected for any cell and the pressure hypothesis is rejected for 4 cells. For an in-depth analysis, we therefore only considered the energy and the pressure hypotheses.

To further distinguish between these two hypotheses, we directly compared the goodness of fit given by the χ^2 values. The energy hypothesis yielded a lower χ^2 than the pressure hypothesis in 16 of the 17 cases. We also calculated a Bayesian estimate of the probability $p(\text{model}|\text{data})$ of the model given the data with prior probabilities of 0.5 for both the energy and the pressure hypothesis. This procedure is explained in detail in Appendix E. The mean of $p(\text{EH}|\text{data})$ was obtained as 0.884 with 0.167 s.d. and median 0.978 ($N = 17$), while $p(\text{PH}|\text{data})$ equals $1 - p(\text{EH}|\text{data})$ and therefore had a mean of only 0.116.

Furthermore, data points for which A_1/C_1 and A_2/C_2 were approximately equal (i.e., data points in the middle sections of the plots in Fig. 5.3) were in general below the fitted iso-response curve of the pressure hypothesis instead of scattered around it as would be expected if the deviations resulted from independent measurement errors. The statistical significance of such trends can be tested with a standard run test. To do so, the data points are subdivided into *runs*, i.e., sequences of points that lie consecutively either above or below the model prediction. The null-hypothesis is that the data points are scattered independently around the model prediction. Trends in the data generally lead to a reduction in the number of runs. The significance of this reduction can be calculated by comparison with the distribution of run numbers for the null-hypothesis (Barlow, 1989).

Since only data sets with a sufficient number of samples can form several runs, we investigated the number of runs only for cells with at least 12 data points (corresponding to 10 degrees of freedom, as two parameters were fitted). For these 9 cells, the run test showed significant deviations ($p < 0.01$) from the pressure hypothesis in 3 cases. All these 3 cells were different from those that had led to statistically significant deviations from the pressure hypothesis according to the χ^2 test. For the energy hypothesis, the data were consistent with independent scatter around the model prediction for all cells.

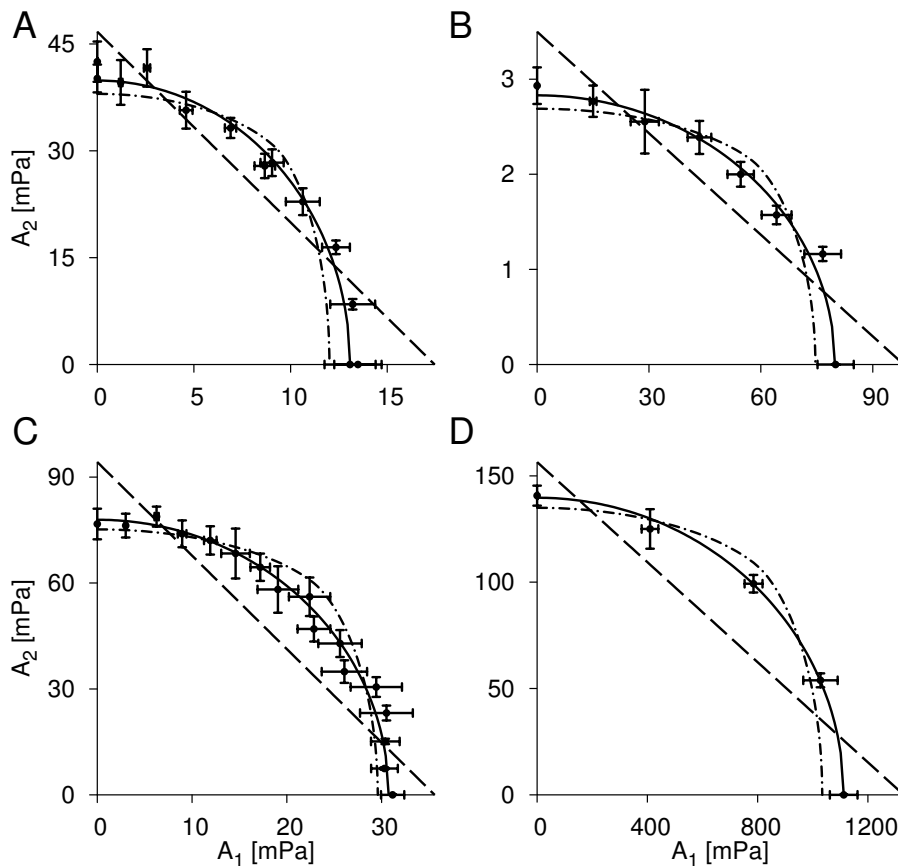


Figure 5.3: Iso-response sets for superpositions of two pure tones from four different receptor cells (**A–D**). The measured pairs of amplitudes corresponding to a firing rate of 150 Hz are shown together with the iso-response curves for the three hypotheses. For each curve, the two free parameters C_1 and C_2 were fitted to the data. The dashed lines denote the fits of the amplitude hypothesis, the solid lines the fits of the energy hypothesis, and the dash-dotted lines the fits of the pressure hypothesis. While the curves for the amplitude and the pressure hypothesis deviate systematically, the ellipse obtained from the energy hypothesis corresponds well with the data. Note the different scales on the axes between the four cells as well as between the x -axis and the y -axis of individual plots. These differences are due to the strong dependence of the sensitivity on the sound frequency and the specific cell. From the fits of the energy hypothesis, we obtain the following ratios C_1/C_2 in these four cases: 0.33 (**A**), 28.33 (**B**), 0.39 (**C**), and 7.96 (**D**). Although there is an almost 30-fold difference (corresponding to approximately 30 dB) between the amplitudes of the two tones in **B**, they contribute equally to the firing rate of the neuron. Also note that in **A** the amplitudes of the pure tones giving a firing rate of 150 Hz were measured twice (at the beginning and the end of the experiment) with the results approximately coinciding. Figure adapted from (Gollisch et al., 2002) with permission.

From the combined evidence, we conclude that the amplitude as well as the pressure hypotheses can be rejected. The energy hypothesis, on the other hand, provides a good description of the data for spectral integration in the two-tone case.

IRS for Different Firing Rates

As an additional test of the energy hypothesis, we investigated how iso-response sets that were obtained separately for different firing rates are related to one another. Fig. 5.4

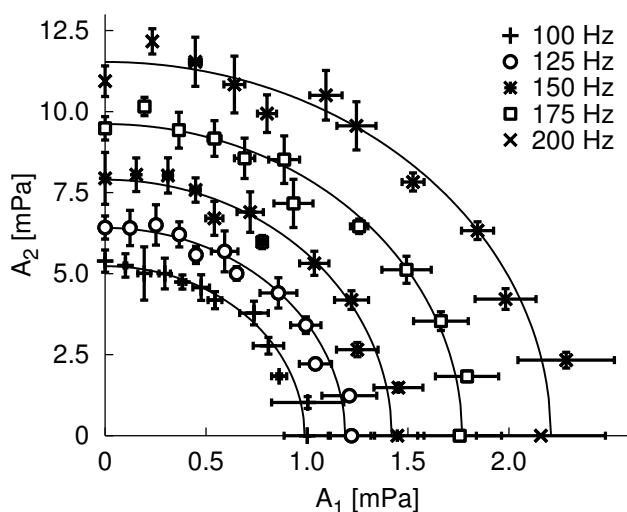


Figure 5.4: Iso-response sets for superpositions of two pure tones from one receptor cell at different firing rates. The points display measured pairs of amplitudes, and the solid lines are corresponding ellipses fitted to the data in accordance with the energy hypothesis. The firing rates rise from 100 to 200 Hz in steps of 25 Hz. Note that the fits agree with the data regardless of the firing rate and that ellipses for different firing rates are scaled versions of each other as predicted by the energy hypothesis. The ratios C_1/C_2 lie in the narrow range between 0.177 and 0.185 for all five firing rates. Figure adapted from (Gollisch et al., 2002) with permission.

shows pairs (A_1, A_2) corresponding to several firing rates between 100 and 200 Hz. Pairs corresponding to the same firing rate are accurately fitted by ellipses. Each ellipse corresponds to an independent fit to those data points that belong to the same firing rate. We find that all ellipses are nearly scaled versions of one another. This result is in accordance with the energy hypothesis, as the ratio of the ellipses' half-axes should always equal the ratio of the filter constants C_1 and C_2 . Such a behavior was observed for all cells that we measured. To quantify this, we determined for each cell the ratios R_{100} and R_{150} of the ellipses' half-axes corresponding to 100 and 150 Hz, respectively, and their relative deviations $|(R_{150} - R_{100})/R_{150}|$. We found that with a mean of 0.044 (s.d. 0.026), these were always small.

5.4 Influence of Adaptation

Up to now, we have disregarded the fact that the spike-train responses contain a pronounced transient due to spike-frequency adaptation. Typical spike trains from receptor cells for 300-ms pure-tone stimuli and the corresponding instantaneous firing rates can be seen in Fig. 5.5A and E. After the first few hundred milliseconds, adaptation is completed, and the response is approximately in a stationary steady state for the rest of the stimulus duration. When the stimulus ends, the receptor cells do not show an offset response, but stop firing or return to their usually low spontaneous activity. In order to investigate how the transients influence our model description, we explicitly analyzed the validity of the hypotheses for the onset as well as the steady-state response.

Spike trains from 10 cells were recorded with stimuli of either 300-ms (in 6 cases) or 500-ms duration (in 4 cases). The same analysis as before was applied to the onset by using only the first 30 ms of the response and to the steady state by disregarding the first 200 ms after stimulus onset. Two examples are shown in Fig. 5.5. In each case, the data points are best fitted by the ellipses from the energy hypothesis. We again performed a statistical analysis of the goodness of fit. Longer stimulus durations resulted in fewer

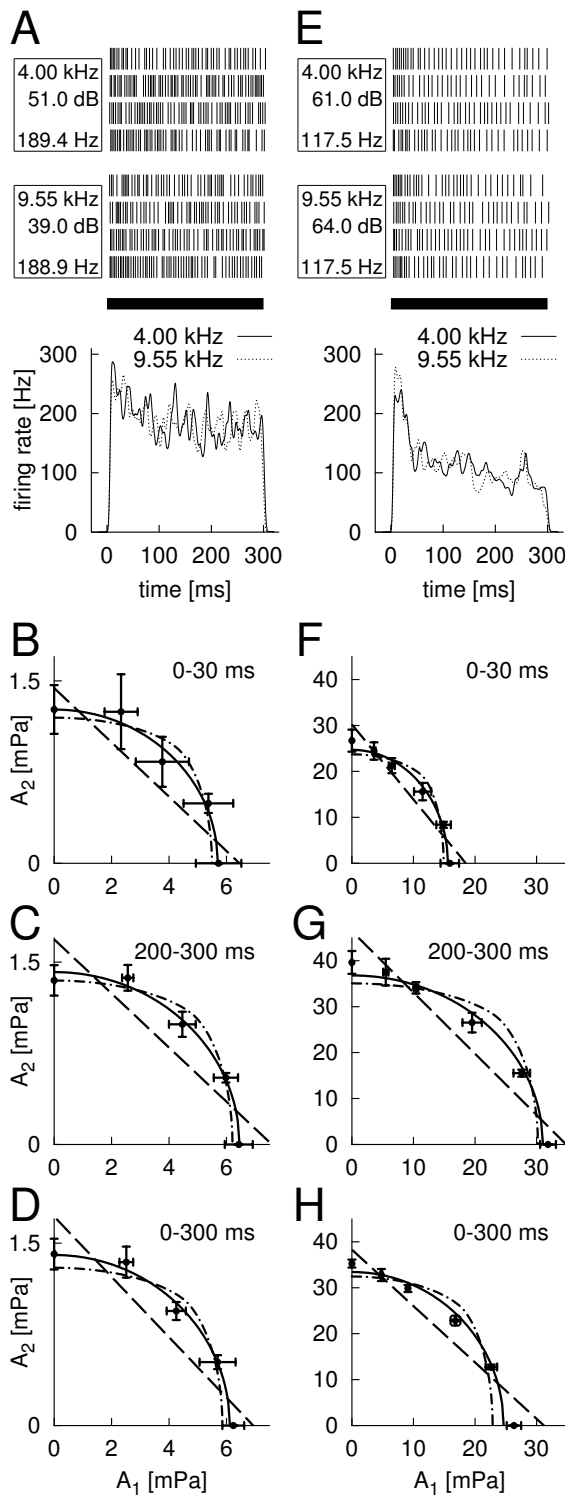


Figure 5.5: Responses and iso-response sets for two cells with stimuli of 300 ms. Each of the two columns (panels A–D and E–H, respectively) depicts results from a single cell. Panels A and E show four typical spike trains in response to pure tones with frequencies $f_1 = 4.00$ kHz (upper sections) and $f_2 = 9.55$ kHz (middle sections) as well as the corresponding instantaneous firing rates (lower sections). The sound frequency in kHz, and the intensity in dB of the stimulus as well as the elicited firing rate in Hz are indicated in the boxes to the left of the spike trains. The sound intensities for which the responses are shown were chosen such that the average firing rates approximately coincided for the two sound frequencies. The duration of the stimuli is denoted by the thick bars. The instantaneous firing rates were calculated by averaging over the inverse inter-spike intervals at each point in time and subsequently smoothed with a Gaussian of 2 ms standard deviation. One observes a strong transient in the first 100 ms. In addition, the cell depicted in panels E to H exhibited a slightly reduced firing rate in the first few milliseconds for the 4-kHz tone compared to the 9.55-kHz tone. Panels B–D and F–H show iso-response sets and fits of the three hypotheses for the two cells obtained from different episodes of the responses. The time window used for the analysis is denoted in each of the panels. Panels B and F capture the onset response of the first 30 ms. Panels C and G refer to the steady state, and panels D and H to the total response. The ellipses corresponding to the energy hypothesis (solid lines) lead to notably better fits of the data than the curves for the amplitude hypothesis (dashed lines) and the pressure hypothesis (dash-dotted lines), regardless of the analyzed response window. Figure adapted from (Gollisch et al., 2002) with permission.

measurements per cell so that the data points often had larger experimental errors. This effect is even stronger for the analysis of the onset response, which relies on considerably shorter stretches of data. Nevertheless, the data from two cells during steady state devi-

ated significantly ($p < 0.05$) from the pressure hypothesis, while the energy hypothesis always gave a good fit. Furthermore, the Bayesian test favored the energy hypothesis over the pressure hypothesis strongly for both onset and steady state ($p(\text{EH}|\text{data})$ for onset response: mean 0.642 with 0.100 s.d., median 0.649; $p(\text{EH}|\text{data})$ for steady state: mean 0.795 with 0.131 s.d., median 0.782; $N = 10$). We conclude that the energy hypothesis yields an appropriate description also for the specific episodes of the response.

How are the parameters of the model affected by adaptation? Apparently, the ellipses for the onset iso-response sets, Fig. 5.5B and F are smaller than those for the steady state, Fig. 5.5C and G. This reflects the higher sensitivity of the neuron at stimulus onset; a lower sound amplitude is needed for obtaining the desired response than in the steady state. The parameters C_1 and C_2 obtained from fitting the ellipse are thus correspondingly larger in the steady state. An interesting question now is whether they become larger “in the same way”, i.e., by the same scaling factor. This would mean that the ellipse for the steady state is just a scaled version of the onset ellipse.

Such a scaling relation is expected for many common cellular mechanisms of spike-frequency adaptation, which are triggered by the spiking activity of the neuron itself and act as an additional current source (Benda and Herz, 2003). This type of output-driven adaptation takes place after spectral integration in the transduction chain and thus only affects the absolute level of sensitivity.

Comparing Fig. 5.5F and G, though, we see that this scaling relation might be violated. To investigate this more closely, we calculated the half-axes ratios $R = C_1/C_2$ of the filter constants for the onset, R_O , and for the steady state, R_S , for all cells. The relative change, $\Delta R = |R_O - R_S|/R_S$, provides information about the validity of the scaling relation. We found values of ΔR between 1 % and 25 %, which must be compared to the error measures for the values of R of around 10 %. Half of the cells had a ΔR value that was larger than their noise level. The change in the half-axes ratio R is thus comparable to the accuracy with which it could be estimated, and it is generally much smaller than the change in the half axes themselves, which was found to lie between 10 and 50 % with error measures of 5 to 10 %. Nevertheless, single examples such as the one in the right column of Fig. 5.5 hint at the possibility that the half-axes ratio between onset and steady state is not conserved, which would suggest the presence of an adaptation component that acts before the spectral-integration step. Nevertheless, the energy hypothesis holds for stimulus onset and steady state separately, and adaptation only influences the exact values of the model parameters C_1 and C_2 . For the rest of this chapter, we thus use the firing rate obtained from the full response of the receptor cell. In Chapter 8, however, we will come back to the question of different adaptation mechanisms and investigate it in more detail with an alternative method.

5.5 IRS in a Three-Dimensional Stimulus Space

In order to see whether the findings from the two-tone experiments generalize to sounds with more complex frequency spectra, responses to superpositions of three pure tones were analyzed. We applied an analogous approach as for the two-tone experiments with

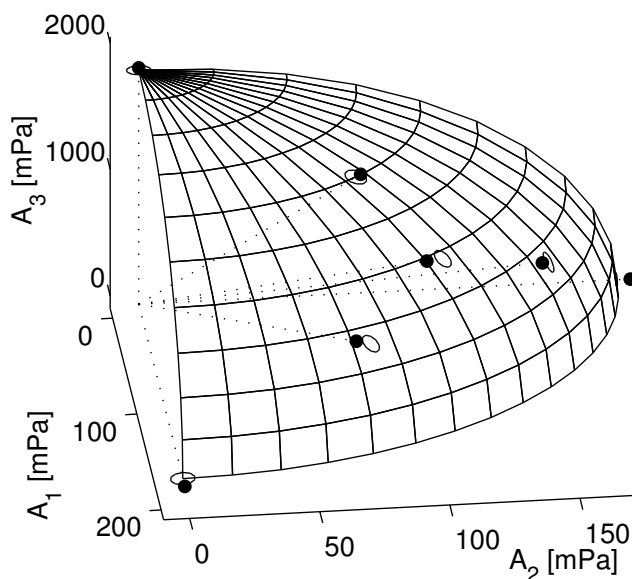


Figure 5.6: Iso-response surface for superpositions of three pure tones for one receptor cell. Amplitude triplets resulting in a firing rate of 150 Hz are shown as filled circles. The three-dimensional mesh displays an ellipsoid with the three half-axes fitted to the data and illustrates the prediction for the iso-response surface from the energy hypothesis. The filter constants obtained from the fit are $C_1 = 0.172$ Pa, $C_2 = 0.186$ Pa, and $C_3 = 1.88$ Pa. For optical guidance, the measured points are connected to the origin of the coordinate system by dotted lines. The intersection points of these lines with the ellipsoid are portrayed by open circles on the ellipsoid. For clarity, the iso-response surfaces corresponding to the amplitude and pressure hypotheses are not shown. Figure adapted from (Gollisch et al., 2002) with permission.

100-ms stimuli and identified iso-response sets for stimuli

$$A(t) = A_1 \sin(2\pi f_1 t) + A_2 \sin(2\pi f_2 t) + A_3 \sin(2\pi f_3 t) \quad (5.9)$$

in the three-dimensional sub-space (A_1, A_2, A_3) . We used two different sets of frequencies, either $f_1 = 4$ kHz, $f_2 = 9.55$ kHz, $f_3 = 15.20$ kHz or $f_1 = 6$ kHz, $f_2 = 8.59$ kHz, $f_3 = 17.22$ kHz with no apparent differences between the results for the two sets. The frequencies were again chosen to be fairly far apart and incommensurate to avoid beating and relative phase dependence. The three hypotheses yield predictions about the surfaces on which the iso-response sets are expected to fall. The surfaces have the form of a plane (amplitude hypothesis), an ellipsoid (energy hypothesis), and a more strongly bent surface (pressure hypothesis) whose exact shape has to be determined numerically.

Responses to superpositions of three pure tones were measured for 8 cells. From the rate-intensity functions, we determined amplitude triplets corresponding to a firing rate of 150 Hz. Fig. 5.6 illustrates the results for one cell and also shows the fitted ellipsoid corresponding to the iso-response surface of the energy hypothesis. A χ^2 test showed that the amplitude hypothesis is rejected at the 1% level for all 8 cells, while the energy hypothesis is rejected for 1 cell and the pressure hypothesis for 4 cells. We again compared the fits for the energy and the pressure hypothesis in more detail. In all cases, the energy hypothesis gave a lower χ^2 than the pressure hypothesis, and the Bayesian estimate of the probability of the models again strongly favored the energy hypothesis over the pressure hypothesis (mean of $p(\text{EH}|\text{data})$ was 0.916 with 0.109 s.d., median 0.987, $N = 8$). Thus, spectral integration for three pure tones is also best described by the energy hypothesis, while the amplitude and the pressure hypothesis are rejected by the data.

5.6 Test of Model Predictions for Noise-Like Stimuli

So far we have found that the energy hypothesis describes spectral integration of mixtures of two and three pure tones. We now pose the question whether this hypothesis also applies to stimuli composed of many frequencies. In particular, we aim at predicting the response to a band-pass-filtered Gaussian white noise based on the knowledge of the filter constants C_n and a pure-tone rate-intensity function. Spike-train responses to constant-intensity stimuli with broad-band carrier-frequency spectrum look in no way different than responses to pure-tone stimulation. We therefore again focus on the firing rate and measure rate-intensity functions for such a noise stimulus.

We have seen earlier that rate-intensity functions for pure tones have the same shape for different sound frequencies (Fig. 2.5). This could be explained by the model as a simple scaling effect induced by the filter constants C_n . A very similar argument tells us that, according to the model framework, the rate-intensity functions for the noise stimulus should also be a shifted version of that of the pure tone,

$$r^{\text{noise}}(I) = r^{\text{pt}}(I - \Delta I), \quad (5.10)$$

where $r^{\text{noise}}(I)$ and $r^{\text{pt}}(I)$ stand for the rate-intensity functions of the noise stimulus and the pure-tone stimulus, respectively. A mathematical derivation of this relation is presented in Appendix F. The calculation also leads to quantitative predictions for the expected shift ΔI_{EH} and ΔI_{PH} according to the energy and pressure hypotheses, respectively. These are given by

$$\Delta I_{EH} = -10 \log_{10} \left((C^{\text{pt}})^2 \frac{\sum_n \frac{A_n^2}{C_n^2}}{\sum_n A_n^2} \right) \text{ dB}, \quad (5.11)$$

$$\Delta I_{PH} = -10 \log_{10} \left(\frac{\pi}{4} (C^{\text{pt}})^2 \frac{\sum_n \frac{A_n^2}{C_n^2}}{\sum_n A_n^2} \right) \text{ dB} = \Delta I_{EH} - 10 \log_{10} \frac{\pi}{4} \text{ dB}. \quad (5.12)$$

The A_n denote the amplitudes of the different frequency components of the noise signal, and the C_n are the corresponding filter constants. C^{pt} stands for the filter constant of the pure tone. The values of the intensity shift for the two hypotheses differ only slightly by $-10 \log_{10}(\pi/4) \text{ dB} \approx 1.05 \text{ dB}$, and we therefore cannot expect that this experiment is suited for distinguishing between the two hypotheses. It nevertheless serves as a valuable test for the general framework.

In the experiments, the pure-tone stimulus had a frequency of 4 kHz, and the noise stimulus was band-pass filtered between 5 and 10 kHz, a region where many receptor cells are most sensitive. Rate-intensity functions for these two types of stimuli were measured for 10 cells. In addition, filter constants in the range of 5 to 10 kHz were determined independently for each cell by measuring the amplitudes of pure tones leading to a firing rate of 260 Hz. Figure 5.7 shows rate-intensity functions for the pure-tone as well as the noise stimulus together with the predictions that are obtained from shifting the pure-tone rate-intensity functions by ΔI_{EH} . Note that only results from pure-tone stimulation are used for the prediction of the noise-signal responses.

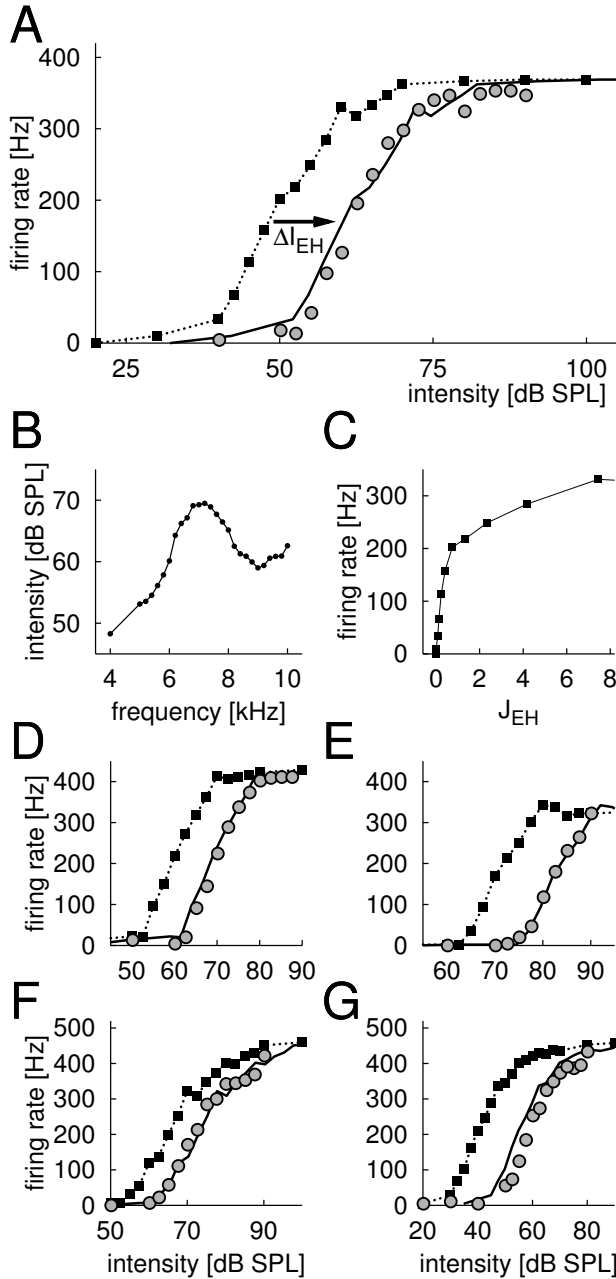


Figure 5.7: Comparison of predicted and measured rate-intensity functions. (A) Rate-intensity functions for pure tone (squares) and noise signal (circles). The prediction for the rate-intensity function of the noise signal (solid line) is obtained by shifting the pure-tone rate-intensity function according to the energy hypothesis, Eq. (5.11), as indicated by the arrow. In this example, the shift was $\Delta I_{EH} = 12.1$ dB, and the estimate of the true shift yielded $\Delta I_{true} = 12.6$ dB. (B) Determination of filter constants. The filled circles depict the measured intensities for pure tones between 4 and 10 kHz that led to a firing rate of 260 Hz in each case. These data were used to determine the filter constants C_n for the 4-kHz pure tone as well as for the range from 5 to 10 kHz. Further filter constants in this range were obtained by linear interpolation of this curve. (C) Response function $r(J_{EH})$ as determined by the rate-intensity function for the 4-kHz tone. The same firing rates that resulted in the squares in A were plotted against the effective sound intensity J_{EH} of the energy hypothesis. J_{EH} is given by $\frac{1}{2}A^2/C^2$, where A denotes the amplitude of the pure tone and C the filter constant as measured in B. While the pure-tone rate-intensity function displayed in A has a large nearly linear section from roughly 40 to 60 dB SPL, the response function $r(J_{EH})$ is clearly non-linear in the corresponding region (from $J_{EH} = 0.08$ to $J_{EH} = 8$) and resembles a square-root function. (D–G) Predicted and measured rate-intensity functions for the noise signal from four other cells. Symbols are used as in A. Note the different scales on the axes. Accordingly, the slopes of the rate-intensity functions differ considerably from cell to cell, but for a single cell, they are almost identical for pure-tone and noise stimulation. The values for ΔI_{EH} and ΔI_{true} in these four cases are: **D:** $\Delta I_{EH} = 9.0$ dB, $\Delta I_{true} = 9.8$ dB, **E:** $\Delta I_{EH} = 12.1$ dB, $\Delta I_{true} = 11.8$ dB, **F:** $\Delta I_{EH} = 7.8$ dB, $\Delta I_{true} = 6.6$ dB, **G:** $\Delta I_{EH} = 14.9$ dB, $\Delta I_{true} = 18.4$ dB. Figure adapted from (Gollisch et al., 2002) with permission.

In each case, the two measured rate-intensity functions are almost identical in shape as expected from the model. Furthermore, the measured noise-stimulus rate-intensity function and the shifted pure-tone rate-intensity function coincide closely in most cases. To assess the results quantitatively, we calculated the deviation of ΔI_{EH} from the actual distance between the rate-intensity functions, ΔI_{true} , in each case. From the measurements, ΔI_{true} was obtained as the average distance of the data points on one rate-intensity function, $r^{\text{pt}}(I)$ or $r^{\text{noise}}(I)$, from the other rate-intensity function. This distance was determined by how far the data points have to be shifted along the intensity axis to fall on the linear interpolation of the other rate-intensity function. Because the steepest parts of the rate-intensity functions are most sensitive to this intensity difference, only points between 10% and 90% of maximum firing were included in this calculation.

For the energy hypothesis, $\Delta I_{EH} - \Delta I_{\text{true}}$ had a mean of $-0.62 \text{ dB} \pm 0.68 \text{ dB}$ (standard error). The spread of these data (standard deviation of 2.16 dB) corresponds to the expected measurement accuracy, which can be estimated to be around 2 dB; the determination of C^{pt} , the collection of C_n , and the locations of both $r^{\text{pt}}(I)$ and $r^{\text{noise}}(I)$ all contribute independently with about 1 dB error range. The pressure hypothesis yields $\Delta I_{PH} - \Delta I_{\text{true}}$ with a mean of $0.43 \text{ dB} \pm 0.68 \text{ dB}$ (standard error) and is thus not ruled out by this experiment.

The results suggest that the description of spectral integration by the energy hypothesis, as derived from the two- and three-tone experiments, is also applicable to more complex stimuli. The model can be used for an accurate prediction of the location of the rate-intensity function after measuring the filter constants from pure-tone responses.

5.7 Discussion of the Model

We have seen that the response of locust auditory receptor cells to stationary sound stimuli is determined by an effective sound intensity J that can be calculated from the stimulus spectrum and the cell's sensitivity at different sound frequencies. Despite the strong nonlinearity induced by spike generation, we were able to draw this conclusion from observing the neuron's firing rate by focusing on iso-response sets of stimuli, which cause the same neural response. Together with a model framework for the auditory transduction chain, this allowed us to identify a quadratic input nonlinearity as part of a cascade model. Mathematically, the discovered model structure corresponds to an LNLN cascade. The signal components are first scaled by filter constants C_n (*L step*), subsequently squared (*N step*), then summed up (*L step*), and the sum is finally transformed (*N step*). As the first model step does not mix contributions from different signal components, the C_n could formally also be taken up in the third model step, thus yielding an NLN cascade. However, the filtering by the tympanum, with which the C_n factors are associated, should happen before the squaring, which is presumably induced by mechanosensory transduction. In Chapter 7, we will indeed see that the C_n arise from a distinct temporal filter as a first model step. The final nonlinear transformation can be derived from the measurement of a single rate-intensity function with arbitrary but fixed spectral content.

Combining the model framework with iso-response measurements provided the ground for quantitative investigations of different hypotheses about the stimulus attribute relevant for spectral integration. While the amplitude hypothesis could be clearly dis-

carded, the energy and pressure hypotheses were more similar in their predictions regarding spectral integration. Combined evidence from several statistical investigations was necessary to demonstrate that the pressure hypothesis failed in several single cases and that the energy hypothesis provided a far better description of the data. Furthermore, the results showed that average responses of an auditory receptor cell to complex stimuli can be well predicted once the cell-specific effective sound intensity J has been measured. The resulting quantitative correspondence between the stimulus spectrum and the firing rate differs from the predictions of an earlier heuristic approach (Lang, 2000).

Important for the model's simplicity is the fact that the mechanical coupling of the stimulus can be described by a linear process. This is consistent with previous studies, which have found no indications of dominant nonlinearities or active movement of the sensory cilia (cf. Eberl, 1999). Distortion-product otoacoustic emissions from locust ears indicate slight nonlinearities at the tympanic membrane; under stimulation with two pure tones, microphone recordings in the ear reveal additional spectral components as a result of the nonlinear interactions of the stimulus frequencies. However, these distortion-product frequencies are at most about 50 dB below the stimulating intensities (Kösse and Boyan, 1998a;b) and thus appear to be negligible for the neuron's coding properties. Many other auditory systems, on the other hand, are strongly affected by nonlinear mechanisms and active signal amplification leading to increased sensitivity and frequency resolution. This phenomenon is common in vertebrate ears (Fettiplace and Fuchs, 1999; Hudspeth et al., 2000), but has also been shown to exist in some insect auditory systems (Göpfert and Robert, 2001).

One may speculate that these nonlinear effects are additional features on top of the same underlying mechanosensory transduction process. The findings of structural and functional similarities between hair cells and the *Drosophila* sensory bristle as well as the discovery in *Drosophila* of homologs of human genes related to hearing and deafness support this view and suggest that many aspects of mechanosensory transduction among insects and vertebrates are conserved (Adam et al., 1998; Bermingham et al., 1999; Eberl, 1999; Walker et al., 2000; Fritzsche et al., 2000; Gillespie and Walker, 2001). The energy hypothesis might thus be extended to account for spectral integration in other mechanosensory systems as well – possibly after modifications that take the system-specific nonlinearities explicitly into account.

To test this hypothesis, spectral integration properties could be measured in other hearing systems. In the mammalian auditory system, response properties of hair cells and nerve fibers are complicated by mechanical nonlinearities induced by the cochlea and a more intricate signal pathway than is the case in insect auditory systems. Nevertheless, measurements of basilar-membrane vibrations indicate that, outside a region around the characteristic frequency, the stimulus coupling to mammalian auditory receptor cells occurs in an approximately linear fashion (Ruggero et al., 2000; Eguíluz et al., 2000). This suggests that a phenomenological study based on the same method as in the present investigation might also reveal interesting properties of the transduction process in hair cells.

Regarding the comparison with temporal-integration studies, our results go along well with the finding that energy detection describes firing thresholds for double-click and intensity-duration-trade-off experiments in receptor cells of moths (Tougaard, 1996;

Tougaard, 1998). In mammalian auditory nerve fibers, on the other hand, first-spike latencies correspond to the integrated pressure and not the energy (Heil and Neubauer, 2001). It is possible that this discrepancy is due to a fundamental difference in the transduction mechanisms of hair cells and insect auditory receptor cells. However, several simpler explanations are also available. First, the interpretation of the mathematical model of spike latencies given by Heil and Neubauer (2003) suggests that the origin of this temporal integration lies in the biophysics of synaptic transmission between the hair cells and the auditory-nerve fibers, and not in the transduction process itself. The long integration times and the large variability of spike timing (P. Heil, personal communication) support this idea.

Second, an interesting possibility to reconcile the two models of spectral energy integration and temporal pressure integration is based on the fact that latency measurements reflect features of the transduction as well as properties of additional dynamic processes, such as internal calcium dynamics and spike generation. In this context, it should be noted that the latency in type-I excitable membranes depends strongly and nonlinearly on the input strength (Hodgkin, 1948; Rinzel and Ermentrout, 1998; Izhikevich, 2000). This opens up the possibility that properties of the spike generator alter the effective input in such a way that energy integration is in accordance with the observed correspondence between latency and the temporal pressure integral.

In fact, Ermentrout (1996) showed that in type-I membranes, the firing rate r to a constant stimulus J above the firing threshold J^* approximately obeys the square-root relation $r(J) \sim \sqrt{J - J^*}$. For a simplified phase-integrator model (Hoppensteadt, 1997), the latency Δt is then given by the condition that the integral $\int_0^{\Delta t} dt \sqrt{J(t) - J^*}$ reaches a threshold value. According to the energy hypothesis, J is proportional to the square of the pressure amplitude A of a pure tone and in most cases large compared to J^* . This cancels the square root thus resulting in the latency condition $\int_0^{\Delta t} dt |A(t)| = \text{const}$, the dominant component of the model proposed by Heil and Neubauer. The above considerations may also explain the apparent discrepancy between the latency measurements and the fact that psycho-acoustic studies successfully apply energy-integration models (Garner, 1947; Plomp and Bouman, 1959; Zwislocki, 1965; Florentine et al., 1988). Further experiments that compare spectral and temporal integration in different systems may shed light on this question.

CHAPTER SUMMARY:

The activity of locust auditory receptor cells in response to stationary stimulation can be well described by average firing rates. The question about which property of the acoustic signal best corresponds to this activity led us to investigate the cells' spectral-integration properties. Three different hypotheses about how the auditory transduction chain combines separate spectral components of the sound were formulated in a cascade-model framework and led to predictions for the different ways in which two tones can be combined to yield the same firing rate. The experimental measurement of these iso-response sets revealed that only the hypotheses based on extracting the stimulus energy is consistent with the data. The resulting three-step model of sound transduction for stationary signals can be used to accurately predict firing-rate responses for noise-like signals.

CHAPTER 6

TEMPORAL INTEGRATION

Only seldom is the auditory system faced with encoding long, stationary stimuli such as in the previous chapter. The characteristic structures of acoustic signals typically comprise changes of sound intensity on different time scales. To encode such temporally modulated sounds, auditory receptor cells must be able to reliably track the signal fluctuations. Hence, a central feature of sound encoding in receptor cells is their high temporal resolution and accuracy. We therefore now turn to investigating the signal processing of short, temporally structured sound patterns.

Here, after having identified a suitable model framework for the processing of stationary sounds in the previous chapter, we aim at including the dynamic aspects of the auditory transduction chain into the model. This takes us to the question how the biophysical processes integrate the acoustic stimulus in time. The small time scales involved in transduction pose a particular experimental challenge. For characterizing the relevant processes nevertheless with high temporal resolution, we will apply the CIRS approach introduced in Chapter 4.¹

6.1 *Spike-Triggered-Ensemble Analysis*

Before applying iso-response methods, let us investigate what more traditional techniques of data analysis can tell us about temporal integration. A common investigation tool is *spike-triggered-ensemble analysis*. This can be viewed as an extension of the spike-triggered-average method, which was used in Chapter 2 to obtain a lower bound on the temporal resolution of the receptor neurons for amplitude-modulated stimuli. Here, we will go further and consider not only amplitude modulations, but variations of the whole air-pressure wave. Furthermore, we will analyze the spike-triggered average as well as the spike-triggered covariance.

Generally, spike-triggered-ensemble analysis is based on recording responses to random stimuli, usually resembling Gaussian white noise. From this set of random signals, those instances are picked out that led to a spike by the investigated neuron. The statistical features of this spike-triggered ensemble are subsequently analyzed to reveal, which stimulus aspects are correlated with the spiking activity. Such an analysis is often used

¹This chapter is in parts based on (Gollisch and Herz, 2004a).

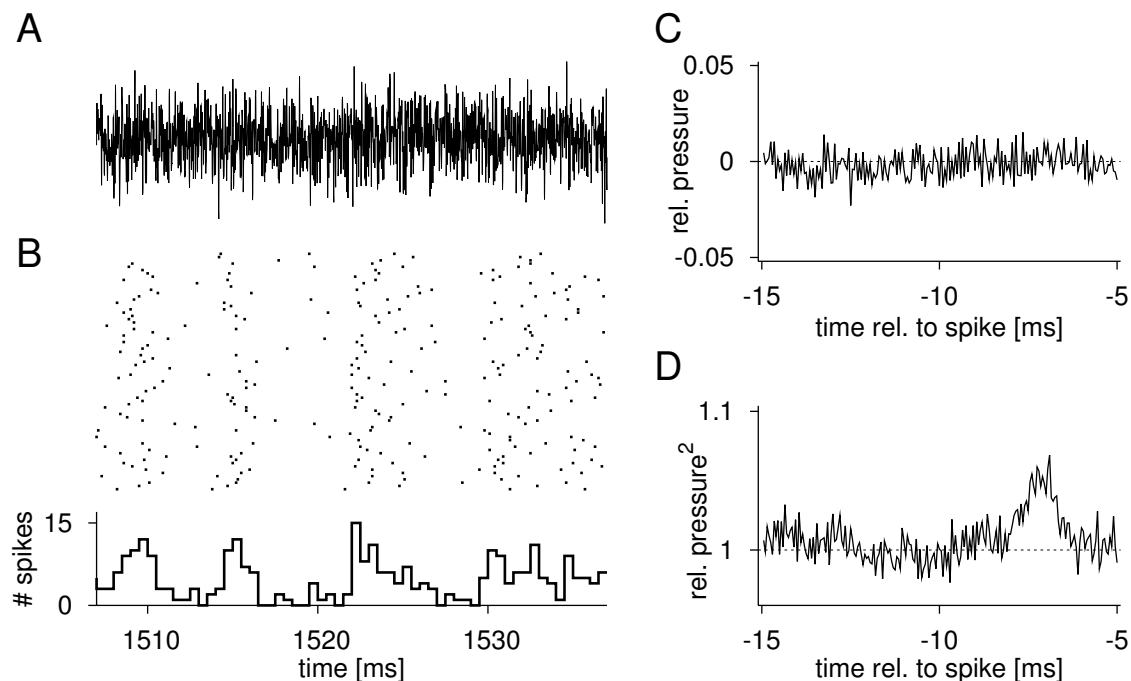


Figure 6.1: Spike-triggered-average analysis. (A) 30-ms excerpt of the stimulus. (B) Spike times from 73 stimulus repetitions corresponding to the stimulus part shown above as a raster plot and combined to a peri-stimulus time histogram, denoting the number of spikes per 0.5-ms bin. (C) Spike-triggered average obtained from averaging all stimulus segments preceding a spike. The first 0.4 s of the response were discarded. 30,327 spikes were included in the analysis, corresponding to an average firing rate of 115.4 Hz. (D) Spike-triggered average of the squared signal.

to determine receptive fields of sensory neurons. So far, systematic treatments have been developed for the average (Rieke et al., 1997; Chichilnisky, 2001) and the covariance (Bialek and de Ruyter van Steveninck, 1998; Schwartz et al., 2002; Touryan et al., 2002) of the spike-triggered ensemble. The spike-triggered average (STA) denotes the average stimulus that preceded a spike and can be interpreted as the linear filter in the first step of a Wiener system (Chichilnisky, 2001), cf. Chapter 3. The spike-triggered covariance (STC) can be used to analyze the structure of the spike-triggered ensemble in a way similar to the technique of Principal Component Analysis. The eigenvalues of the STC matrix are compared to those of the covariance matrix of the complete stimulus. The eigenvectors of the STC for which the eigenvalues show significant deviations indicate stimulus components that substantially influence the spike probability. These components can also be interpreted as the first step of a Wiener system containing multiple linear filters (Bialek and de Ruyter van Steveninck, 1998).

Figure 6.1 shows a spike-triggered-average analysis for a locust auditory receptor neuron. The stimulus was a random acoustic signal of four seconds duration with sound amplitudes drawn at a sampling rate of 20 kHz from a unit-variance Gaussian distribution (corresponding to a 10-kHz cut-off frequency). The amplitudes were cut off at ± 4 standard deviations. For the recording shown here, the stimulus was played at an intensity of 64 dB SPL. The responses in Fig. 6.1B reveal phases of higher and lower response probability, but the timing is apparently unreliable. Note that this is in contrast to

the higher temporal precision found in response to amplitude-modulated Gaussian noise (Fig. 2.6), which contained long excursion to high stimulus intensities more frequently than the present signal. The fast random fluctuations of this signal, which are necessary to probe the system on small time scales, thus result in a stimulus that drives the cell inefficiently for most of the time. This is a general problem of white-noise analysis; particular stimulus structures, to which the neuron may preferentially respond, occur only seldom in a random sequence. As a consequence, long recording times are necessary to acquire sufficient statistics.

The spike-triggered average in Fig. 6.1C shows no particular structure. When we first square each stimulus component and subsequently average over the spike-triggered ensemble, however, we find a peak near 7 ms before the spike (Fig. 6.1D). This tells us that spikes were correlated with large stimulus deflections to positive or negative values in a window of approximately 1.5 ms width around 7 ms before the spike. In the first calculation of the spike-triggered average, these positive as well as negative deflections apparently canceled each other out on average. Other stimulus parts outside the 1.5-ms temporal window seem to be of no importance to the spike so that this window can be interpreted as an upper bound of the extent of the temporal receptive field. The true window of temporal integration, however, may still be smaller; temporal jitter of the output can smear out its structure and lead to a broadening of the peak in the correlation analysis. Note further that the interpretation of the spike-triggered average in terms of a linear filter in a Wiener system as given, e.g., by Chichilnisky (2001) is only valid if the spike-triggered average is obtained from a random signal with radially symmetric distribution. This is true for the Gaussian distribution of the amplitudes, but not for the distribution of the squares. For such an interpretation, the experiment would have to be repeated with a stimulus whose squared amplitudes follow a Gaussian distribution, but the temporal resolution will still be limited by spike jitter.

Instead, let us turn to investigating the second order statistics of the spike-triggered ensemble. The spike-triggered covariance is calculated as

$$C(t_1, t_2) = \frac{1}{N} \sum_{n=1}^N A(t_1) \cdot A(t_2) - \delta_{t_1 t_2}, \quad (6.1)$$

where n enumerates all N stimulus segments preceding a spike, t_1 and t_2 denote the time points relative to the spike, and $\delta_{t_1 t_2}$ is the prior covariance of the applied stimulus. To be exact, the above formula is thus rather a difference of covariances. Note also that the spike-triggered average has not been subtracted from $A(t_1)$ and $A(t_2)$, as it was found to be approximately zero (Fig. 6.1C). Part of the matrix is shown in Fig. 6.2A. The covariance matrix was calculated for all time points between -15 ms and -5 ms before the spike. Because of the 10-kHz sampling rate, this corresponds to a 200×200 matrix. For clarity, only the lower right part of the matrix for time lags between -10 and -5 ms before the spike is shown. Here, a subtle oscillatory structure near the diagonal around 7 ms prior to the spike is visible.

To analyze, which components of the spike-triggered ensemble give rise to this structure, we performed an eigenvalue analysis. However, due to the finite number of spikes that goes into the analysis, noise in the matrix entries will lead to a distribution of eigenvalues around zero, which does not reflect significant structures of the spike-triggered

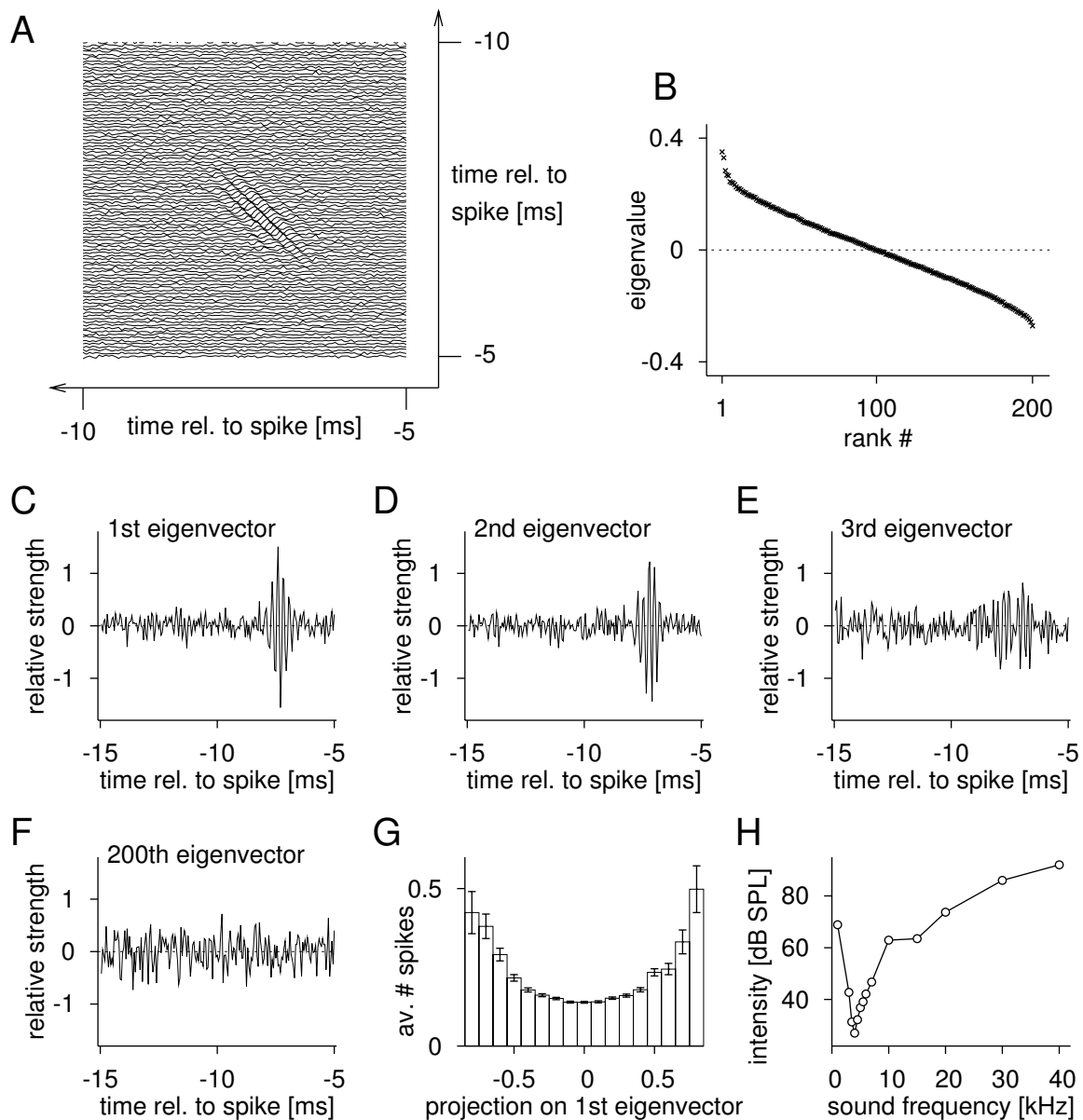


Figure 6.2: Spike-triggered-covariance analysis. (A) Spike-triggered covariance matrix. Each line shows the fluctuations of the matrix entries for one row of the matrix. Only one fourth of the matrix is shown; the complete matrix was calculated for time lags between -15 ms and -5 ms before the spike. (G) Eigenvalues of spike-triggered covariance matrix, rank-ordered. The two highest eigenvalues at the left hand side of the spectrum are raised slightly above the continuous distribution of the rest. (C–E) Eigenvectors corresponding to the three largest eigenvalues of the spike-triggered covariance matrix. (F) Eigenvector corresponding to the largest negative eigenvalue. (G) Average number of spikes as a function of the projection of the corresponding stimulus section onto the first eigenvector. (H) Characterization of the neuron's tuning properties by an independent measurement of the tuning curve. The data points denote intensities for pure tones of different sound frequencies required to evoke an average firing rate of 150 Hz.

ensemble. The eigenvalues are shown in rank order in Fig. 6.2B, and the continuous distribution of eigenvalues reflects this noise floor. However, the two highest eigenvalues at the left hand side are raised slightly above this level. The corresponding eigenvectors indeed display a pronounced structure with oscillatory contributions near 4 kHz (Fig. 6.2C and D). Note also that the envelopes of these two components are given by approximately the same 1.5-ms window as was found for the spike-triggered average of the squared signal. The third eigenvector indicates some smaller oscillations, suggesting that for even longer recordings, a third relevant component might be identifiable (Fig. 6.2E). All other eigenvectors display no evident structure. As an example, the eigenvector for the largest negative eigenvalue is shown in Fig. 6.2F.

For the first two eigenvectors, the positive eigenvalues indicate that these stimulus components lead to an increased spike probability. This can be verified by plotting the average spike number as a function of the projection of the corresponding stimulus segments onto the eigenvector. The projection is computed as the scalar product between the stimulus segments and the eigenvector. This is shown for the first eigenvector of the spike-triggered covariance matrix in Fig. 6.2G. For larger absolute values of the projection, more spikes were observed on average. The symmetry of the histogram for positive and negative values shows that the first eigenvector and its negative were equally effective in producing spikes. The histogram has a very similar shape for the second eigenvector as well. The 4-kHz frequency of the oscillations observed for both these eigenvectors coincide with the frequency of highest sensitivity of this neuron as measured by a standard tuning curve (Fig. 6.2H). A closer inspection of these two components of the spike-triggered ensemble show that they are phase shifted by about a quarter cycle. Given their otherwise nearly identical form, this is a consequence of the orthogonality of components obtained from an eigenvector analysis. Since the corresponding eigenvalues are nearly degenerate, any linear combination of the two components is also an eigenvector, which results in a two-dimensional eigenspace that is invariant to the stimulus phase. In other words, all oscillation phases are equally represented in the spike-triggered ensemble. The spike response within this two-dimensional eigenspace can be analyzed by viewing the average number of spikes as a function of the stimulus section's projection onto the first as well as the second eigenvector. This is shown in Fig. 6.3. The spike probability increases towards the margins of the plot, and the approximate spherical symmetry is in accordance with the phase invariance within this eigenspace. However, most stimulus sections fall into the center of the plot leading to poor statistics towards the margins, and several combinations of projections onto the first and second eigenvectors are not sufficiently represented.

In summary, we find that the spike-triggered stimulus ensemble preferentially contains sections with large contributions from the neuron's characteristic frequency regardless of the phase. The neuron thus responds best to the same sound frequency under noise stimulation as it does for pure tones. This result may be expected by intuition. Beyond the frequency preference, it is difficult to deduce information about the signal processing from the revealed components of the spike-triggered ensemble. For example, it is not clear how the vibration of the tympanum and the time constant of the neural membrane individually contribute to the shape of the determined relevant stimulus components. Furthermore, the true integration time is unclear. The relevant parts of the eigenvectors are contained in a 1.5-ms window. But here the same argument holds as for the peak of the average squared

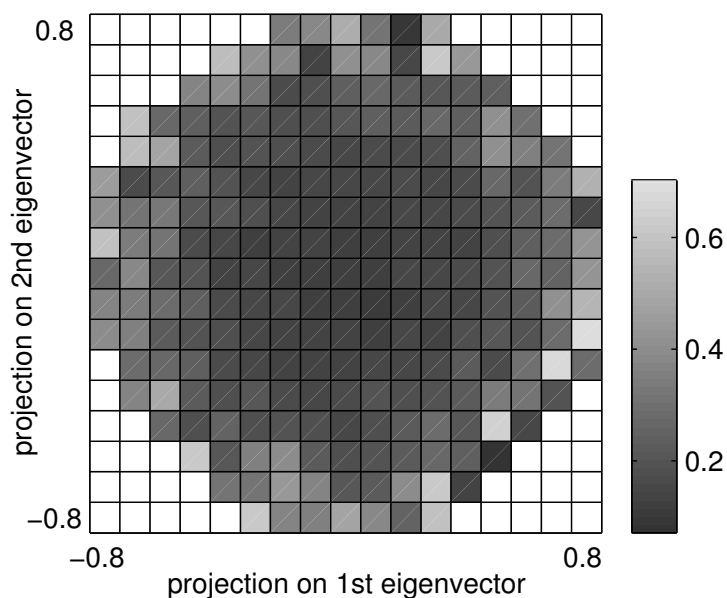


Figure 6.3: Joint dependence of spikes on two stimulus components. The gray scale depicts the average number of spikes as a function of the projections of the corresponding stimulus section onto the first and second eigenvectors of the covariance matrix. The data and the eigenvectors are the same as in Fig. 6.2. Bins with insufficient sampling, here less than 20 corresponding stimulus sections, were left white.

signal; its width is mostly determined by spike jitter. It is thus not clear how much of the oscillation is really integrated to produce a single response.

Although spike-triggered-ensemble analysis has been successfully applied to a number of neural systems, we see its limited applicability for auditory receptor cells. Two reasons seem to be largely responsible: 1) The approach does not separate different integration steps that may be part of the processing sequence. 2) Spike jitter smoothes out the temporal relation between the relevant structures within the segments of the spike-triggered ensemble and the spikes. In other words, we cannot deduce from a correlation analysis which stimulus part was actually responsible for a given spike if spikes occur sometimes 6 ms, sometimes 8 ms after their cause. To overcome these limitations, we will now investigate the receptor neurons with iso-response methods, which allow us to take the sequential nature of the transduction chain explicitly into account and focus on spike probabilities, not spike times.

6.2 IRS at Different Time Scales

We begin our analysis of the processing cascade by searching for input nonlinearities on different fixed time scales. To achieve high temporal resolution, we apply stimuli consisting of short sound-pressure pulses, called clicks. Combining the clicks in pairs of two with a fixed peak-to-peak interval Δt , we obtain a two-dimensional stimulus space that is parametrized by the peak amplitudes of the two clicks, A_1 and A_2 , respectively. Δt defines the time scale of investigation. Figure 6.4 shows illustrating examples of such stimuli with clicks that are $20\mu\text{s}$ long. Microphone recordings obtained at the site of the animal's ear are included. The measured air-pressure fluctuations indicate a slight broadening of the click width and some residual vibrations, but they nevertheless present a good approximation of the sharp original pulses, verifying that the loudspeakers reliably transmit such signals.

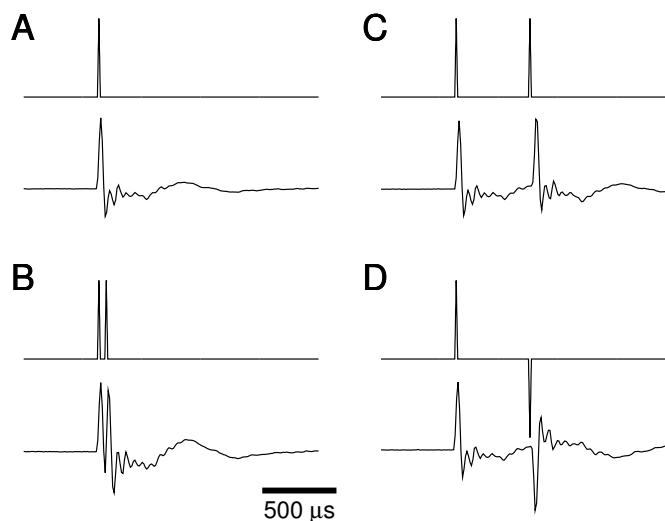


Figure 6.4: Examples of click stimuli. Each panel illustrates the computer-generated pulse signal that drives the loudspeaker (upper trace) and the resulting air-pressure fluctuations as measured with a high-precision microphone at the site of the animal’s ear (lower trace). The relative timing of the two traces in each panel is corrected for the approximately 1-ms absolute latency due to the propagation of the sound wave. The computer-generated clicks are triangular with a total width of $20\ \mu\text{s}$. For this measurement, all stimuli were presented at peak intensities of 90 dB SPL. The stimuli shown are (A) a single click, (B) a double click with a peak-to-peak interval $\Delta t = 50\ \mu\text{s}$, (C) a double click with $\Delta t = 500\ \mu\text{s}$, and (D) another double click with $\Delta t = 500\ \mu\text{s}$ whose second click points in the opposite (“negative”) direction. As the effectiveness in driving the loudspeaker is different for positive and negative clicks, the pressure values going into the amplifier were scaled by a factor of 0.83 for negative clicks. The scaling factor was determined so that the peak pressure of single clicks had the same absolute value as measured with the microphone for positive and negative clicks.

In response to these stimuli, the receptor cell fires at most one action potential per double click; stimulus intensity hardly influences spike timing, but strongly affects spike probability, as seen in Fig. 6.5. Responses may thus be described by the probability that a spike occurs within a certain time window, in the present case 3 to 10 ms after the first click. Here, we again find a dimensional reduction from the two-dimensional stimulus space to a one-dimensional output variable, which allows us to systematically search for iso-response sets.

For fixed time interval Δt , an iso-response set consists of those combinations of A_1 and A_2 that lead to the same predefined spike probability p . Since the spike probability increases with the click amplitudes, A_1 and A_2 can easily be tuned during the experiment to yield spike probabilities close to p . In the present case, this was achieved by presenting the click combination 2 to 15 times for a fixed intensity, beginning at 50 dB SPL and successively increasing or decreasing the intensity in steps of 5 dB depending on whether the measured spike probability was larger or smaller than p . Nine different values in steps of 1 dB around the obtained preliminary estimate of the required intensity were then repeated 30 to 40 times to achieve sufficient statistics. Finally, click amplitudes that matched the desired spike probability were obtained through interpolation. For fast and reliable data acquisition, we chose $p = 70\%$.

Figure 6.6B shows typical examples of such iso-response sets, measured for two dif-

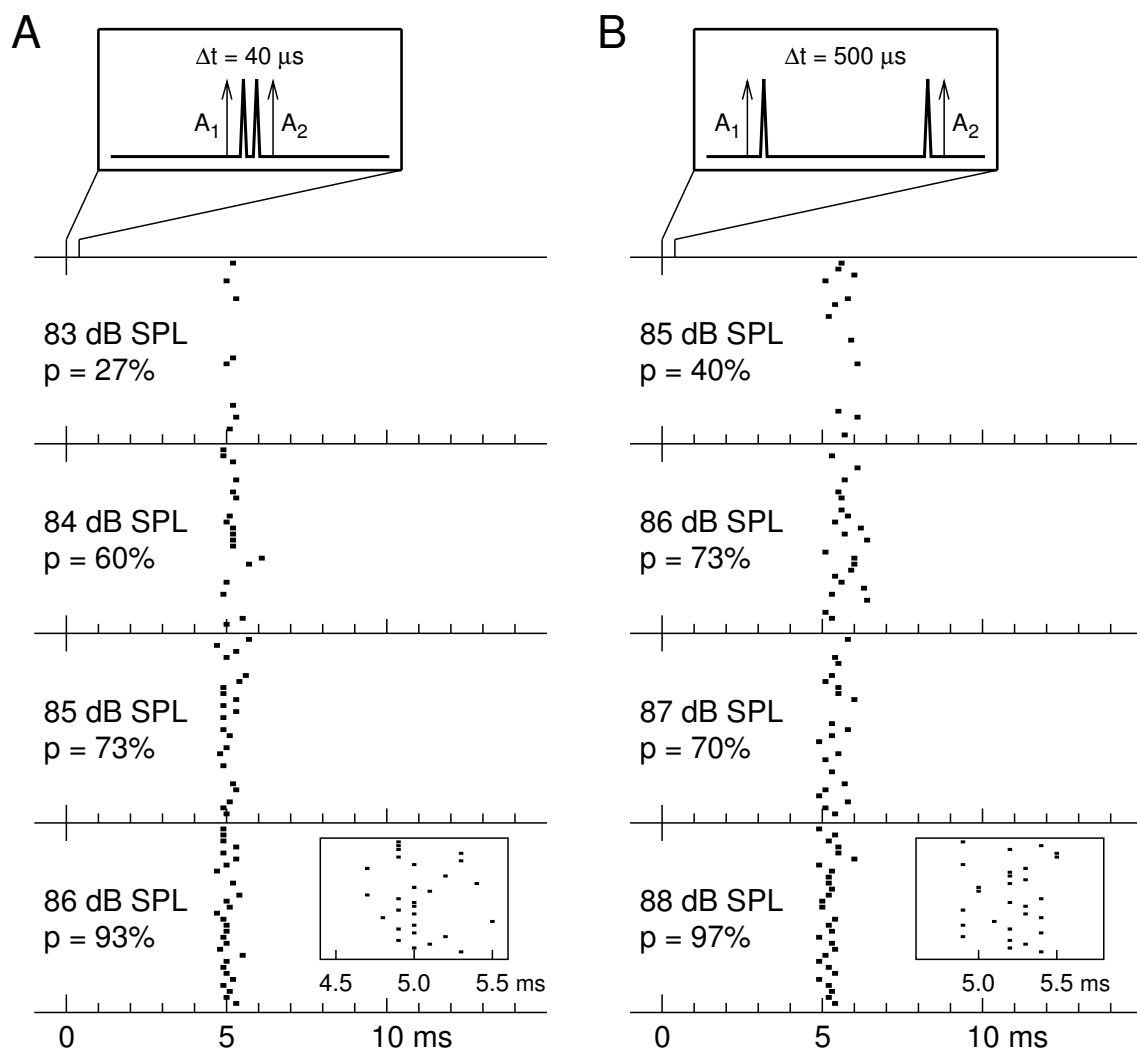


Figure 6.5: Raster plots of responses to two-click stimuli. Spike times were recorded for 30 presentations of two-click stimuli at different peak intensities for click intervals $\Delta t = 40 \mu\text{s}$ (**A**) and $\Delta t = 500 \mu\text{s}$ (**B**). For this data, the stimulus patterns were such that the click amplitudes A_1 and A_2 had a ratio of 1 : 1. The top row schematically displays the stimuli. The values of p denote the resulting spike probabilities in each case. Note that for the longer Δt , panel **B**, the intensity has to be approximately 2 dB higher than for the shorter Δt to reach the same spike probability. The inset displays spike times of the trials for the largest sound intensity for each Δt at higher magnification. All spikes fall in a temporal window of around 1 ms width. Spike times were measured with a temporal resolution of 0.1 ms. The responses in panel **B** have a slightly longer latency corresponding to the longer stimulus duration. Spike jitter appears to be slightly stronger for the longer inter-click interval. This may be caused by single spikes that occur in response to the first click alone. This effect is reduced when the first click is kept smaller than the second. Nevertheless, the data illustrate that the response of the receptor cell is well described by the occurrence probability of a single spike in a window between 3 and 10 ms after stimulus presentation. As often observed for these neurons, there is virtually no spontaneous activity.

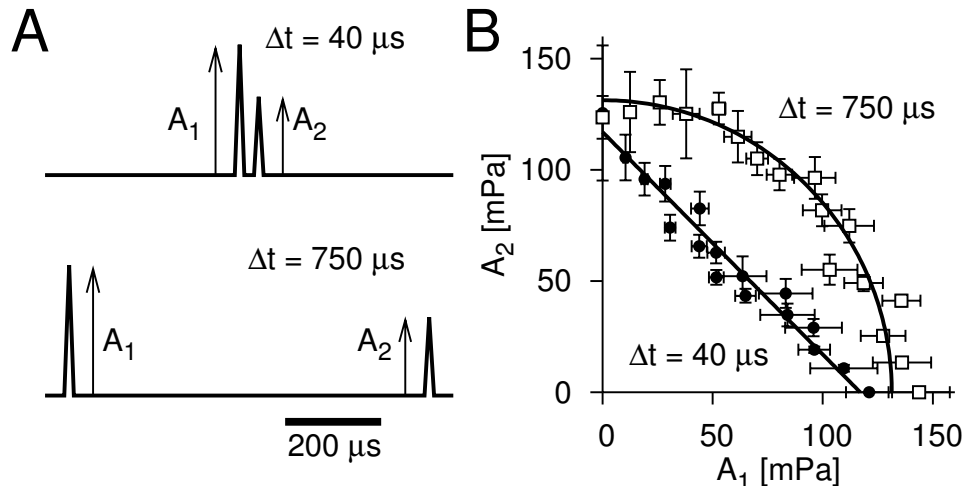


Figure 6.6: Iso-response sets for two-click stimuli. **(A)** Acoustic signals. The stimuli consisted of two short clicks with amplitudes A_1 and A_2 that were separated by a peak-to-peak interval Δt with $\Delta t = 40 \mu\text{s}$ (upper trace) or $\Delta t = 750 \mu\text{s}$ (lower trace). **(B)** Examples of iso-response sets from a single receptor cell. By adjusting the overall intensity for fixed ratios of A_1 and A_2 , stimulus combinations yielding spike probabilities of 70% were obtained (filled circles for $\Delta t = 40 \mu\text{s}$, open squares for $\Delta t = 750 \mu\text{s}$). All error measures display 95% confidence intervals. For the short interval, the data are well fitted by a straight line ($A_1 + A_2 = \text{const}$). For the long interval, a circle ($A_1^2 + A_2^2 = \text{const}$) yields a good fit (solid lines in both cases).

ferent time intervals Δt . The sets can be used to identify stimulus parameters that govern signal processing at the particular time scale. Most importantly, the iso-response sets exhibit specific shapes that vary systematically with Δt . For short intervals (below approximately $60 \mu\text{s}$), the sets lie on straight lines. For long intervals (between approximately 400 and $800 \mu\text{s}$, depending on the cell), the iso-response sets fall onto nearly circular curves. Presumably, these two shapes reflect two different processing steps in the auditory transduction chain.

A straight line implies that the linear sum, $A_1 + A_2$, of both click amplitudes determines the spike probability, as found for small Δt . This demonstrates that the sound pressure is the relevant stimulus parameter for short time scales. Knowing that the first step of the auditory transduction chain is the induced vibration of the ear drum, the linear summation on short time scales is not surprising; due to the tympanum's mechanical inertia, rapidly following stimuli are expected to superimpose. This interpretation is also in agreement with laser interferometer experiments, which have demonstrated that the tympanum reacts approximately linearly to the sound pressure (Schiolten et al., 1981).

For the longer intervals, on the other hand, the iso-response sets are circles, indicating that the quadratic sum, or $A_1^2 + A_2^2$, now determines the spike probability. It follows that the sound energy, which is proportional to the squared pressure, is the relevant stimulus parameter on this time scale. This means that besides the linear summation process visible on short time scales, there exists a second summation process, which is revealed on longer time scales. In between the two summation processes, the signal is squared.

A biophysical process that can mediate stimulus integration over longer intervals is the accumulation of electrical charge at the neural membrane. According to this explanation, the electrical potential induced by a click is proportional to the click's squared

amplitude, its energy; contributions from consecutive clicks are summed approximately linearly due to the passive membrane properties. This is in accordance with the investigations of Chapter 5 that have revealed an energy dependence of the receptor cells' firing rate for stationary sound signals. Furthermore, it has been shown that the DC component of the membrane potential in hair cells is proportional to sound energy (Dallos, 1985), suggesting that the energy-dependence may be a general feature of auditory transduction across species. The squaring of the transmitted signal between the mechanical resonator and the electrical integrator can be attributed to the core process of mechanosensory transduction, i.e., the gating of ion channels by the mechanical stimulus.

6.3 Cascade Model for Integrating Click Stimuli

The fact that we found two summation processes with an intermediate quadratic non-linearity immediately suggest a cascade model for the auditory transduction chain. The mathematical form of the model is derived as follows: The first sound click generates a tympanic vibration that is proportional to the click amplitude A_1 . Due to the subsequent quadratic nonlinearity, the resulting change of the membrane potential is proportional to A_1^2 . The second click will add to the tympanic vibration and to the membrane potential. We must remember, however, that some time Δt has passed since the first click so that the deflection of the tympanum as well as the membrane potential have changed in the meanwhile. Let us denote the time course of these changes by $L(\Delta t)$ for the tympanic vibration (linear in A_1) and by $Q(\Delta t)$ for the membrane potential (quadratic in A_1); accordingly, at time Δt , the deflection of the tympanum is $A_1 \cdot L(\Delta t)$, and the value of the membrane potential is $A_1^2 \cdot Q(\Delta t)$. When the second click arrives at time Δt , the deflection of the ear drum is augmented by A_2 , yielding $A_1 \cdot L(\Delta t) + A_2$. Due to the quadratic nonlinearity, the resulting contribution to the membrane potential is therefore $[A_1 \cdot L(\Delta t) + A_2]^2$. Adding this term to the membrane potential caused by the first click, we obtain an effective stimulus strength J :

$$J = A_1^2 \cdot Q(\Delta t) + [A_1 \cdot L(\Delta t) + A_2]^2. \quad (6.2)$$

Finally, the spike probability p is given as a function $p = g(J)$ of the effective stimulus strength.

We have thus obtained an LNLN cascade for pulse-like stimuli, as we see from a slightly more general description: The cascade is initiated when a new pulse comes in. It is added (*L step*) to all previous pulses, which receive “discount factors” (*filter constants*) $L(\Delta t)$ that depend on the time Δt since their occurrence (*temporal filter*). The resulting sum is then squared (*N step, static transformation*) and added (*L step*) to all previous squares, which themselves receive time-dependent “discount factors” $Q(\Delta t)$. At last, the result is transformed by the function $g(J)$ (*N step, static*). The investigations of the model's relation to more general cascade structures is postponed until the next chapter. First, let us investigate the functional form of the two filters $L(\Delta t)$ and $Q(\Delta t)$.

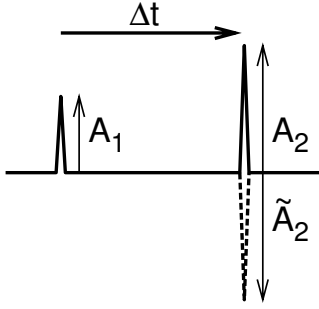


Figure 6.7: Stimuli for CIRS method. For measuring the temporal filters $L(\Delta t)$ and $Q(\Delta t)$, stimuli were applied that consisted of two clicks separated by a time interval Δt . The first click (amplitude A_1) was held constant throughout the experiment. The second click was presented in the same direction as the first click (solid line, amplitude A_2) or in the opposite (“negative”) direction (dashed line, amplitude \tilde{A}_2).

6.4 Temporal Characteristics of Stimulus Integration

Whereas the previous experiment showed that the separate effects of the two summation processes can be clearly discerned for short and long time intervals, their dynamics may largely overlap for intermediate Δt . Is it nevertheless possible to design an experiment that directly reveals the whole time course of the mechanical vibration $L(\Delta t)$ and the electrical integration $Q(\Delta t)$? This would provide a parameter-free description of both processes. To reach this goal, we again measure iso-response sets and quantitatively compare the stimuli with the CIRS method introduced in Section 4.2.

We thereby exploit that for fixed Δt , any pair of click amplitudes (B_1, B_2) should result in the same spike probability p as the pair (A_1, A_2) as soon as $J(A_1, A_2) = J(B_1, B_2)$. It is this straightforward relation that allows us to determine both $L(\Delta t)$ and $Q(\Delta t)$ independently of each other. To illustrate this, we now proceed with a particularly suitable choice of stimulus patterns, which keeps the mathematical requirements for the calculation at a minimum. For each Δt , we measure two different iso-response stimuli, one of which has a “negative” second click, i.e., a sound-pressure pulse pointing in the opposite direction as compared to the first click (Fig. 6.7). The amplitude of the first click, A_1 , is held fixed for both iso-response measurements.

Mathematically, this choice of stimulus patterns leads to two simple equations for the two unknowns $L(\Delta t)$ and $Q(\Delta t)$. Let us denote the absolute value of the amplitude for the second click by A_2 if presented in the same direction as the first click and by \tilde{A}_2 if presented in the opposite direction. Since we can assume that the spike probability p increases with the stimulus strength J , equal p implies equal J . The two pairs (A_1, A_2) and (A_1, \tilde{A}_2) therefore correspond to the same value of J . According to Eq. (6.2), the click amplitudes thus satisfy the two equations

$$J = A_1^2 \cdot Q(\Delta t) + [A_1 \cdot L(\Delta t) + A_2]^2, \quad (6.3)$$

$$J = A_1^2 \cdot Q(\Delta t) + [A_1 \cdot L(\Delta t) - \tilde{A}_2]^2. \quad (6.4)$$

Setting the two right sides equal to each other, we obtain

$$[A_1 \cdot L(\Delta t) + A_2]^2 = [A_1 \cdot L(\Delta t) - \tilde{A}_2]^2 \quad (6.5)$$

or

$$A_1 \cdot L(\Delta t) + A_2 = \pm \left(A_1 \cdot L(\Delta t) - \tilde{A}_2 \right). \quad (6.6)$$

The first solution of this mathematical equation, $\tilde{A}_2 = -A_2$, does not correspond to a physical situation as both A_2 and \tilde{A}_2 denote absolute values and are therefore positive. The remaining, second solution reads

$$A_1 \cdot L(\Delta t) + A_2 = -A_1 \cdot L(\Delta t) + \tilde{A}_2. \quad (6.7)$$

Solving for $L(\Delta t)$, we obtain

$$L(\Delta t) = \frac{\tilde{A}_2 - A_2}{2A_1}. \quad (6.8)$$

Substituting $L(\Delta t)$ from Eq. (6.8) in Eq. (6.3) or Eq. (6.4), we find

$$J = A_1^2 \cdot Q(\Delta t) + \left(\frac{\tilde{A}_2 + A_2}{2} \right)^2. \quad (6.9)$$

This yields

$$Q(\Delta t) - c = - \left(\frac{\tilde{A}_2 + A_2}{2A_1} \right)^2 \quad (6.10)$$

with $c = J/A_1^2$. Keeping A_1 and J constant throughout the experiment, $Q(\Delta t)$ is determined up to the constant c . We here leave this constant as a free parameter, which for plotting the data is estimated from the saturation level of $Q(\Delta t)$ as Δt becomes large. Alternatively, it could be inferred from an independent measurement with a single click: by setting $A_1 = 0$ in Eq. (6.2), we see that J corresponds to the square of the single-click amplitude that yields the desired spike probability, which lets us calculate $c = J/A_1^2$.

The above equations yield a direct and independent extraction of $L(\Delta t)$ and $Q(\Delta t)$ from two measurements with a specific inter-click interval Δt . By repeating such double measurements for different values of Δt , the whole time course of $L(\Delta t)$ and $Q(\Delta t)$ is obtained in a parameter-free fashion. Figure 6.8 shows examples of experimental results from three different cells. The “raw data” for the iso-response sets (Fig. 6.8A) show oscillations of the measured second-click amplitudes. The oscillations have an anti-phasic relation between positive clicks A_2 and negative clicks \tilde{A}_2 . This already reveals the oscillation of the tympanum. By quantitatively comparing the iso-response stimuli as derived above, the detailed shapes of $L(\Delta t)$ and $Q(\Delta t)$ were extracted as shown in Figs. 6.8B and C, respectively.

$L(\Delta t)$ displays strong oscillatory components. We interpret this as reflecting the tympanum’s oscillation at the attachment site of the receptor cell. The detailed temporal structure of $L(\Delta t)$ now allows us to investigate the salient features of this oscillation. To quantify our findings, we fitted a damped harmonic oscillation to the measured data for $L(\Delta t)$ and extracted the fundamental frequency as well as the decay-time constant. We can use these values to predict the neuron’s characteristic frequency (frequency of highest sensitivity) and the width of its frequency-tuning curve. For comparison, the tuning curves were measured with traditional methods by presenting pure tones at different fre-

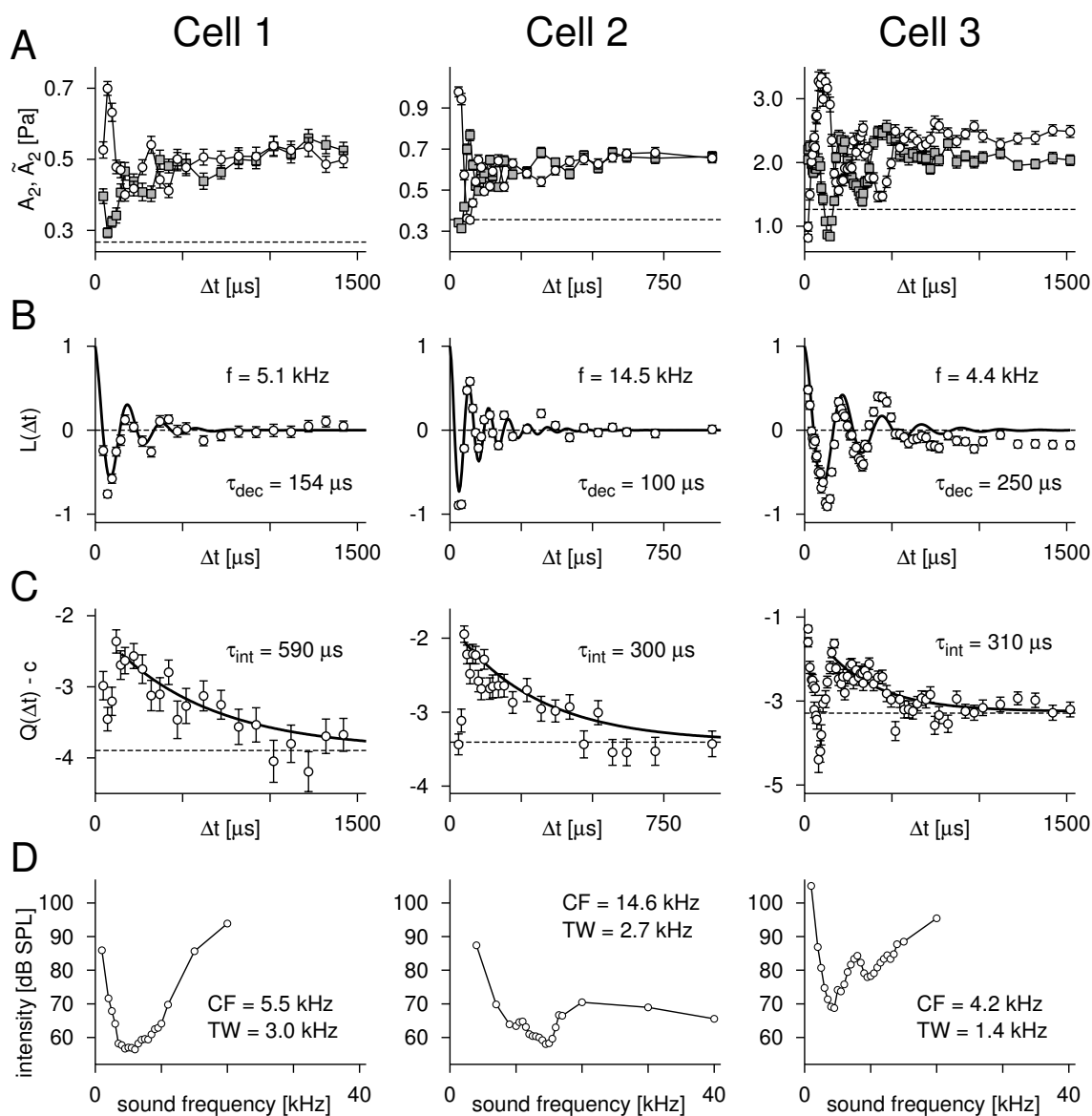


Figure 6.8: Measurements of temporal filters in the auditory transduction chain. The three columns for **A–D** show data from three exemplary recordings. (**A**) Iso-response sets. Shown are the amplitudes of the second click in the positive direction (A_2 , white circles) or negative direction (\tilde{A}_2 , gray squares) required for a spike probability of 70% for different inter-click intervals Δt . The first click was held fixed at a peak value A_1 indicated by the dashed line. (**B**) Time course of the filter $L(\Delta t)$ (white circles) calculated from the amplitudes of the measured iso-response stimuli. The data are compared to the response function of a damped harmonic oscillator (solid line) with fundamental frequency f and decay time constant τ_{dec} fitted to the data. (**C**) Time course of the filter $Q(\Delta t)$ (white circles). The data are compared to an exponential function (solid line) with an integration time constant τ_{int} fitted to the data. From the measurements, the values of $Q(\Delta t)$ were determined up to a constant $-c$, whose value can be determined from the exponential fit and is indicated by the dashed line. (**D**) Tuning curves depicting the intensity needed to evoke a firing rate of 150 Hz for stationary pure tones at different sound frequencies. The characteristic frequency (CF) and the tuning width (TW) are determined for comparison with the predictions obtained from the measured filter $L(\Delta t)$. Cell 1 and Cell 3 are low-frequency receptor cells, Cell 2 is a high-frequency receptor cell.

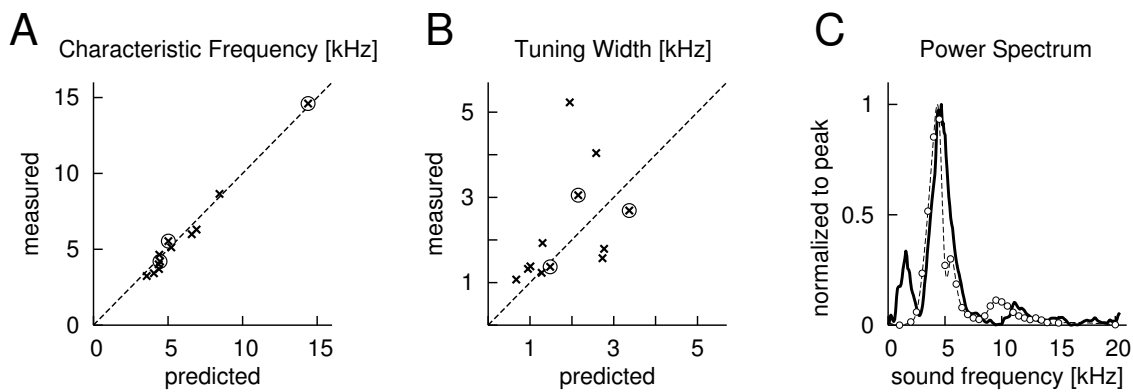


Figure 6.9: Prediction of tuning properties. Comparison of the predictions for the characteristic frequency (A) and the tuning width (B) as extracted from $L(\Delta t)$ with the corresponding values from the measured tuning curves. The encircled data points correspond to the three cells shown in Fig. 6.8. (C) Power spectra of a measured temporal filter $L(\Delta t)$ (solid line) and as obtained from the tuning curve (white circles; spline fit shown as a dashed line) of the same cell, both normalized to their peak values. The data for this panel is the same as for Cell 3 in Fig. 6.8.

quencies (Fig. 6.8D). The agreement between the predicted and the measured values of the characteristic frequency (Fig. 6.9A) and the tuning width (Fig. 6.9B) confirms that the new analysis faithfully extracts the relevant, cell-specific properties of the transduction sequence.

The data for Cell 3 resulted from an exceptionally long recording, which allowed 80 minutes of data collection for the iso-response measurements. The data is sufficiently dense to estimate the power spectrum of the transfer function $L(\Delta t)$ by a method called *Lomb periodogram* (Press et al., 1992), which is applicable to the present case of unevenly sampled data. Figure 6.9C shows the comparison of this power spectrum with the corresponding sensitivity curve obtained from the tuning curve in Fig. 6.8D. No assumptions about harmonic oscillation as in the comparison of characteristic frequency and tuning width are needed in this case. The location and the width of the primary peak near 5 kHz closely match, substantiating that the filter $L(\Delta t)$ determines the tuning properties of the receptor cell. Furthermore, a secondary small peak near 10 kHz is identified in both spectra with similar location and relative height. However, the power spectrum of $L(\Delta t)$ shows an additional prominent peak near 2 kHz, which is not present in the tuning curve. The origin of this low-frequency contribution is unclear. It is possible, though, that during this experiment, the coupling of positive and negative clicks was slightly different (cf. legend of Fig. 6.4 for normalizing positive and negative clicks), which is indicated by the offset between A_2 and \tilde{A}_2 in Fig. 6.8A. This might have caused an artifactual trend of the data for $L(\Delta t)$ resulting in additional power at low frequencies.

The measured $Q(\Delta t)$ displays an exponential decay suggesting that electrical charge accumulates at the neural membrane and decays over time due to a leak conductance. The decay time constants of $Q(\Delta t)$, which are extracted from exponential fits to the data, can thus be interpreted as membrane time constants. Previously, these could not be measured due to difficulties in obtaining reliable recordings from the somata or dendrites of the auditory receptor cells. We here find time constants in the range of 200 to 800 μ s. These

values are small compared to typical neural time constants around several milliseconds, reflect the high demand for temporal resolution in the auditory periphery, and explain the large maximum information rates of the investigated receptor neurons (Machens et al., 2001; Watzl et al., 2003). Similar small time constants are also suggested for mammalian auditory receptor cells (hair cells) by intracellularly measuring the low-pass properties for sinusoidal signals (Russell and Sellick, 1983; Geisler, 1998). The short initial rise phase of $Q(\Delta t)$ may result from the rapid build-up of the membrane potential after a click. For Cell 3 in Fig. 6.8, we seen a dip of $Q(\Delta t)$ to negative values after about 100 μs . This was seen in several examples, and its origin is unclear. It may, however, indicate additional dynamics of the transduction channels, such as an inactivation following the first click.

6.5 Test of Predictions for Three-Click Stimuli

Measuring the mechanical and electrical response dynamics, $L(\Delta t)$ and $Q(\Delta t)$, completes the model. It can now be used to predict responses to other types of stimuli and thereby test the general framework as well as the specific characteristics of $L(\Delta t)$ and $Q(\Delta t)$. As an example, let us consider three-click stimuli with amplitudes A_1 , A_2 , and A_3 and inter-click intervals Δt_1 and Δt_2 as depicted in Fig. 6.10A. Following the cascade model structure, the effective stimulus strength can be written as

$$\begin{aligned} J = & A_1^2 \cdot Q(\Delta t_1 + \Delta t_2) \\ & + [A_1 \cdot L(\Delta t_1) + A_2]^2 \cdot Q(\Delta t_2) \\ & + [A_1 \cdot L(\Delta t_1 + \Delta t_2) + A_2 \cdot L(\Delta t_2) + A_3]^2. \end{aligned} \quad (6.11)$$

This equation can be used to predict the values of A_3 needed to reach a predefined spike probability p , here again 70 %, for different combinations of A_1 , A_2 , Δt_1 , Δt_2 . This merely requires knowledge of those values for L , Q , and J that appear in the equation above. The values for the filters L and Q were obtained from two-click experiments as in the previous section, and J was measured as the squared amplitude of a single click that yields the predefined spike probability p . For comparison, A_3 was then measured by tuning the amplitude of the third click in the experiment until the spike probability p is reached. Figure 6.10B shows the correspondence of predicted and measured values for A_3 from one exemplary recording; the quantitative agreement between model and experiment shows that the cascade-model approach may be generalized to acoustic inputs with more than two clicks.

6.6 Discussion of the Experimental Approach

As we have seen, sound transduction in locust auditory receptor cells can be described by a nonlinear cascade model consisting of two linear filters and two nonlinear transformations. The identification of this cascade was possible by applying iso-response measurements. First, an intermediate nonlinear transformation was uncovered by measuring iso-response sets at different time scales; the two linear filters surrounding this nonlinearity were then characterized by a quantitative comparison of iso-response stimuli. The final

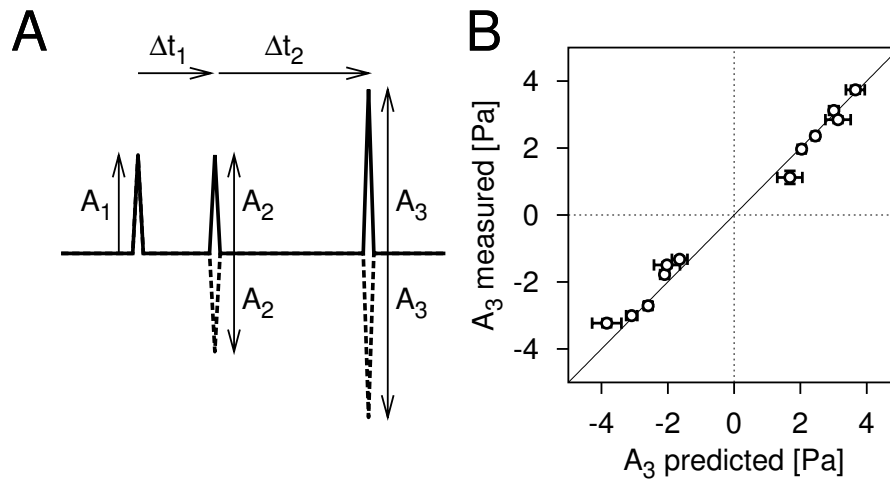


Figure 6.10: Model predictions for three-click stimuli. **(A)** Acoustic stimuli. The stimuli consisted of three clicks with amplitudes A_1 , A_2 , A_3 that were separated by time intervals Δt_1 and Δt_2 , respectively. The second and third click were either given in the same or opposite (“negative”) direction as the first click. The absolute values of A_1 and A_2 were set equal and held constant (here $|A_1| = |A_2| = 1.13$ Pa), and A_3 was adjusted to yield a spike probability of 70%. The pairs of time intervals $(\Delta t_1, \Delta t_2)$ used for this experiment were $(100\ \mu\text{s}, 100\ \mu\text{s})$, $(100\ \mu\text{s}, 200\ \mu\text{s})$, and $(200\ \mu\text{s}, 100\ \mu\text{s})$; all 4 combinations of possible directions for A_2 and A_3 were applied in each case. **(B)** Predicted and measured amplitudes of the third click. Predictions were made after $L(\Delta t)$ and $Q(\Delta t)$ had been measured with two-click experiments such as in Fig. 6.8. The comparison between predicted and measured values for A_3 therefore contains no free parameters. As shown by these data, the model allows quantitatively accurate predictions.

output nonlinearity was not explicitly measured, but could in principle be easily obtained by presenting stimuli that cover a range of effective sound intensities and by assessing the corresponding spike probability.

The method revealed new details of the integration processes with a resolution far below one millisecond. The results for the time course of the filter $L(\Delta t)$ for the mechanical oscillation agreed with traditional measurements of tuning curves and, moreover, explicitly showed the decay of the oscillation. The time constants of the electrical integration that could be extracted with the CIRS method had not been accessible by other means.

Besides its applicability under *in vivo* conditions, the presented approach has five advantageous properties: First, the method effectively decouples temporal sensitivity on the input side from temporal precision on the output side by focusing on spike probabilities. For example, we saw that spike latencies varied by about one millisecond within a single recording set due to cell-intrinsic noise (Fig. 6.5). Still we were able to probe the system with a resolution down to a few microseconds. This would not have been possible using classical techniques such as poststimulus time histograms, reverse correlation, and Wiener-series analysis. All these methods are intrinsically limited by the width of spike-time jitter and thus cannot capture the fine temporal details of rapid transduction processes. For our method, the resolution is only limited by the precision with which the sensory input can be applied.

Second, the method is robust against moderate levels of spontaneous output activity, as this affects all stimuli within one iso-response set in the same way. Methods that require measurements at different response levels, on the other hand, are likely to be sys-

tematically affected because the same internal noise level may have a different influence at different levels of output activity.

Third, the method can be used to investigate processing sequences that include multiple nonlinear steps. For the investigated system, both mechanosensory transduction and spike generation induce strong nonlinearities. Classical systems analysis (Marmarelis and Marmarelis, 1978; Korenberg and Hunter, 1986) is severely limited in this situation. The simultaneous analysis of individual steps makes it also possible to uncover possible correlations between parameter values of the different individual processes.

Forth, the method does not require that the time scales of the individual processes are well separated. For the studied receptor cells, mechanical damping was on average about 2.2 times faster than electrical integration, and even for cells with almost identical time constants, iso-response measurements led to high-quality data and reliable parameter fits.

Finally, in many input-output systems, the last stage of processing can be described by a monotonic nonlinearity. Here, this is the relation between the effective stimulus strength J and the spike probability p , which includes thresholding and saturation. By always comparing stimuli that yield the same output activity, the analysis is independent of the actual shape of $p(J)$. Preceding integration steps may thus be analyzed without any need to model $p(J)$. This feature is independent of the specific output measure and applies to spike probabilities, firing rates, or any other continuous output variable.

CHAPTER SUMMARY:

For understanding the remarkable signal-processing features of auditory systems, knowledge about the dynamics of stimulus integration by auditory receptor cells on short time scales is required. Here, we have seen that a nonlinear cascade can be identified that describes the response probability of locust auditory receptor neurons to short click stimuli. Application of iso-response measurements made it possible to characterize this cascade despite the involvement of two different nonlinear transformations. This led to an accurate assessment of the two integration processes involved in the transduction chain, the mechanical vibration of the tympanum and the accumulation of electrical charge. Both these processes were found to act on sub-millisecond time scales.

CHAPTER 7

GENERALIZED CASCADE MODEL

The results of the previous two chapters led to models that describe different features of the response properties observed in locust auditory receptor neurons. The model in Chapter 5 captures the behavior of the firing rate in response to stationary acoustic signals; the model in Chapter 6 relates single-spike probabilities to the amplitudes of short click stimuli. Both models are based on cascade systems with similar building blocks and a straight-forward biophysical interpretation. It is thus natural to ask if the models can be viewed as special cases of a single underlying framework. After all, the biophysical machinery of auditory transduction is the same whether under constant stimulation or for short clicks.

In this chapter, we set up a more general cascade model for the auditory transduction chain in locust auditory receptor neurons. Subsequently, we will investigate how the special model versions of Chapter 5 and 6 can be formally derived from the general model. These derivations manifest the relations between the different theoretical approaches and allow us to interpret their parameters within a common framework. Furthermore, explicitly stating the mathematical assumptions that are required for the derivation makes us aware of the limitations of the different model versions.

The formal derivations require only simple, straight-forward mathematical manipulations. Nevertheless, as they are targeted at forming rigorous connections between the model versions, Sections 7.2 and 7.3 have a somewhat technical taste to them. Readers with less interest in the formal aspects of the model and little mathematical inclination may skip these stand-alone sections without lacking background in the remainder of this study.

7.1 Generalization of the Model to Arbitrary Stimuli

The findings of the previous two chapters suggested that the following sequence of processing modules form the basis of the relation between sound input and spike response:

1. the linear filtering induced by the tympanum,
2. the nonlinear (quadratic) transformation of mechanosensory transduction,
3. the linear filtering by the low-pass properties of the neural membrane,
4. the nonlinear transformation induced by the spike-generation mechanism.

A general mathematical formalization of this signal-processing sequence is straightforward, given the building blocks introduced in Chapter 3. We denote the filter of the tympanum in the time domain by $l(\tau)$, so that after the first step, the movement of the tympanum $\xi(t)$ in response to a sound-pressure wave $A(t)$ is given by

$$\xi(t) = \int_0^{\infty} d\tau l(\tau) \cdot A(t - \tau). \quad (7.1)$$

Note that the causality of the filter $l(\tau)$ is taken explicitly into account by setting the lower limit of the integral to zero. The next step is the mechanosensory transduction, which is modeled as a static nonlinearity. Following the models of the previous two chapters, we directly take the nonlinearity to be a squaring operation. For the provoked transduction current $\psi(t)$, we thus find

$$\psi(t) = [\xi(t)]^2 = \left[\int_0^{\infty} d\tau l(\tau) \cdot A(t - \tau) \right]^2. \quad (7.2)$$

The accumulation of charge at the neural membrane is modeled by another linear filter $q(\tau)$. This yields the effective sound intensity $J(t)$,

$$J(t) = \int_0^{\infty} d\tau' q(\tau') \cdot \psi(t - \tau') = \int_0^{\infty} d\tau' q(\tau') \cdot \left[\int_0^{\infty} d\tau l(\tau) \cdot A(t - \tau - \tau') \right]^2. \quad (7.3)$$

Finally, the spike generation leads to the response $r(t)$ via another static nonlinearity $g(\cdot)$,

$$r(t) = g(J(t)) = g\left(\int_0^{\infty} d\tau' q(\tau') \cdot \left[\int_0^{\infty} d\tau l(\tau) \cdot A(t - \tau - \tau') \right]^2 \right). \quad (7.4)$$

The response $r(t)$ can be interpreted as the instantaneous firing rate; in other words, $r(t) \cdot dt$ is the probability of finding a spike in the small time window dt around time t .

The model structure is schematically depicted in Fig. 7.1. For completeness, let us remark that the filters $l(\tau)$ and $q(\tau)$ are the impulse-response functions of linear operators, i.e., they denote the responses to short, “delta-function-like” inputs into the linear sub-processes. To emphasize the dynamic aspect, they can also be viewed as *temporal transfer functions*, as they denote how strongly an input affects the sub-system’s response after τ .

Note that the model – despite its stochastic nature if $r(t)$ is interpreted as a spike probability – does not include explicit sources of spike jitter. Noise in the spike propagation velocity, e.g., is likely to distort the relation between the timing of the observed spike and the time t of its generation by $r(t)$.

The model also does not include refractoriness or adaptation. As these phenomena in general affect the responses of the receptor neurons (Benda et al., 2001; Schaette et al.,

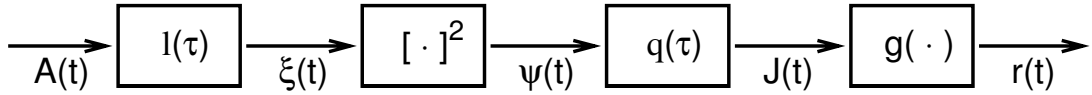


Figure 7.1: Structure of the LNLN cascade. The linear filter $l(\tau)$, $q(\tau)$ and the squaring nonlinearity as well as the nonlinearity $g(\cdot)$ successively transform the input signal $A(t)$ into the response signal $r(t)$.

2004), the direct application of this model is limited to the probability of the first spike in response to a stimulus: $r(t) \cdot dt$ then denotes the conditional spike probability given that no other spike occurred before t . More formally, $r(t)$ is the *hazard function* of spike occurrence (Gerstner and Kistler, 2002).

For the model’s application to firing rates, we will introduce additional assumptions about the cumulative effects of refractoriness and adaptation in the next section. In order to generalize the framework to arbitrary stimuli, however, additional modules need to be included. Appropriate concepts have recently been developed for adaptation (Benda and Herz, 2003) and refractoriness (Berry and Meister, 1998; Schaette et al., 2004). Combining these with the cascade model presented here should lead to a thorough description of the input-output relation for a large set of acoustic signals. Now let us turn to analyzing the relation of the cascade in Eq. (7.4) to the stationary and the click model versions.

7.2 Derivation of Stationary Model Version

The general model of Eq. (7.4) yields spike probabilities, from which we now intend to deduce firing rates. We must therefore capture the “average effects” of adaptation and refractoriness. For stationary stimuli, we can do so without invoking a complete model description of these two phenomena by the following central assumption: Refractoriness and adaptation occur in the processing sequence after the summation of transduction currents. In other words, we assume that $J(t)$ itself is not affected by the spiking activity and that instead the dependence of the spike probability on J , $p = g(J)$, is influenced.

Deferring the discussion about the validity of this assumption to the end of this section, we proceed by noting that $J(t)$ results from an input $A(t)$, which consists of a constant-intensity sound with frequencies in the kilohertz range. As the low-pass properties of the neural membrane smooth out such high-frequency components, the accumulated charge in response to stationary sound should be nearly constant. We therefore also assume that $J(t)$ can be approximated by a constant value J_0 .

Hence for constant-intensity stimuli, Eq. (7.3) yields the effective sound intensity J_0 that underlies the firing rate R . Assuming that for given J_0 the interactions between R , and the average levels of refractoriness and adaptation lead to a unique stable steady state, R depends on J_0 via some nonlinear transformation $\tilde{g}(\cdot)$, which will generally be different from the function $g(\cdot)$ in Eq. (7.4),

$$R = \tilde{g}(J_0). \quad (7.5)$$

Finally, J_0 can be calculated by noting that a constant value is equal to its temporal average,

$$J_0 = \langle J(t) \rangle = \lim_{T \rightarrow \infty} \frac{1}{2T} \int_{-T}^T dt J(t). \quad (7.6)$$

A shortcut for the calculation of J_0 based on spectral analysis is given in Appendix G. Here, we proceed by explicitly calculating $\langle J(t) \rangle$ for a stationary input signal $A(t)$, which can be written as a Fourier series:

$$A(t) = \sum_{n=1}^N A_n \sin(2\pi f_n t + \phi_n). \quad (7.7)$$

Using this as the input for the full model for $J(t)$, we find

$$\begin{aligned} \langle J(t) \rangle &= \lim_{T \rightarrow \infty} \frac{1}{2T} \int_{-T}^T dt \int_0^\infty d\tau' q(\tau') \cdot \left[\int_0^\infty d\tau l(\tau) \cdot A(t - \tau - \tau') \right]^2 \\ &= \sum_{m=1}^N A_m A_n \int_0^\infty d\tau' q(\tau') \int_0^\infty d\tau_1 l(\tau_1) \int_0^\infty d\tau_2 l(\tau_2) \cdot M_{mn}(\tau', \tau_1, \tau_2) \end{aligned} \quad (7.8)$$

with the coupling matrix

$$\begin{aligned} M_{mn}(\tau', \tau_1, \tau_2) &= \lim_{T \rightarrow \infty} \frac{1}{2T} \int_{-T}^T dt \sin(2\pi f_m(t - \tau' - \tau_1) + \phi_m) \\ &\quad \times \sin(2\pi f_n(t - \tau' - \tau_2) + \phi_n). \end{aligned} \quad (7.9)$$

Due to the orthogonality properties of the sine-function, only the diagonal elements ($m = n$) of M give non-zero contributions. The integral thus yields

$$\begin{aligned} M_{mn}(\tau', \tau_1, \tau_2) &= \delta_{mn} \cdot \cos(2\pi f_n(\tau_1 - \tau_2)) \cdot \lim_{T \rightarrow \infty} \frac{1}{2T} \int_{-T}^T dt \left[\sin(2\pi f_n(t - \tau' - \tau_1) + \phi_n) \right]^2 \\ &= \delta_{mn} \cdot \frac{1}{2} \cdot \cos(2\pi f_n(\tau_1 - \tau_2)). \end{aligned} \quad (7.10)$$

Substituting this expression into Eq. (7.8), one summation can be performed directly by use of the Kronecker-delta, δ_{mn} , which leads to

$$\langle J(t) \rangle = \frac{1}{2} \sum_{n=1}^N A_n^2 \int_0^\infty d\tau' q(\tau') \cdot C_n^{-2} \quad (7.11)$$

with

$$\begin{aligned} C_n^{-2} &= \int_0^\infty d\tau_1 \int_0^\infty d\tau_2 l(\tau_1) \cdot l(\tau_2) \cdot \cos(2\pi f_n(\tau_1 - \tau_2)) \\ &= \left[\int_0^\infty d\tau l(\tau) \cos(2\pi f_n \tau) \right]^2 + \left[\int_0^\infty d\tau l(\tau) \sin(2\pi f_n \tau) \right]^2 \\ &= \|\hat{l}(f_n)\|^2 \end{aligned} \quad (7.12)$$

where $\hat{l}(f)$ is the Fourier transform of $l(\tau)$,

$$\hat{l}(f) = \int_0^{\infty} d\tau l(\tau) \cdot \exp(-2\pi i f \tau). \quad (7.13)$$

The term $\int_0^{\infty} d\tau' q(\tau')$ only yields a constant factor that can be absorbed by redefining the nonlinear function $\tilde{g}(\cdot)$. We thus find

$$R = \tilde{g}(J) \quad \text{and} \quad J = \frac{1}{2} \sum_{n=1}^N \frac{A_n^2}{C_n^2}, \quad (7.14)$$

exactly as in the energy model for stationary stimuli, Eqs. (5.5) and (5.7).

Note that according to the above derivation, the filter constants C_n of the stationary model have their origin in the Fourier components of the filter $l(\tau)$ and thus reflect the frequency tuning as induced by the tympanum. This had already been the intuition in Chapter 5, but has been manifested here mathematically. The exact shape of the filter $q(\tau)$, on the other hand, has no influence on the spectral-integration properties as long as it induces the low-pass filtering that leads to a constant $J(t)$. Finally, the firing-rate model also has a static output nonlinearity, $\tilde{g}(\cdot)$, at the end, but the exact shape of this nonlinearity may be substantially different from that of the full model, $g(\cdot)$, mainly due to the influence of refractoriness and adaptation.

The derivation relies on the assumptions that 1) adaptation and refractoriness effect the processing sequence of the auditory transduction chain only in the last step, the conversion of the effective sound intensity J into the spike probability, 2) the signals are low-passed filtered so that $J(t)$ is constant under stationary stimulus conditions, and 3) only one stable stationary state exists. The first assumption is justified by the fact that generic models of refractoriness and adaptation have been successfully applied to locust auditory receptor neurons (Schaette et al., 2004; Benda, 2002), which fulfill this criterion. Both phenomena are triggered by the spiking activity in these models; refractoriness then modifies the resulting spike probability multiplicatively, whereas adaptation leads to a subtractive current contribution in the relation between the transduction current and the spike probability. For completeness, let us add that a putative input-driven adaptation component, as hypothesized in Chapter 5 and to be revisited in the chapter to come, is not expected to affect the derivation presented here; as will be discussed in more detail later, it acts by changing the input filter $l(\tau)$ slowly over time so that under stationary conditions, $l(\tau)$ is fixed, albeit possibly different than at stimulus onset.

The second assumption is well fulfilled for typical sound frequencies in the kilohertz range where the grasshopper receptor cells are sensitive because the neural membrane low-pass-filters any remaining fluctuations in this range. As discussed in the derivation of the model in Chapter 5, this is supported by the absence of peaks at the stimulating sound frequency in the spectrum of the membrane potential (Hill, 1983) as well as by the absence of phase locking (Suga, 1960; see also Section 2.4).

Finally, the uniqueness of the stable steady state for a given J_0 is explained by the fact that the firing rate R and the stationary effects of refractoriness and adaptation form a simple negative feedback loop that does not lead to multistability.

7.3 Derivation of Click Model Version

In order to connect the general model to the click model version of Chapter 6, we need to investigate the responses to pairs of short, pulse-like inputs. These are mathematically modeled as Dirac delta functions at time $t_1 = 0$ and at time $t_2 = \Delta t > 0$ with amplitudes A_1 and A_2 , respectively:

$$A(t) = A_1 \cdot \delta(t) + A_2 \cdot \delta(t - \Delta t). \quad (7.15)$$

The resulting effective sound intensity $J(t)$ is a function of time, but we are interested in the total (integrated) probability that a spike occurs. We can expect that the form of $J(t)$ to click inputs is stereotypical and sharply peaked, and that the height of this peak is a good measure for the total spike probability. Therefore we assume that the spike probability for click stimuli is approximately given as a function of the effective sound intensity a fixed time T after the second click, i.e.,

$$p = \tilde{g}(J(\Delta t + T)). \quad (7.16)$$

Note again that $\tilde{g}(\cdot)$ is not the same function as $g(\cdot)$ in Eq. (7.4), but effectively includes the integration of the spike probability density over time.

Substituting the expression (7.15) into Eq. (7.3), we can solve the inner integral directly because of the delta functions and thus obtain

$$\begin{aligned} J(\Delta t + T) &= \int_0^\infty d\tau' q(\tau') \cdot \left[\int_0^\infty d\tau l(\tau) \cdot \left(A_1 \cdot \delta(\Delta t + T - \tau - \tau') \right. \right. \\ &\quad \left. \left. + A_2 \cdot \delta(\Delta t + T - \tau - \tau' - \Delta t) \right) \right]^2 \\ &= \int_0^\infty d\tau \left[A_1 \cdot l(\Delta t + T - \tau) + A_2 \cdot l(T - \tau) \right]^2 \cdot q(\tau) \\ &= \int_T^{\Delta t + T} d\tau A_1^2 \cdot [l(\Delta t + T - \tau)]^2 \cdot q(\tau) \\ &\quad + \int_0^T d\tau \left[A_1 \cdot l(\Delta t + T - \tau) + A_2 \cdot l(T - \tau) \right]^2 \cdot q(\tau) \\ &= \int_0^{\Delta t} d\tau A_1^2 \cdot [l(\tau)]^2 \cdot q(\Delta t + T - \tau) \\ &\quad + \int_0^T d\tau \left[A_1 \cdot l(\Delta t + \tau) + A_2 \cdot l(\tau) \right]^2 \cdot q(T - \tau) \end{aligned} \quad (7.17)$$

The last two steps were obtained by splitting up the integral together with applying the causality conditions and by variable transformations. In order to solve these integrals, we need expressions for “successive transfer”, i.e., we need to understand how $l(\tau_1 + \tau_2)$ and $q(\tau_1 + \tau_2)$ are composed of transfer functions that depend only on τ_1 or τ_2 . To do so, we resort to the findings of the previous chapter and assume specific functional forms of $l(\tau)$ and $q(\tau)$. We approximate $l(\tau)$ as a damped harmonic oscillator with natural frequency ω and decay constant λ , whereas $q(\tau)$ is modeled as a leaky integrator with a decay constant

δ , i.e., for $\tau > 0$,

$$l(\tau) = \sin(\omega\tau)e^{-\lambda\tau}, \quad (7.18)$$

$$q(\tau) = e^{-\delta\tau}. \quad (7.19)$$

This yields

$$\begin{aligned} q(\tau_1 + \tau_2) &= e^{-\delta\tau_1} \cdot e^{-\delta\tau_2} \\ &= q(\tau_1) \cdot q(\tau_2), \end{aligned} \quad (7.20)$$

$$\begin{aligned} l(\tau_1 + \tau_2) &= \sin[\omega(\tau_1 + \tau_2)]e^{-\lambda(\tau_1 + \tau_2)} \\ &= \sin(\omega\tau_1)e^{-\lambda\tau_1} \cdot \cos(\omega\tau_2)e^{-\lambda\tau_2} + \sin(\omega\tau_2)e^{-\lambda\tau_2} \cdot \cos(\omega\tau_1)e^{-\lambda\tau_1} \\ &= l(\tau_1) \cdot \tilde{l}(\tau_2) + l(\tau_2) \cdot \tilde{l}(\tau_1), \end{aligned} \quad (7.21)$$

where $\tilde{l}(\tau) = \cos(\omega\tau)e^{-\lambda\tau}$ denotes a phase-shifted oscillator. Applying these relations to Eq. (7.17), we find

$$\begin{aligned} J(\Delta t + T) &= \int_0^{\Delta t} d\tau A_1^2 \cdot [l(\tau)]^2 \cdot q(\Delta t) \cdot q(T - \tau) \\ &\quad + \int_0^T d\tau \left[A_1 \cdot l(\Delta t) \cdot \tilde{l}(\tau) + A_1 \cdot l(\tau) \cdot \tilde{l}(\Delta t) + A_2 \cdot l(\tau) \right]^2 \cdot q(T - \tau) \\ &= A_1^2 \cdot q(\Delta t) \cdot \int_0^{\Delta t} d\tau [l(\tau)]^2 \cdot q(T - \tau) \\ &\quad + [A_1 \cdot \tilde{l}(\Delta t) + A_2]^2 \cdot \int_0^T d\tau [l(\tau)]^2 \cdot q(T - \tau) \\ &\quad + A_1^2 \cdot l^2(\Delta t) \cdot \int_0^T d\tau [\tilde{l}(\tau)]^2 \cdot q(T - \tau) \\ &\quad + 2 \cdot A_1 \cdot l(\Delta t) \cdot [A_1 \cdot \tilde{l}(\Delta t) + A_2] \cdot \int_0^T d\tau \tilde{l}(\tau) \cdot l(\tau) \cdot q(T - \tau) \end{aligned} \quad (7.22)$$

The last term contains an integral over a product of a sine (from $l(t)$) and a cosine (from $\tilde{l}(t)$) and will thus be small compared to the other integrals. We therefore neglect this term. Furthermore, we assume that the second integral is approximately equal to the third, as the phases of $l(t)$ and $\tilde{l}(t)$ do not significantly contribute in the integrals. We thus substitute $l(t)$ for $\tilde{l}(t)$ in the third integral. These two approximations both rely on the assumption that the oscillation period of $l(\tau)$ is short enough, i.e., ω is large enough, to result in significant averaging of the l -terms in the integral. Using the definitions

$$k = \int_0^T d\tau [l(\tau)]^2 \cdot q(T - \tau), \quad (7.23)$$

$$\gamma(\Delta t) = \frac{1}{k} \cdot \int_0^{\Delta t} d\tau [l(\tau)]^2 \cdot q(T - \tau), \quad (7.24)$$

Eq. (7.22) can be written as

$$\begin{aligned} J(\Delta t + T) &= A_1^2 \cdot q(\Delta t) \cdot \gamma(\Delta t) \cdot k + [A_1 \cdot \tilde{l}(\Delta t) + A_2]^2 \cdot k + A_1^2 \cdot [l(\Delta t)]^2 \cdot k \\ &= A_1^2 \cdot \{q(\Delta t) \cdot \gamma(\Delta t) + [l(\Delta t)]^2\} \cdot k + [A_1 \cdot \tilde{l}(\Delta t) + A_2]^2 \cdot k. \end{aligned} \quad (7.25)$$

Absorbing the constant factor k in the function $\tilde{g}(J)$, we obtain the same functional dependence of J on A_1 and A_2 as in the click model, Eq. (6.2). By comparison, we find

$$L(\Delta t) = \tilde{l}(\Delta t), \quad (7.26)$$

$$Q(\Delta t) = q(\Delta t) \cdot \gamma(\Delta t) + [l(\Delta t)]^2. \quad (7.27)$$

$L(\Delta t)$ is thus a phase-shifted version of the tympanum's response function $l(\Delta t)$, but retains the important resonance characteristics such as natural frequency and decay constant. In fact, as the oscillation of $l(\Delta t)$ is found to be faster than its decay ($\omega = 2\pi f > \lambda = 1/\tau_{\text{dec}}$, cf. Fig. 6.8), $\tilde{l}(\Delta t)$ is approximately proportional to the derivative of $l(\Delta t)$. Hence, $L(\Delta t)$ measures the velocity of the tympanic vibration. Note that this interpretation is consistent with the initial jump of $L(\Delta t)$ at $t = 0$, which is not expected for the displacement of an impulse-driven oscillator, but for its velocity.

$Q(\Delta t)$ captures the response function of electrical integration given by $q(\Delta t)$ up to small corrections. The $[l(\Delta t)]^2$ -term is quadratic and thus negligible for large enough Δt , as $l(\Delta t)$ quickly goes to zero. For small Δt , though, this term may lead to an oscillatory contribution to $Q(\Delta t)$, but this putative effect has so far been below our measurement accuracy. The factor $\gamma(\Delta t)$ approaches unity also due to the fast decay of $[l(\Delta t)]^2$, which yields the integrals in the numerator and denominator of Eq. (7.24) equal for large enough Δt . For this range (from the time scale of $L(\Delta t)$ measured in Chapter 6, this corresponds to $\Delta t \gtrsim 100$ or $200 \mu\text{s}$), we find $Q(\Delta t) \approx q(\Delta t)$. For small Δt , on the other hand, the factor $\gamma(\Delta t)$ suppresses the contribution from $q(\Delta t)$ leading to an initial rising phase of $Q(\Delta t)$ in contrast to the sharp onset of $q(\Delta t)$. This effect is seen in the data (Fig. 6.8) as well as expected from the notion that, for short Δt , the inter-click interval is too short to allow for a transduction current induced by the first click alone.

The above derivation mainly rests on two assumptions: 1) that the spike probability is mainly determined by the effective sound intensity $J(t)$ at a single point in time, 2) that the explicit formulas of “successive transfer”, Eqs. (7.20) and (7.21), apply to $l(\tau)$ and $q(\tau)$. The first assumption is motivated by the expected sharp deflections of the transduction currents in response to click stimuli. It is supported by the strong temporal localization of spike occurrence around a fixed time after the second click, see Fig. 6.5. However, the distribution of spike times may be slightly wider for larger inter-click intervals. A future systematic investigation of this effect, connecting it to the width of the expected peak in $J(t)$, may further advance the understanding of the model.

The second assumption rests on the experimentally extracted forms of $L(\Delta t)$ and $Q(\Delta t)$. The derivation is thus not entirely deductive, but instead leads to a self-consistent interpretation of the relations between l , q , L , and Q . The derivation explicitly uses the oscillator characteristics of $l(\tau)$ and the leaky-integrator properties of $q(\tau)$. For different characteristics of these filters, the relations between l , q , L , and Q may be different. This would not preclude their experimental examination based on the same approach with click

stimuli, but it may alter the interpretation of the extracted filters with respect to a general cascade model.

Further minor assumptions were used in the derivation in order to simplify the integrals in Eq. (7.22). These assumptions rest on the fact that the oscillation period of $l(\tau)$ is shorter than the decay time constants of $l(\tau)$ and $q(\tau)$ so that the integrals involve averaging over the phases of $l(\tau)$. This is consistent with the data, as the measurement of $L(\tau)$ generally reveals more than one full cycle of the oscillation.

CHAPTER SUMMARY:

Two models for the auditory transduction chain in receptor cells of locusts had been obtained under particular stimulus conditions, stationary and pulse-like stimulation. In this chapter, we showed that these two model versions can be deduced from a general model based on an LNLN cascade. The assumptions on which the specialized model versions rest were made explicit. The derivations showed that the two specialized versions are consistent with each other and led to mathematical relations between the parameters of the individual models. The generalized model can be further enhanced by including additional functional modules, which capture refractoriness and adaptation phenomena.

CHAPTER 8

SEPARATING ADAPTATION SOURCES

Many spiking neurons adapt to long-lasting stimulation; the firing rate decreases over time, even though the stimulus stays constant. Often, the activity levels off to a steady state after a certain period, which may range from tens of milliseconds to several seconds. The time scales of spike-frequency adaptation are thus considerably longer than the ones we found for the integration processes in the auditory transduction chain. The separation of time scales allows us to analyze adaptation processes independently of the details of the primary transduction chain.

Here, we return to a question already raised in Chapter 5: Can we distinguish between different functional sources that contribute to spike-frequency adaptation? More precisely, we will investigate the possible interfaces of spike-frequency adaptation within the auditory transduction chain. In Chapter 5, we argued that the primary sources of adaptation are triggered by the neuron's own spiking activity (*output-driven adaptation*) and thus lead to a global rescaling of sensitivity, which is the same for all frequency components. However, slight differences in the spectral-integration characteristics at stimulus onset and during the steady state raised questions about the existence of an additional adaptation component that depends directly on the sensory input, i.e., its sound intensity and frequency (*input-driven adaptation*). In this chapter, we will investigate this aspect further by applying the DIRS method introduced in Section 4.3.¹

8.1 *Input-Driven versus Output-Driven Adaptation*

The most prominent sources of adaptation are the activation of calcium-dependent (Madison and Nicoll, 1984; Vergara et al., 1998; Sah and Davies, 2000) or slow voltage-dependent (Brown and Adams, 1980; Storm, 1990) potassium currents and the inactivation of fast sodium currents (Fleidervish et al., 1996; Vilin and Ruben, 2001; Torkkeli et al., 2001). All these sources are essentially output-driven feedback components of adaptation, as they causally depend on the neuron's spiking activity (Benda and Herz, 2003).

¹This chapter is based on (Gollisch and Herz, 2004b).

On the other hand, adaptation may also contain components that are driven by the strength of the sensory or synaptic input in a feedforward way. In mechanosensory systems, e.g., the mechanical substrate may contribute to the dynamics of transduction. As originally suggested by Matthews (1931, 1933), muscle stress relaxation contributes to adaptation in vertebrate muscle spindles and tendon organs. In the Pacinian corpuscle, the viscoelasticity of the capsule leads to a characteristic rapid adaptation (Hubbard, 1958; Loewenstein and Mendelson, 1965), whereas mammalian hearing systems are influenced by adaptation of the transducer currents (Gillespie and Walker, 2001; Ricci et al., 1998; Holt and Corey, 2000).

In fact, adaptation mechanisms have been discovered acting on all principal stages of the signal-processing chain in receptor neurons, the coupling (Loewenstein, 1971; Catton, 1970; Chapman et al., 1979), the transduction (Ricci et al., 1998; Holt and Corey, 2000), and the encoding (Matthews and Stein, 1969; Purali and Rydqvist, 1998) of the primary sensory signal. For higher-order neurons, synaptic mechanisms also contribute to spike-frequency adaptation (Best and Wilson, 2004).

Such different sources of adaptation will have different effects on the coding properties of a sensory neuron. A complete understanding of the functional aspects of adaptation therefore requires the localization of its sources in the processing sequence and the identification of the causal relations between sensory input, neural activity, and the level of adaptation (Nurse, 2003).

Auditory receptor neurons of locusts reveal pronounced spike-frequency adaptation in response to prolonged acoustic stimulation. For temperatures around 30 °C, firing rates at stimulus onset can reach as high as 500 or even 600 Hz. Subsequently, they decrease to a steady-state level below 300 Hz. This spike-frequency adaptation takes place within the first few hundred milliseconds after stimulus onset. Experimental characterizations of the strength and the time constants of adaptation indicate that adaptation mainly depends on the output level of neural activity, the firing rate (Benda et al., 2001; Benda, 2002). This is consistent with studies on other insect mechanosensitive systems where output-driven components have been identified as the primary source of spike-frequency adaptation (French, 1984a; French, 1984b). In the following, we will systematically test for additional input-driven adaptation components and their effects on the spiking activity of the auditory receptor cells by analyzing *in vivo* recordings of spike trains from single receptor-cell axons in the auditory nerve.

8.2 Assessing Input-Driven Adaptation

To experimentally detect and analyze input-driven adaptation, we follow the DIRS method introduced in Section 4.3: For each recorded receptor neuron, we first identified stimuli with different sound frequencies that evoked the same steady-state firing rate. This was achieved by tuning the individual sound intensities so that a predefined firing rate was reached. These intensities were generally different for different sound frequencies due to the frequency dependence of the neuron's sensitivity. We then observed the firing rate when the stimulus was switched from one sound to the other. If only output-driven adaptation were present, the firing rate should stay at the constant steady-state level. Input-driven adaptation components, on the other hand, are disequilibrated follow-

ing such a switch in input intensity. While this component subsequently approaches its new equilibrium value, the firing rate is transiently deflected, which can easily be measured to assess the characteristics of input-driven adaptation.

Figure 8.1 shows a typical sound-evoked response of an auditory-nerve fiber. The firing rate is initially high and decays during the first few hundred milliseconds. No differences in spike patterns are apparent when responses for different tones causing similar firing rates are compared (Fig. 8.1A). The time-dependent firing rates $r(t)$ were determined as the trial average of the inverse inter-spike interval around t ,

$$r(t) = \sum_{n=1}^N \frac{1}{ISI_n(t)}, \quad (8.1)$$

where n enumerates the trials from 1 to N and $ISI_n(t)$ denotes the length of the inter-spike interval around time t of the n -th trial. Two tones can be fine-tuned so that the evoked steady-state firing rates are indistinguishable within the measurement error (Fig. 8.1B). This may require substantial differences in intensity for the two tones; in the present example, the 10-kHz tone needs to be played nearly 20 dB louder than the 4-kHz tone to be equally effective. Not only the steady-state level of firing is equal for the two tones, but the whole time course of the firing rate is strikingly similar. This is consistent with the idea that the primary component of adaptation is output-driven.

However, switching from the 10 to the 4-kHz tone after half the stimulus duration, which is accompanied by a switch to a smaller sound intensity, leads to a transient decrease in firing rate (Fig. 8.1D, left panel). This is a sign for the presence of an input-driven adaptation component. The level of input-driven adaptation is higher for the higher-intensity 10-kHz stimulus; the response is consequently suppressed after the switch while this component decays to the level of the 4-kHz tone. Conversely, a switch from the 4-kHz to the 10-kHz tone results in a transient increase in firing rate (Fig. 8.1D, right panel). After the switch, the input-driven adaptation builds up and the firing rate decays back to the steady-state level.

8.3 Characterizing Input-Driven Adaptation

In order to quantitatively characterize input-driven adaptation, we calculated firing-rate differences between the responses to a “switch stimulus”, which contained a switch from one sound frequency to the other, and the responses to a “pure stimulus”, i.e., a stimulus whose sound frequency and intensity equal that in the second half of the switch stimulus (Fig. 8.1E). We fitted exponential curves to the firing-rate differences after the switch to obtain the initial firing-rate difference Δr and the decay time constant τ .

Figure 8.2 shows a collection of such data from four different recorded receptor cells. For all these cells, the transient firing-rate deflections are clearly visible. This indicates that input-driven adaptation is a general phenomenon in these neurons. Size and time constant of the effect vary considerably between cells (note the different scales on the y-axis) and can cause firing-differences as high as 100 Hz in some cases. A clear relationship exists between the direction of the firing-rate deflection and the direction of the switch; switches from lower to higher sound intensity lead to upward deflections and vice versa.

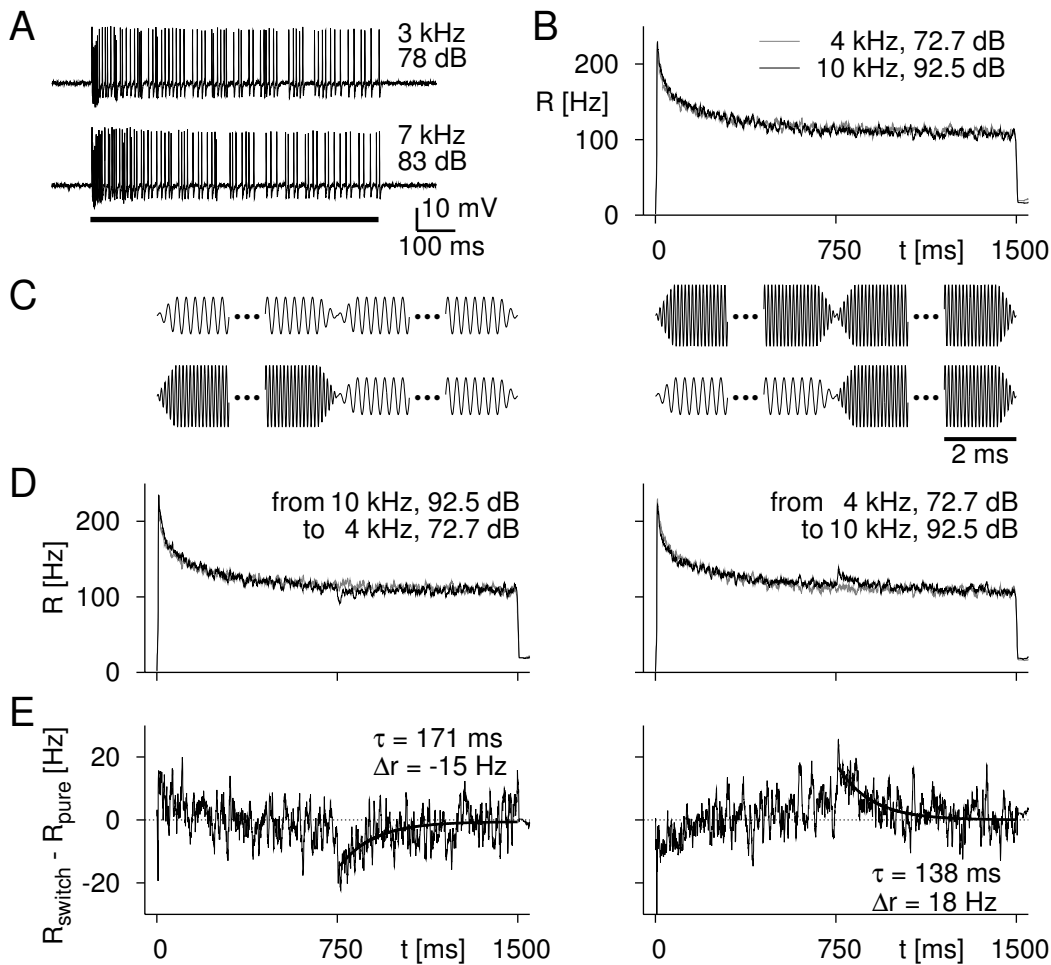


Figure 8.1: Detecting input-driven adaptation. (A) Examples of recorded spike trains. Pure tones of 3 and 7 kHz with intensities of 78 and 83 dB SPL, respectively, were presented for 750 ms (black bar). The firing rate patterns show no obvious differences for the two tones. (B) Instantaneous firing rates obtained from 94 repetitions of two stimuli with a duration of 1.5 s; sound frequencies and intensities are indicated in the plot. The intensities had been tuned to reach the same steady-state firing rate. The initial firing-rate transients are nearly identical. (C) Schematic drawings of the applied stimuli. Each stimulus half consisted of either a 4-kHz or a 10-kHz pure tone of constant intensity. For two stimuli (“switch stimuli”), the tone was switched after half the stimulus duration. The 10-kHz tone is depicted with a larger amplitude, corresponding to the higher intensity needed to drive the cell at the same steady-state firing rate as with the 4-kHz tone. (D) Firing rates in response to switch stimuli. A small downward deflection (black line, left panel) or upward deflection (black line, right panel) is apparent following the switch at $t = 750$ ms. For comparison, the gray lines show the firing rate that is obtained for the pure stimulus with sound frequency and intensity as in the second part of the switch stimulus. (E) Firing-rate differences calculated by subtracting the firing rate of the pure stimulus (gray curve in D) from that of the switch stimulus (black curve in D). The deflections are fitted by exponential curves with initial firing-rate difference Δr and time constant τ . For the switch from the high-intensity 10-kHz to the low-intensity 4-kHz stimulus (left panel), the deflection is in the downward direction and, correspondingly, Δr is negative. For the right panel, the switch is from low to high intensity, and Δr is positive.

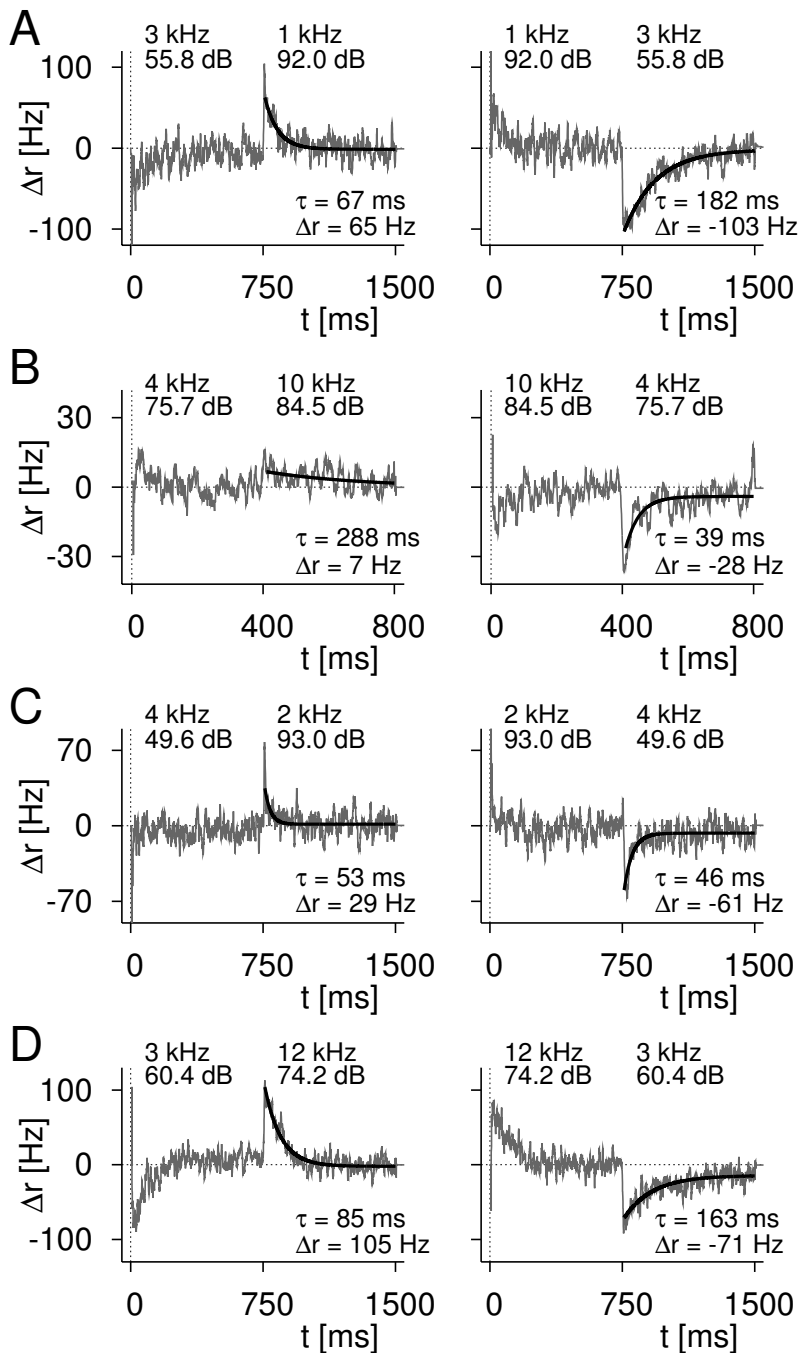


Figure 8.2: Survey of measurements of input-driven adaptation. Firing rates were determined for stimuli containing a switch from one tone to another after half the stimulus duration. The intensities of the tones had been tuned to yield the same steady-state firing rate. The parameter values in each plot indicate the sound frequency and intensity of the tones before and after the switch. For the graphs, the firing rates that were obtained for pure stimuli (sound frequency and intensity as in the second stimulus part) were subtracted. The resulting firing-rate differences (gray lines) are shown here for four different cells (A–D). In each case, both directions of switching were used, from the low-intensity to the high-intensity tone (left column) and vice versa (right column). Exponential functions (black lines) were fitted to the responses following the switch. The obtained parameters are indicated in the individual panels.

In about half of the recordings, we observed that after the switch from the higher to the lower sound intensity, the firing rate did not always reach the original level of firing within the remaining observation time. This becomes apparent in the negative asymptote of the firing-rate differences in Figs. 8.2B–D. A possible explanation is the contribution of an additional, much slower time scale to the recovery from input-driven adaptation. Such an effect was not seen for the build-up of input-driven adaptation. To account for this effect in the exponential fits, a constant offset was included as an additional fit parameter.

In some cases, the firing-rate differences directly following stimulus onset show a similar transient deflection as after the switch, but with an opposite sign (Fig. 8.2D). These cases indicate that input-driven adaptation is also part of the initial total adaptation and may account for sound-frequency-dependent differences in the time course of the firing rate after stimulus onset. Generally, though, the firing-rate differences at stimulus onset give no clear picture of input-driven adaptation (Fig. 8.2A–C), presumably because the dynamics is governed strongly by output-driven adaptation.

Note that the upward and downward deflections of the firing rate for the same cell do not necessarily have the same shape. Especially the time constants of build-up and decay may diverge considerably (Fig. 8.2A, B). This is in contrast to the minimal model that was introduced in Section 4.3 and suggests an extension where the time constant of input-driven adaptation, τ_I , either differs for build-up and decay or explicitly depends on the intensity level I . Due to the large cell-to-cell variability, however, the present data did not allow for a quantitative investigation of such a dependence.

Let us add a note of caution for the interpretation of such data. In order to deduce the existence of input-driven adaptation from the switching-induced firing-rate deflections, the sound intensities need to be tuned to yield approximately the same steady-state firing rates. In the model of Section 4.3, this was easy to achieve given the mathematical solutions, but in experiments, such a tuning relies on noisy data and is never perfect. With a mismatch of steady-state firing rates, output-driven adaptation alone could in principle lead to similar deflections of the firing rates. Imagine, e.g., that tone x leads to a higher firing rate than tone y . Output-driven adaptation will consequently be higher during presentation of tone x , and after the switch to tone y , the firing rate will be transiently reduced while this adaptation component decays to the steady-state level of tone y .

We can exclude this scenario by observing cases where a slight tuning mismatch is found together with a firing-rate deflection in the *opposite* direction to what would be expected from output-driven adaptation. In the left panel of Fig. 8.2D, e.g., we see that although the steady-state firing rate for the 3-kHz stimulus was slightly higher than for the 12-kHz stimulus (apparent in the positive offset of the firing-rate difference in the first half of the observation), the rate even *increased* further after the switch to the 12-kHz stimulus. Pure output-driven adaptation would have been expected to result in a firing-rate *decrease* triggered by the firing-rate difference before the switch, but this was apparently overcompensated by input-driven adaptation. Analyzing input-driven adaptation thus does not require a perfect match of steady-state firing rates, though one should be aware of possible influences from a mismatch. For further analysis, we included only those recordings where the firing rates, measured in the 100-ms period before the switch, matched with deviations of not more than 10%. In fact, for 13 of the 22 included recordings, the deviations were less than 3%.

8.4 Correlations with Stimulus Parameters

Figure 8.3 summarizes the data from 22 recordings. In order to distinguish the two directions of the switch, we now provide the parameters Δr and τ with indices lh for switches from lower to higher intensity and indices hl for switches from higher to lower intensity. The direction of the firing-rate deflection is governed by the sign of $I_2 - I_1$; positive

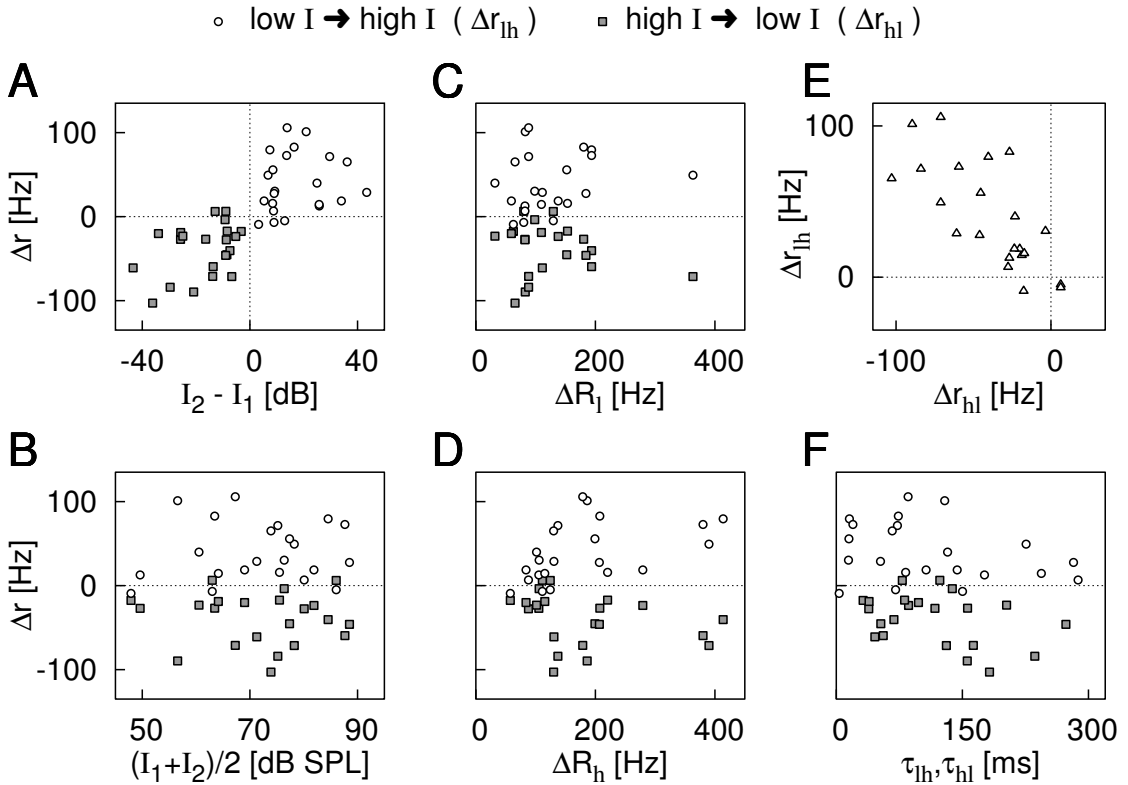


Figure 8.3: Correlation analyses of parameters characterizing input-driven adaptation. The initial firing-rate difference Δr and the decay time constant τ are obtained from exponential fits of the firing-rate transients following the stimulus switch. To distinguish between the two directions of the switch, the parameters are labeled Δr_{lh} , τ_{lh} for switches from lower to higher intensity and Δr_{hl} , τ_{hl} for switches from higher to lower intensity, and the data are plotted as open circles and gray squares, respectively. (A) Comparison of Δr with the intensity difference between the second and first stimulus part, $I_2 - I_1$. (B) Distribution of values for Δr over the average of the two intensities used in the corresponding experiment. (C) Comparison of Δr with ΔR_l , the total amount of adaptation between stimulus onset and steady state for the lower-intensity stimulus. (D) Comparison of Δr with ΔR_h , the total amount of adaptation for the higher-intensity stimulus. (E) Correlation of Δr_{lh} and Δr_{hl} obtained from the two switching directions of the same stimuli measured for the same cell. (F) Relation between Δr and the decay time constant τ of the firing-rate transients.

$I_2 - I_1$, i.e., switches from lower to higher intensity generally cause upward deflections of the firing rate ($\Delta r_{lh} > 0$) and vice versa (Fig. 8.3A). Consequently, we observe a strong correlation between $I_2 - I_1$ and the complete set of values for Δr ($\rho = 0.74$, $p < 10^{-4}$). But also restricting the data to switches from higher to lower intensity (Δr_{hl} vs. $I_2 - I_1 < 0$, gray squares in Fig. 8.3A) reveals a correlation ($\rho = 0.38$, $p = 0.078$); the higher the intensity difference, the higher generally the difference in input-driven adaptation. For switches from lower to higher intensities (Δr_{lh} vs. $I_2 - I_1 > 0$), the correlation is not significant ($\rho = 0.14$, $p = 0.52$). In contrast, we found no influence of the absolute level of intensity on the size of the firing-rate deflections (Fig. 8.3B), nor of the level of the steady-state firing rate (data not shown).

The total level of adaptation following the initial stimulus onset is denoted by ΔR_l for the lower-intensity tone and by ΔR_h for the higher-intensity tone. These are obtained from exponential fits to the pure-stimulus responses. We find that Δr_{lh} and Δr_{hl} are not corre-

lated with ΔR_l (Fig. 8.3C), but with ΔR_h , though the correlation of Δr_{hl} is not significant ($\rho = 0.47$, $p = 0.027$ for Δr_{lh} ; $\rho = -0.30$, $p = 0.17$ for Δr_{hl} ; Fig. 8.3D). Our conclusion is that input-driven adaptation is a substantial part of total adaptation for high-intensity tones, whereas it contributes less for low-intensity tones. Input-driven adaptation must thus be caused by a process that is activated more strongly at higher intensities and that reduces neural sensitivity in the high-intensity regime. This is opposed to hypothetical rival processes that would be activated at lower intensities and that could cause the firing-rate deflections by increasing sensitivity in the low-intensity regime.

The firing-rate deflections for both switching directions of two tones measured for the same cell are of comparable size (Fig. 8.3E) as seen in the correlation between Δr_{hl} and Δr_{lh} ($\rho = -0.74$, $p < 10^{-3}$). This supports the idea that the same amount of input-driven adaptation builds up after the switch from lower to higher intensity as decays after the switch from higher to lower intensity.

Figure 8.3F shows that the time constants of the firing-rate deflections were distributed over a wide range between 10 and 300 ms. τ_{lh} and Δr_{lh} showed no significant correlation ($p = 0.20$). But for the shift from higher to lower intensity, the time constant τ_{hl} was correlated with Δr_{hl} ($\rho = -0.3708$, $p = 0.089$). As we had seen in the model of Section 4.3, time constants for the firing-rate deflections may reflect the mixture of input-driven and output-driven adaptation. Two simple explanations of this correlation are therefore possible: 1) the strength and the time constant of input-driven adaptation within a neuron are coupled, or 2) a larger effect of input-driven adaptation leads to a larger contribution of the corresponding time constant to the firing-rate transient. Which of these hypotheses may hold is presently undecided.

8.5 Discussion of the Experimental Approach

Spike-frequency adaptation is ubiquitous in neural systems. Several functions are linked to adaptation, including control of the dynamic operating range, noise suppression, and high-pass filtering (Kandel et al., 2000). Furthermore, the temporal dynamics of adaptation allow specific computational strategies (Adorjan et al., 2002; Schwabe and Obermayer, 2003). At the sensory periphery, adaptation may also contribute to the protection of receptor neuron's structures and transduction channels from over-stimulation as part of an allostatic regulation (McEwen and Wingfield, 2003).

A functional study of adaptation in a specific system should include a determination of its causal dependencies. What aspects of the stimulus or of the neural activity trigger adaptation? In many neuron types, adaptation is thought to be driven by the cells own spiking activity. Many adaptation currents based on cell-membrane-intrinsic ion channels fall into this class of output-driven adaptation mechanisms (Benda and Herz, 2003).

The approach presented in this chapter for analyzing input-driven adaptation components only requires measurements of the spiking activity of the neuron. This is especially advantageous for *in vivo* studies and when intracellular recordings from the soma or dendrites are not available and the application of biomedical agents, such as channel blockers, is difficult or impossible. A requirement for being able to observe firing-rate transients caused by input-driven adaptation after a stimulus switch is the existence of different stimulus types (such as acoustic frequencies or locations of visual stimuli) that drive the

neuron equally despite different input levels. For high-dimensional stimulus spaces, it is likely that such stimuli exist and can be identified experimentally, but this has to be decided on a case-by-case basis.

Since we measure the difference of adaptation for two stimuli, we assess the existence and relative strength of input-driven adaptation, but we do not determine its absolute level. The input-driven adaptation component appears to be considerably weaker than output-driven adaptation, as the phasic parts of the receptor cell's activity following stimulus onset are strongly dependent on the level of the output firing rate. But it remains an open issue to actually quantify the contribution of input-driven adaptation to total adaptation. Performing the same experiment with more than just two tones could help answering this question, as the resulting set of firing-rate differences may suggest a certain functional dependence of the level of input-driven adaptation on the sound intensity. The limited recording time, though, currently precludes such an experiment for locust auditory receptor cells.

8.6 Mechanistic Foundation

What is the biophysical mechanism behind input-driven adaptation? As we have seen so far, the sound stimulus is successively transformed; the sound-pressure waves cause oscillations of the tympanic membrane, the animal's ear drum, which in turn lead to the opening of mechanosensory ion channels in the attached receptor neurons, and finally the provoked transduction currents may trigger action potentials. At which point in this cascade can input-driven adaptation occur?

The information about the absolute intensity is only present at the very first step of the processing chain, the coupling of the air-pressure wave to the tympanum. By its resonance properties, the tympanum filters the sound wave (Michelsen, 1971b; Schiolten et al., 1981); subsequent stages of the transduction chain obtain only information about the filtered stimulus intensities and thus cannot evoke an adaptation mechanism that depends on the absolute intensity level. We conclude that the observed adaptation process is an effect of the mechanical coupling of the stimulus to the tympanum. Similar influences of mechanical structures have been described in vertebrate muscle spindles (Matthews, 1931; Matthews, 1933) and the Pacinian corpuscle (Hubbard, 1958; Loewenstein and Mendelson, 1965).

In the cascade-model framework of Chapter 7, the mechanical coupling is captured by the temporal filter $l(\tau)$. An adaptation-induced change in the mechanical properties should therefore be reflected in a change of $l(\tau)$. One may speculate that the reduced relative sensitivity at high intensities, which effectively should lead to a sharpening of the frequency tuning over time, is mediated by an increase of the decay time constant of $l(\tau)$. In other words, a longer temporal filter $l(\tau)$ during the steady state as compared to stimulus onset could sharpen the frequency tuning and thus suppress the responses to sound frequencies which do not lie near the cell's characteristic frequency. This constitutes a straight-forward way of incorporating the observed phenomena into the cascade model of the auditory transduction chain. Furthermore, an experimental test – e.g. by measuring the temporal filter of the tympanum as in Chapter 6 in an adapted and a non-adapted state, provided the necessary longer recording times are available – would be highly interesting.

The putative mechanical origin opens the possibility of a complementary characterization via the mechanical properties of the tympanum. Laser interferometry allows the observation of the tympanic oscillations under acoustic stimulation (Schiolten et al., 1981; Robert and Göpfert, 2002). Our results predict that a slight decrease in oscillation amplitude should be visible during the first few hundred milliseconds in response to constant-intensity stimulation. However, the auditory ganglion, which contains the receptor-cell somata and which is attached to the tympanum, also vibrates during sound stimulation (Stephen and Bennet-Clark, 1982) and thus contributes to the mechanical deformations that induce transduction. It could well be that part (or all) of input-driven adaptation is associated with this movement, which is considerably harder to observe in detail. Furthermore, the inhomogeneous structure of the tympanum makes it difficult to relate such observations to individual receptor cells because they are attached at different positions on the tympanic membrane. Here, on the other hand, we were able to observe the effect of this adaptation component on the spiking activity of single neurons.

8.7 *Possible Functions*

What function may this adaptation component serve? The observed phenomenon might be a consequence of mechanical constraints and nonlinear properties that come with the specific way of stimulus coupling. This could in fact lead to a protection of the delicate mechanical structures from damage at high sound intensities. On the other hand, input-driven adaptation components in principle open up new possibilities for coding strategies; the relative sensitivities of the neuron to different sound frequencies change over time depending on previous intensity levels.

It is yet unclear, though, what benefit would result from such a dynamic reorganization of the code. Natural stimuli for grasshoppers, such as their courtship songs, usually contain broad carrier-frequency bands (von Helversen and von Helversen, 1994; Stumpner and von Helversen, 2001). The coding properties of grasshopper auditory receptor cells have been shown to be particularly adapted to specific aspects of these stimuli (Meyer and Elsner, 1996; Machens et al., 2001) and to allow discrimination between slightly different songs (Machens et al., 2003). Investigating input-driven adaptation using these more complex signals may thus shed light on how this adaptation component affects neural coding.

Further insight about the functional roles of input-driven and output-driven adaptation may result from comparisons with other sensory modalities. In fact, olfactory receptor cells have been shown to be affected by adaptation mechanisms originating in the ciliary transduction machinery as well as in somatic ion channels (Narusuye et al., 2003). These mechanisms of input-driven and output-driven adaptation may have different biophysical origins as compared to auditory receptor cells, but could constitute analogous functional operations. Similarly, photoreceptor cells are influenced by several different adaptation mechanisms along the phototransduction pathway (Lamb and Pugh, 1992; Hardie and Raghu, 2001), and their relative importance is subject to ongoing research (Bownds and Arshavsky, 1995).

The approach presented in this chapter is not specific to the auditory system and may thus lead to similar insight in other sensory systems. For higher-order neurons, it may be

applied to disentangle adaptation contributions that are caused by the activity of the investigated neuron itself and those that are inherited from previous processing steps such as short-term synaptic plasticity. As in the present study, no dendritic or somatic measurements are needed; extracellular recordings of spiking activity would suffice to identify and discriminate different (sub-)cellular adaptation components.

CHAPTER SUMMARY:

Spike-frequency adaptation modifies a neuron's input-output relation depending on the history of stimulation and activity. For a functional characterization of adaptation, the identification of its causes is an essential aspect. In this chapter, we have seen how input-driven adaptation can be experimentally uncovered from *in vivo* recordings of spiking activity. The applied method is based on measuring transient deflections of the firing rate, which are caused by switches between different stimuli corresponding to the same steady-state response. The observed input-driven adaptation component is likely to result from specific mechanical properties of the sound-receiving structures in the ear. It thus affects the first stage of the auditory transduction chain, the coupling of the acoustic signal to the tympanum.

CONCLUSION AND OUTLOOK

In this thesis, a modular study of the auditory transduction chain in receptor cells of the locust ear was presented. The experimental data were obtained from *in vivo* recordings of spike trains from single fibers in the auditory nerve. As an appropriate theoretical framework for studying the auditory transduction chain, cascade models were identified. Their basic building blocks, temporal linear filters and static nonlinear transformations, constitute the modules of the studied system. For determining the cascade structure and the parameters of the modules, a suitable experimental approach to collecting data in electrophysiological recordings was developed. A key feature of the new method is the identification of different stimuli that lead to the same response of the system.

By applying this method, we found that the auditory transduction chain can be described by a sequence of four generic signal-processing operations. The first and third step of this cascade are formed by temporal linear filters; in the second and in the final step, static nonlinear transformations act on the signal. The model structure thus corresponds to an LNLN cascade, which has a straight-forward biophysical interpretation. The mechanical coupling of the tympanum and the accumulation of charge at the neural membrane correspond to the linear filtering processes; the mechanosensory transduction process that converts the tympanic vibration into an electrical signal as well as the generation of spikes induce the nonlinear transformations. Furthermore, an investigation of adaptation components showed that – in addition to commonly assumed output-driven spike-frequency adaptation – this transduction chain is influenced by an input-driven adaptation component. This phenomenon appeared to be of mechanical origin acting on the first stage, the coupling of the sound signal to the tympanum.

Discussion of the Cascade Model

The linearity of the first model step agrees with laser interferometric observations (Michelsen, 1979; Schiolten et al., 1981). However, otoacoustic emissions in the grasshopper ear discovered by Kössl and Boyan (1998a;b) provided evidence that mechanical nonlinearities do influence the stimulus coupling. The nonlinear contributions detected in these studies were small, though, and appear to be negligible for modeling the coding properties of the receptor neurons. In the second model step, the nonlinear transformation induced by the mechanosensory transduction was found to match a simple squaring operation. This led to the conclusion that the intensity coding of stationary signals in these receptor neurons corresponds to an energy-integration mechanism. Furthermore, previous studies of hair cells had shown that the DC component of currents

evoked by stationary sine tones depends approximately quadratically on sound amplitude (Dallos, 1985), thus indicating a general auditory coding principle.

For the electrical integration of the receptor cell in the third model step, the neuron's membrane time constant was extracted, which had not been accessible before. The small values in the sub-millisecond range, which we found, reflect the demands for high temporal resolution in the auditory periphery. This finding corresponds well with observations of precisely timed spikes and high information rates of spike trains recorded in these cells (Watzl et al., 2003). In the final model step, spike generation was captured by a static nonlinearity. This description does not include specific effects of the spike-generation process on spike timing. Such effects are likely to exist, e.g., in the form of spike jitter and systematic shifts in latency depending on the input intensity. In the context of the present study, it was not necessary to include an explicit model of spike timing, as we focused on firing rates and spike probabilities only. For a complete description of the signal-processing characteristics associated with these neurons, however, the cascade structure should be extended accordingly.

Continuative Studies of Auditory Transduction

The results of the present work pave the way to a series of more detailed investigations of the auditory transduction chain. First, the general model structure obtained in Chapter 7 suggests to test predictions obtained for short stimuli with wave forms other than clicks, such as short pieces of sine tones. This could be extended to longer stimuli after combining the present description with modules that go beyond the primary signal-transduction cascade and capture effects of refractoriness and adaptation. Appropriate frameworks for both these phenomena already exist. Many variants of adaptation can be captured as subtractive contributions to the spike-generating current (Benda and Herz, 2003). This suggests that the final step of the cascade, $r = g(J)$, can be substituted by $r = g(J - I_A)$, where I_A describes the level of adaptation. Such a modification may yield a suitable first approach to including adaptation phenomena. On the other hand, input-driven adaptation, as discussed in Chapter 8, would require a stimulus-dependent modification of the input filter $l(\tau)$, but may be negligible for initial investigations. Refractoriness has successfully been captured in a recovery-function framework (Berry and Meister, 1998; Schaette et al., 2004). Here, this corresponds to adjusting the final model step according to $r(t) = g(J) \cdot w(t - t_{\text{last}})$, where the recovery function $w(t - t_{\text{last}})$ modifies the spike probability according to the time that has passed since the last spike at t_{last} . Together, these modifications may result in a simple, yet biologically inspired and accurate description of the receptor neuron's input-output relation for arbitrary sound signals.

With a complete model description of neural activity in these cells, the foundations are laid for a theoretical investigation of the information-theoretic and signal-detection capacities measured for these neurons by other studies (Machens et al., 2001; Machens et al., 2003; Watzl et al., 2003; Machens et al., 2004). One may thus ask how the model parameters, e.g., the membrane time constant, influence the precision of single spikes and information transmission for particular signal features. These studies could be complemented by experiments, which extract both the cascade model's constituents and the information-theoretic characteristics during single recordings in order to investigate cor-

relations between these different aspects. This would allow one to test general hypotheses, such as the enhancement of information rates by shorter integration time constants.

Further insight about auditory transduction can be expected from comparing the characteristics of the model constituents for different experimental situations. For example, essential aspects of the biophysics underlying signal processing may result from asking how the shapes and time constants of the involved linear filters are affected by different states of adaptation or different temperatures. The effect of adaptation could be tested by performing the CIRS measurements twice, once exactly as in the present study, Chapter 6, and once with a pre-adapting stimulus that precedes every click combination. Such an experiment can also be used to investigate the connection between the cascade structure of auditory transduction and the phenomenon of input-driven adaptation, which is expected to affect the first linear filter, $l(\tau)$. In a different study, the effect of temperature on the processes of the auditory transduction chain may in particular address the question how mechanical and electrical processes differ in their temperature dependence. This question is particularly interesting for insect systems, where function has to be preserved despite large fluctuations in body temperature.

Generalization of the Methodological Framework

The methodological framework that was presented in this thesis is not restricted to the analysis of the auditory transduction chain. In fact, signal-processing sequences combining generic filters and transformations are ubiquitous on all levels of biological organization, from molecular pathways for gene regulation to large-scale relay structures in the neural networks of sensory processing. Application of iso-response methods to such systems may lead to similar new insights as in the present study.

The CIRS method will be most directly applicable to systems that share the same general structure with the LNLN cascade of auditory transduction. In the present case, analysis was facilitated by identifying, at the outset, an explicit expression for the first nonlinearity from specific measurements of iso-response sets. This may not always be possible. An alternative way for determining the proper form of the first nonlinear transformation may be found by combining iso-response methods with standard correlation techniques of systems identification. Methods aimed at *structure detection* (Billings, 1980) may be used to identify and characterize certain nonlinearities within cascade models. For example, the intermediate nonlinearity in putative LNL cascades can be detected by a correlation analysis. The nonlinearity will cause deviations from the output of a best-fit linear model, and correlating these deviations with the output of nonlinear “test models” can be used to estimate the form of the nonlinearity (*Douce’s algorithm*, see (Billings, 1980) for a review). If such a scheme can be applied within an iso-response set, the first nonlinearity of an LNLN cascade may be detectable in a general situation.

Furthermore, the CIRS method may even be applicable in cases where no or little prior information about the first nonlinearity can be obtained. In that case, one may resort to a parametrization of the nonlinearity and subsequently estimate its exact shape numerically. The required information for constraining the parameter estimates could come from additional measurements obtained in the same fashion as in Fig. 6.8. Here, two measurements at each Δt were needed to determine the filter parameters $L(\Delta t)$ and $Q(\Delta t)$. Loosely

speaking, a third measurement could be used to determine how “good” the estimate of the nonlinearity is, which underlies the estimation of L and Q . The parametrization of the nonlinearity therefore gives rise to *hyperparameters* for the estimation of the filters. A numerical technique that deals with such combined estimation problems is the *estimation maximization algorithms* (Hartley, 1958; Neal and Hinton, 1998), which constitutes a generic, iterative estimation procedure for a model’s parameters and hyperparameters. This estimation technique has been successfully applied, e.g., to hierarchical linear models for neuroimaging data (Friston et al., 2002) that share some of the sequential processing characteristics with transduction chains.

An important aspect in generalizing the methodological framework will be to study the influence of noise on parameter estimation in the CIRS method. For example, if the measured level of output activity is subject to random noise, a strong nonlinearity in the final step of the cascade may transform random fluctuations of the measured output into a bias of estimators for preceding model steps. The severity of the bias and its dependence on particular estimation techniques that may be applied in the experimental approach can be investigated by simulation studies.

An interesting future application of iso-response methods may result from studying feedback systems. For applying the DIRS method, we already used the fact that any purely output-dependent feedback component assumes the same state for different iso-response stimuli. Combining this concept with the CIRS approach may help discern feedforward and feedback contributions. This idea is clarified by a simple scenario, where the output r is a function of several input components A_1, A_2, \dots and several feedback components $B_1(r), B_2(r), \dots$: $r = g(A_1, A_2, \dots, B_1(r), B_2(r), \dots)$. Within an iso-response set, each $B_n(r)$ component remains constant, and the functional dependence on the A_n components can therefore be analyzed independently as before by the CIRS method.

Concerning the DIRS method, extensions would be desirable that yield a better separation of input-driven and output-driven dynamic processes. In the analysis of input-driven and output-driven adaptation, we saw that the time constants of the two processes were still mixed after switching from one iso-response stimulus to the other. This mixing was due to a secondary effect in output-driven adaptation in response to the firing-rate transient. A possible solution in order to overcome this effect would be to augment the switch between the two stimuli with a gradual change of stimulus parameters that is aimed at truly keeping the output firing rate constant. The gradual stimulus changes required to achieve this could be obtained by applying an iterative online procedure, which successively improves the estimate of the required stimulus change. Measurements without additional gradual stimulus changes, as presented in this work, could be used to determine promising initial estimates for this procedure. Finally, the determined gradual stimulus change provides the desired information about the dynamics of the input-driven processes, independently of output-driven dynamics.¹ However, such a scheme will require substantially longer experimental recording times, and finding a suitably fast algorithm for the iterative optimization of the stimulus change will be crucial to such an enterprise.

¹The suggested concept is based on a similar experimental idea by J. Benda and H. Schütze for measuring the firing-rate dependence of output-driven adaptation following stimulus onset (personal communication).

Limitations of the Method

The application of iso-response methods is based on the possibility to detect multiple stimuli that yield the same response. Generally, the dimensional reduction associated with mapping a high-dimensional input space onto a smaller set of outputs should provide for the existence of stimulus sub-spaces in which the system's response is invariant. Detecting such sub-spaces, however, may present technical difficulties. For example, the response space can be more complex than the one-dimensional examples of firing rate and spike probability regarded in this study. An example is a bursting neuron whose response may contain nearly independent information in burst timing and in the number of occurring spikes. In such cases, simple linear search algorithms may not suffice for determining iso-response stimuli. On an abstract level, the task of identifying inputs for a given output corresponds to a numerical "root-finding" problem, which is notoriously difficult for multi-dimensional outputs (Press et al., 1992), especially if the system comprises substantial non-monotonic behavior. In particular cases, it may then be beneficial to disregard certain response characteristics and consider only a projection of the response onto a smaller sub-space. Consequently, the interpretability of the data will depend on the experimenter's skill in choosing appropriate response attributes for describing the system.

The efficiency of extracting iso-response sets for a given system depends on the feasibility of quick read-outs of the system's response for iteratively adapting the inputs as required. If the system takes a long time to either settle to a response or recover from an earlier response or even shows hysteresis effects, tuning inputs by an automatic feedback loop may not be possible, and the extraction of iso-response sets may thus not be appropriate for studying such systems.

The question of *structure detection*, which was already alluded to above, presents a general problem in the application of cascade models. Most applications rely on previous knowledge about the number and order of linear and nonlinear components. In fact, analyzing the structure of iso-response sets, as we have seen in the application of the IRS method in this work, may help reveal certain nonlinear components and thus contribute to structure detection by suggesting a particular cascade model. In general, however, the appropriate cascade may not be directly available from the iso-response data. Especially weak nonlinearities will be difficult to detect, as their influence on the composition of the iso-response set is correspondingly small. In such cases, the system's anatomy alone may provide a suitable guess for the cascade structure that can be tested with particular iso-response sets.

Presently, application of the CIRS method is limited to cascades with at most two nonlinear transformations. The most likely possibility to cope with even more complex systems, at least in certain cases, seems to be the exploitation of differences in time scales or other appropriate means of breaking down the complete system into appropriate modules, which may be on a higher organizational level than the constituents of the cascade models investigated so far. By choosing stimuli appropriately, one may be able to obtain iso-response sets that reflect the features of a particular module. Furthermore, the presented methods of analyzing cascade structures rely on the separability of dynamic and nonlinear effects. If the system cannot be broken down into temporal linear filters and static nonlinear transformations, the CIRS method will generally not be able to resolve the individual steps.

Closure

The investigation of complex, multi-process biological systems by integrating approaches and analysis techniques from different scientific disciplines has grown over recent years to become a new focus point of biological research, often termed *systems biology*. The novel experimental and theoretical questions that come along with such a new paradigm raise the need for new techniques and methods of integrating experimental data into comprehensive models. The extensions presented in this thesis of classical iso-response investigations may contribute to this development, as they provide new perspectives for analyzing complex cascade-structured systems. Several possibilities to generalize the methodology are feasible, as demonstrated, in order to increase the scope of this framework beyond the applications in this work. The presented results, which were obtained with these methods, revealed the characteristics of the various modules that constitute sensory transduction in locust auditory receptor cells. These insights provide a foundation for investigating the relationships between the biophysical dynamics and the signal encoding in sensory systems.

APPENDICES

A *Electrophysiology*

All experiments were performed on adult male and female migratory locusts (*Locusta migratoria* L.). The tympanic auditory organ of these animals is located in the first abdominal segment. After decapitation, removal of the legs, wings, intestines, and the dorsal part of the thorax, the animal was waxed to a holder, and the metathoracic ganglion and the auditory nerve were exposed. Action potentials from auditory receptor-cell axons were recorded intracellularly in the auditory nerve with standard glass microelectrodes (borosilicate, GC100F-10, Harvard Apparatus Ltd., Edenbridge, UK), filled with a 1 mol/l KCl solution (50–110 M Ω resistance). The signals were amplified (BRAMP-01, NPI electronic, Tamm, Germany) and recorded by a data acquisition board (PCI-MIO-16E-1, National Instruments, München, Germany) with a sampling rate of 10 kHz. Detection of action potentials and generation of acoustic signals were controlled online by the custom-made *Online Electrophysiology Laboratory (OEL)* software. Stimuli were transmitted by the above-mentioned data acquisition board with a conversion rate of 100 kHz to the loudspeakers (Esotec D-260, Dynaudio, Skanderborg, Denmark, on a DCA 450 amplifier, Denon Electronic GmbH, Ratingen, Germany). These were mounted at 30 cm distance on each side of the animal. Stimuli were played only by the loudspeaker ipsilateral to the recorded auditory nerve. The proper transmission of the sound signals used in this study was verified by playing samples of the stimuli while recording the sound at the animal's location with a high-precision microphone (40AC, G.R.A.S. Sound & Vibration, Vedbæk, Denmark, on a 2690 conditioning amplifier, Brüel & Kjær, Langen, Germany). During the experiments, animals were kept either at room temperature, which was about 20 °C, or at a constant temperature of 30 °C. The experiments were performed in a Faraday cage lined with sound-attenuating foam to reduce echoes.

B Solutions for the Adaptation Model

We here present analytical solutions for the adaptation model introduced in Section 4.3. With the simplifying linearity assumptions $g(x) = x$, $A_{R,\infty}(R) = \alpha \cdot R$, and $A_{I,\infty}(I) = \beta \cdot I$, the model reads

$$R = k \cdot I - A_R - A_I, \quad (\text{B.1})$$

$$\tau_R \cdot \frac{dA_R}{dt} = \alpha \cdot R - A_R, \quad (\text{B.2})$$

$$\tau_I \cdot \frac{dA_I}{dt} = \beta \cdot I - A_I. \quad (\text{B.3})$$

The differential equations are linear and of first order. For constant input I , Eq. (B.3) can be solved directly for the initial condition $A_I(0) = A_{I,0}$. Substituting A_I in Eq. (B.1) and subsequently R in Eq. (B.2), we also find a solution for $A_R(t)$ with the initial condition $A_R(0) = A_{R,0}$. Together, this yields

$$R(t) = \frac{(k - \beta)I}{\alpha + 1} + \frac{(\beta I - A_{I,0}) \cdot (1 - \tau_R/\tau_I)}{\alpha + 1 - \tau_R/\tau_I} \cdot \exp\left(-\frac{t}{\tau_I}\right) + \left(\frac{\alpha(k - \beta)I}{\alpha + 1} + \frac{\alpha(\beta I - A_{I,0})}{\alpha + 1 - \tau_R/\tau_I} - A_{R,0}\right) \cdot \exp\left(-\frac{\alpha + 1}{\tau_R}t\right), \quad (\text{B.4})$$

$$A_R(t) = \frac{\alpha(k - \beta)I}{\alpha + 1} + \frac{\alpha(\beta I - A_{I,0})}{\alpha + 1 - \tau_R/\tau_I} \cdot \exp\left(-\frac{t}{\tau_I}\right) + \left(A_{R,0} - \frac{\alpha(k - \beta)I}{\alpha + 1} - \frac{\alpha(\beta I - A_{I,0})}{\alpha + 1 - \tau_R/\tau_I}\right) \cdot \exp\left(-\frac{\alpha + 1}{\tau_R}t\right), \quad (\text{B.5})$$

$$A_I(t) = \beta I + (A_{I,0} - \beta I) \cdot \exp\left(-\frac{t}{\tau_I}\right).$$

Note that $R(t)$ contains two exponential parts corresponding to the two time scales in the model. The time constant of A_R is rescaled by the factor $1/(\alpha + 1)$ leading to faster dynamics as a result of the feedback between R and A_R . If the two time constants τ_R and τ_I are very similar in value, the first exponential contribution, containing the term $\exp(-t/\tau_I)$, becomes very small due to the $(1 - \tau_R/\tau_I)$ -term. The firing rate at onset is then seemingly dominated by a single process on a time scale that may be much faster than both adaptation processes.

In the context of the present study, we need the solution for stimulus onset and after the switch between stimuli with different I and k . At stimulus onset, the initial conditions are given by $A_{R,0} = A_{I,0} = 0$. If the switch happens long enough after stimulus onset, the system has approximately reached its steady state, and $A_{R,0}$ and $A_{I,0}$ can be obtained from the steady-state conditions. These are found by setting $dA_R/dt = dA_I/dt = 0$:

$$R = \frac{(k - \beta)I}{\alpha + 1}, \quad A_R = \frac{\alpha(k - \beta)I}{\alpha + 1}, \quad A_I = \beta I. \quad (\text{B.6})$$

Note that the values of k and I of the tone prior to the switch have to be inserted in these equations in order to obtain $A_{R,0}$ and $A_{I,0}$ as initial conditions for the system after the switch.

C Measurement Directions for Iso-Response Sets

For measuring iso-response sets, the directions in stimulus space have to be chosen along which to search for a predefined response. In order to yield most informative data, these directions should generally be homogeneously spaced on the relevant scales of the stimulus space. For the measurements of iso-response sets in the two-dimensional stimulus space (A_1, A_2) of Section 5.3, these relevant scales are provided by the filter constants C_1 and C_2 , which incorporate the sensitivity of the receptor cell for the corresponding sound frequencies. The measurement directions, as shown by the gray arrows in Fig. 5.2, were determined in the following way: First, estimates C_1^{est} and C_2^{est} of the filter constants were obtained from measurements with each pure tone alone. For subsequent measurements of iso-response stimuli, the ratio A_1/A_2 was fixed so that the radial direction of measurement was defined by the angle α of the corresponding straight line $A_2 = k \cdot A_1$ in the A_1 – A_2 plane as was shown in Fig. 5.2. The different ratios A_1/A_2 were then chosen so that the angles α were homogeneously spaced in the interval $[0^\circ, 90^\circ]$. The relationship between A_1/A_2 and the angle α is given by the equation for the slope of a straight line,

$$\tan \alpha = \frac{A_1/C_1^{\text{est}}}{A_2/C_2^{\text{est}}}. \quad (\text{C.1})$$

Similarly, for the experiments with superpositions of three tones in Section 5.5, estimates C_1^{est} , C_2^{est} , C_3^{est} of the filter constants were first obtained with pure-tone measurements. Subsequently, iso-response stimuli were measured along radial directions defined by keeping the mutual ratios

$$\frac{A_1}{C_1^{\text{est}}} : \frac{A_2}{C_2^{\text{est}}} : \frac{A_3}{C_3^{\text{est}}} \quad (\text{C.2})$$

fixed. For each recording, the ratios 1 : 1 : 1, 2 : 1 : 1, 1 : 2 : 1, and 1 : 1 : 2 were used.

D Least Squares Method for Fitting Iso-Response Sets

In order to compare the iso-response sets obtained in Chapter 5 with the predictions of the model hypotheses, the free parameters C_1 and C_2 have to be fitted to the data. Fitting iso-response data must be handled with care as the components of the data points do not have typical relations of independent and dependent variables. For example, fitting a function to the amplitude combinations (A_1, A_2) by regarding A_2 as a function of A_1 would break the symmetry between the two components and induce an artificial and unnatural weighting of data points. Data points in regions where the iso-response curve becomes very steep in the A_1 – A_2 plot, e.g., at the x -axis intersection of the ellipse, would “clamp” the fitted curve to particular values. Furthermore, the relevant scales of the axes should be taken into account, i.e., the fitting procedure should be robust against large differences in the sensitivity for the individual components of the iso-response stimuli.

We therefore take the following approach for fitting iso-response data, as here explained in detail for the comparison of the different hypotheses in Chapter 5: We first normalize the measured amplitudes $A_1^{(n)}, A_2^{(n)}$ by the filter constants C_1, C_2 , where n enumerates all measured iso-response stimuli. We then regard the radial distance of the data points $\left(\frac{A_1^{(n)}}{C_1}, \frac{A_2^{(n)}}{C_2}\right)$ from the origin as a function of the ratio $\rho_n = \frac{A_1^{(n)}/C_1}{A_2^{(n)}/C_2}$. The ra-

dial distance is given by $\sqrt{\left(\frac{A_1^{(n)}}{C_1}\right)^2 + \left(\frac{A_2^{(n)}}{C_2}\right)^2}$ and constitutes a natural choice, as the rate-intensity functions that led to the data points were measured in the radial direction. For the three hypotheses, we denote the predicted radial distance by d_m , where m stands for the particular model hypothesis ($m = AH, EH,$ or PH). d_m can be obtained from the model as a function of ρ_n and corresponds to the normalized distance from the origin to the respective iso-firing-rate curve in Fig. 5.2. For the amplitude hypothesis, one obtains $d_{AH}(\rho_n) = \frac{\sqrt{\rho_n^2 + 1}}{\rho_n + 1}$ and for the energy hypothesis, $d_{EH}(\rho_n) = 1$. For the pressure hypothesis, $d_{PH}(\rho_n)$ has to be determined numerically by solving the equation

$$\langle |\tilde{A}(t)| \rangle = \frac{1}{\tau} \int_0^\tau dt \left| \frac{A_1}{C_1} \sin(2\pi f_1 t) + \frac{A_2}{C_2} \sin(2\pi f_2 t) \right| = \text{constant} \quad (\text{D.1})$$

for pairs $\left(\frac{A_1}{C_1}, \frac{A_2}{C_2}\right)$. The integration time τ has to be chosen large enough to cover many cycles of the sine waves in the signal, so that the potential phase offsets of the two sine functions, cf. Eq. (5.2), do not contribute.

Estimating C_1 and C_2 then corresponds to minimizing the χ^2 function for the radial distance for each model m ,

$$\chi_m^2(C_1, C_2) = \sum_n \frac{\left[\sqrt{\left(\frac{A_1^{(n)}}{C_1}\right)^2 + \left(\frac{A_2^{(n)}}{C_2}\right)^2} - d_m(\rho_n) \right]^2}{\sigma_n^2}, \quad (\text{D.2})$$

with respect to C_1 and C_2 . The contributions of the data points are weighted by the mea-

surement errors σ_n , which follow from the measurement errors $\Delta A_1^{(n)}$ and $\Delta A_2^{(n)}$ for $A_1^{(n)}$ and $A_2^{(n)}$, respectively, by the law of error propagation as

$$\sigma_n = \sqrt{\frac{\left(\frac{A_1^{(n)} \cdot \Delta A_1^{(n)}}{C_1^2}\right)^2 + \left(\frac{A_2^{(n)} \cdot \Delta A_2^{(n)}}{C_2^2}\right)^2}{\left(\frac{A_1^{(n)}}{C_1}\right)^2 + \left(\frac{A_2^{(n)}}{C_2}\right)^2}}. \quad (\text{D.3})$$

Minimization the χ^2 function was achieved with the Matlab Statistical Toolbox (Mathworks, Inc., version 6.5, release 13). The fitted curves and the χ^2 values obtained from the fits were used for further statistical analysis.

E Bayesian Estimate of Hypotheses Probabilities

To quantitatively evaluate how the experimental data of the iso-response sets suggest the preference of one hypothesis over another, we calculated the posterior Bayesian probabilities for the model hypotheses. According to Bayes' formula, the conditional probability of a model given the data is obtained as

$$p(\text{model } m|\text{data}) = \frac{p(\text{data}|\text{model } m)}{p(\text{data})} \cdot p(\text{model } m), \quad (\text{E.1})$$

where m enumerates the different models that are compared and $p(\text{data})$ is given by $p(\text{data}) = \sum_m p(\text{data}|\text{model } m) \cdot p(\text{model } m)$. If there is no *a priori* evidence for any model, the prior probabilities for the models are to be set to $p(\text{model } m) = 1/M$, where M is the number of models investigated.

For the comparison of the energy and pressure hypotheses in Chapter 5, the probabilities $p(\text{data}|\text{model } m)$ were calculated from the difference between $\sqrt{\left(\frac{A_1^{(n)}}{C_1}\right)^2 + \left(\frac{A_2^{(n)}}{C_2}\right)^2}$ and the corresponding model predictions $d_m(\rho_n)$, which is obtained as a function of the ratio $\rho_n = \frac{A_1^{(n)}/C_1}{A_2^{(n)}/C_2}$ as explained in the previous appendix section. The data points are measured independently, and the corresponding error measures are assumed to follow a Gaussian distribution of standard deviations σ_n , given by the measurement errors as in Eq. (D.3). With a finite and fixed measurement resolution Δ , we find

$$p(\text{data}|\text{model } m) = \Delta \cdot \prod_n \frac{1}{\sqrt{2\pi\sigma_n^2}} \exp \left\{ -\frac{1}{2\sigma_n^2} \cdot \left[\sqrt{\left(\frac{A_1^{(n)}}{C_1}\right)^2 + \left(\frac{A_2^{(n)}}{C_2}\right)^2} - d_m(\rho_n) \right]^2 \right\} \quad (\text{E.2})$$

An analogous formula was used in the case of superpositions of three pure tones.

F Shifts of the Rate-Intensity Functions

The spectral-integration model of Chapter 5 can be used to predict rate-intensity functions for stationary stimuli with arbitrary frequency content. Doing so requires knowledge of a single rate-intensity function and all relevant filter constants. Let us assume that the rate-intensity function $r^{\text{pt}}(I)$ for a pure tone is known as well as the filter constant C^{pt} corresponding to the pure tone and all filter constants C_n of contributions to the spectrum of a noise signal, for which we want to predict the rate-intensity function $r^{\text{noise}}(I)$.

Following the model in Section 5.2, we denote the effective sound intensities of the noise signal by J_{EH}^{noise} and J_{PH}^{noise} and the effective sound intensities of the pure-tone signal by J_{EH}^{pt} and J_{PH}^{pt} according to the energy and the pressure hypotheses, respectively. The intensity in the dB SPL scale is defined as

$$I = 20 \log_{10} \frac{\sqrt{\langle A(t)^2 \rangle}}{A_0} \quad (\text{F.1})$$

with $A_0 = 20 \mu\text{Pa}$. For the noise signal, written as a Fourier series

$$A^{\text{noise}}(t) = \sum_n A_n \sin(2\pi f_n t + \phi_n), \quad (\text{F.2})$$

the root-mean-square is obtained as

$$\sqrt{\langle A(t)^2 \rangle} = \sqrt{\frac{1}{2} \sum_n A_n^2}, \quad (\text{F.3})$$

which implies that the intensity is given by

$$I^{\text{noise}} = 20 \log_{10} \frac{\sqrt{\frac{1}{2} \sum_n A_n^2}}{A_0}. \quad (\text{F.4})$$

Intensity changes for this sound signal correspond to scaling all amplitudes A_n with a common factor. The effective sound intensity of the energy hypothesis, J_{EH}^{noise} , see Eq. (5.5), can thus be written as

$$J_{EH}^{\text{noise}}(I^{\text{noise}}) = \frac{1}{2} \sum_n \frac{A_n^2}{C_n^2} = 10^{I^{\text{noise}}/10} \cdot A_0^2 \cdot \frac{\sum_n \frac{A_n^2}{C_n^2}}{\sum_n A_n^2}, \quad (\text{F.5})$$

where the dependence on the intensity I^{noise} is denoted explicitly since the term $\sum \frac{A_n^2}{C_n^2} / \sum A_n^2$ is invariant to intensity changes.

For the effective sound intensity of the pressure hypothesis, J_{PH}^{noise} , see Eq. (5.6), we note that the values of $\tilde{A}(t)$ are distributed according to a Gaussian distribution if the original sound-pressure wave $A(t)$ is a noise signal. In the present case, the amplitudes of $A(t)$ themselves are already distributed according to a Gaussian distribution; quite generally, though, the filtering by the tympanum causes a Gaussian distribution of the

values of $\tilde{A}(t)$ according to the central limit theorem. The variance σ^2 of $\tilde{A}(t)$ is given by

$$\sigma^2 = \frac{1}{2} \sum_n \frac{A_n^2}{C_n^2} = J_{EH}^{\text{noise}}. \quad (\text{F.6})$$

For a Gaussian distribution with standard deviation σ , the mean of the absolute value can be calculated as

$$\langle |\tilde{A}(t)| \rangle = \int_{-\infty}^{\infty} dx \frac{|x|}{\sqrt{2\pi\sigma^2}} \cdot e^{-\frac{x^2}{2\sigma^2}} = 2 \int_0^{\infty} dx \frac{x}{\sqrt{2\pi\sigma^2}} \cdot e^{-\frac{x^2}{2\sigma^2}} = \sqrt{\frac{2}{\pi}} \cdot \sigma, \quad (\text{F.7})$$

and we therefore obtain

$$J_{PH}^{\text{noise}}(I^{\text{noise}}) = \langle |\tilde{A}(t)| \rangle = \sqrt{\frac{2}{\pi}} \cdot J_{EH}^{\text{noise}} = \sqrt{\frac{2}{\pi}} \cdot 10^{I^{\text{noise}}/20} \cdot A_0 \cdot \sqrt{\frac{\sum_n \frac{A_n^2}{C_n^2}}{\sum_n A_n^2}}. \quad (\text{F.8})$$

Equivalently, we find for the pure-tone stimulus $A^{\text{pt}}(t) = A^{\text{pt}} \cdot \sin(2\pi ft)$

$$J_{EH}^{\text{pt}}(I^{\text{pt}}) = \frac{1}{2} \cdot \frac{A^{\text{pt}2}}{C^{\text{pt}2}} = 10^{I^{\text{pt}}/10} \cdot \frac{A_0^2}{C^{\text{pt}2}}, \quad (\text{F.9})$$

$$J_{PH}^{\text{pt}}(I^{\text{pt}}) = \frac{2}{\pi} \cdot \frac{A^{\text{pt}}}{C^{\text{pt}}} = \frac{2\sqrt{2}}{\pi} \cdot 10^{I^{\text{pt}}/20} \cdot \frac{A_0}{C^{\text{pt}}}, \quad (\text{F.10})$$

where C^{pt} denotes the filter constant for the pure tone. These latter relationships can be inverted to yield I^{pt} as a function of J^{pt} :

$$I^{\text{pt}} = 10 \log_{10} \left(\frac{(C^{\text{pt}})^2}{A_0^2} \cdot J_{EH}^{\text{pt}} \right), \quad (\text{F.11})$$

$$I^{\text{pt}} = 20 \log_{10} \left(\frac{\pi}{2\sqrt{2}} \cdot \frac{C^{\text{pt}}}{A_0} \cdot J_{PH}^{\text{pt}} \right). \quad (\text{F.12})$$

Since equal J implies equal firing rate, we can then substitute J^{pt} by $J^{\text{noise}}(I^{\text{noise}})$ to obtain that intensity of the pure tone that leads to the same firing rate as a given intensity I^{noise} of the noise signal:

$$\begin{aligned} r_{EH}^{\text{noise}}(I^{\text{noise}}) &= r_{EH}^{\text{pt}} \left(10 \log_{10} \left(\frac{(C^{\text{pt}})^2}{A_0^2} \cdot J_{EH}^{\text{noise}}(I^{\text{noise}}) \right) \right) \\ &= r_{EH}^{\text{pt}} \left(I^{\text{noise}} + 10 \log_{10} \left(\frac{(C^{\text{pt}})^2}{\sum_n A_n^2} \cdot \frac{\sum_n \frac{A_n^2}{C_n^2}}{\sum_n A_n^2} \right) \right), \end{aligned} \quad (\text{F.13})$$

$$\begin{aligned}
r_{PH}^{\text{noise}}(I^{\text{noise}}) &= r_{PH}^{\text{pt}} \left(20 \log_{10} \left(\frac{\pi}{2\sqrt{2}} \cdot \frac{C^{\text{pt}}}{A_0} \cdot J_{PH}^{\text{noise}}(I^{\text{noise}}) \right) \right) \\
&= r_{PH}^{\text{pt}} \left(I^{\text{noise}} + 10 \log_{10} \left(\frac{\pi}{4} (C^{\text{pt}})^2 \frac{\sum_n \frac{A_n^2}{C_n^2}}{\sum_n A_n^2} \right) \right). \quad (\text{F.14})
\end{aligned}$$

From these formulas, we see that the rate-intensity functions $r^{\text{noise}}(I)$ and $r^{\text{pt}}(I)$ are shifted versions of each other for both hypotheses. The shift ΔI can be directly read out by comparison with Eq. (5.10).

G Shortcut to the Stationary Effective Sound Intensity

According to Eq. (7.3), J_0 results from a convolution of $q(\cdot)$ and $[\xi(\cdot)]^2$. Since the temporal average is proportional to the zeroth Fourier mode, we find from Eq. (7.3)

$$J_0 = \langle J(t) \rangle = \left(\int_0^\infty d\tau q(\tau) \right) \cdot \langle [\xi(t)]^2 \rangle. \quad (\text{G.1})$$

The constant $\int_0^\infty d\tau q(\tau)$ can be absorbed into the nonlinear function $\tilde{g}(J_0)$, and Parseval's theorem yields

$$\langle [\xi(t)]^2 \rangle \propto \int_{-\infty}^\infty df \|\hat{\xi}(f)\|^2, \quad (\text{G.2})$$

where $\hat{\xi}(f)$ is the Fourier transform of $\xi(t)$, $\hat{\xi}(f) = \int dt \xi(t) \exp(-2\pi i f t)$.

According to Eq. (7.1), $\xi(t)$ is the convolution of the filter $l(\tau)$ with the input signal $A(t) = \sum_n A_n \sin(2\pi f_n t)$. Hence, $\hat{\xi}(f)$ has non-zero contributions only at the frequencies f_n , for which we find

$$\|\hat{\xi}(f_n)\|^2 \propto A_n^2 \cdot \|\hat{l}(f_n)\|^2 \quad (\text{G.3})$$

with the Fourier transform $\hat{l}(f)$ of $l(\tau)$. This finally leads to

$$J_0 \propto \sum_n A_n^2 \cdot \|\hat{l}(f_n)\|^2 = \sum_n \frac{A_n^2}{C_n^2} \quad (\text{G.4})$$

where C_n^{-2} has been identified with the squared absolute value of the Fourier component \hat{l}_n of $l(\tau)$. The proportionality factor can also be absorbed into $\tilde{g}(\cdot)$.

BIBLIOGRAPHY

- Adam, J., Myat, A., Le Roux, I., Eddison, M., Henrique, D., Ish-Horowicz, D., and Lewis, J. (1998). Cell fate choices and the expression of Notch, Delta and Serrate homologues in the chick inner ear: Parallels with *Drosophila* sense-organ development. *Development*, 125:4645–4654.
- Adorjan, P., Schwabe, L., Wenning, G., and Obermayer, K. (2002). Rapid adaptation to internal states as a coding strategy in visual cortex? *Neuroreport*, 13:337–342.
- Aguirre, L. A. and Billings, S. A. (1995). Retrieving dynamical invariants from chaotic data using NARMAX models. *Int J Bifurcation and Chaos*, 5:449–474.
- Ahissar, E. and Arieli, A. (2001). Figuring space by time. *Neuron*, 32:185–201.
- Autrum, H. (1940). Über Lautäußerungen und Schallwahrnehmung bei Arthropoden. II. Das Richtungshören von *Locusta* und Versuch einer Hörtheorie für Tympanalorgane vom Locustidentyp. *Z vergl Physiol*, 28:326–352.
- Barlow, R. (1989). *Statistics*. Wiley, New York.
- Benda, J. (2002). *Single Neuron Dynamics – Models Linking Theory and Experiment*. PhD thesis, Humboldt University Berlin.
- Benda, J., Bethge, M., Hennig, M., Pawelzik, K., and Herz, A. V. M. (2001). Spike-frequency adaptation: Phenomenological model and experimental tests. *Neurocomputing*, 38–40:105–110.
- Benda, J. and Herz, A. V. M. (2003). A universal model for spike-frequency adaptation. *Neural Comput*, 15:2523–2564.
- Bermingham, N. A., Hassan, B. A., Price, S. D., Vollrath, M. A., Ben-Arie, N., Eatock, R. A., Bellen, H. J., and Lysakowski, A. (1999). Math1: An essential gene for the generation of inner hair cells. *Science*, 284:1837–1841.
- Berry, M. J. and Meister, M. (1998). Refractoriness and neural precision. *J Neurosci*, 18:2200–2211.
- Best, A. R. and Wilson, D. A. (2004). Coordinate synaptic mechanisms contributing to olfactory cortical adaptation. *J Neurosci*, 24:652–660.

- Bialek, W. and de Ruyter van Steveninck, R. R. (1998). What do motion sensitive visual neurons compute? Unpublished.
- Billings, S. A. (1980). Identification of nonlinear systems – A survey. *IEE Proc*, 127:272–285.
- Billings, S. A. and Chen, S. (1998). The determination of multivariable nonlinear models for dynamic systems. In Leondes, C. T., editor, *Neural Network Systems: Techniques and Applications*, chapter 6, pages 231–278. Academic Press, San Diego.
- Bownds, M. D. and Arshavsky, V. Y. (1995). What are the mechanisms of photoreceptor adaptation? *Behav Brain Sci*, 18:415–424.
- Breckow, J. and Sippel, M. (1985). Mechanics of the tympanal organ of locusts. *J Comp Physiol A*, 157:619–629.
- Brown, D. A. and Adams, P. R. (1980). Muscarinic suppression of a novel voltage-sensitive K⁺ current in a vertebrate neurone. *Nature*, 283:673–676.
- Catton, W. T. (1970). Mechanoreceptor function. *Physiol Rev*, 50:297–318.
- Chapman, K. M., Mosinger, J. L., and Duckrow, R. B. (1979). The role of distributed viscoelastic coupling in sensory adaptation in an insect mechanoreceptor. *J Comp Physiol*, 131:1–12.
- Chichilnisky, E. J. (2001). A simple white noise analysis of neuronal light responses. *Network*, 12:199–213.
- Dallos, P. (1985). Response characteristics of mammalian cochlear hair cells. *J Neurosci*, 5:1591–1608.
- de Boer, E. (1985). Auditory time constants: A paradox? In Michelsen, A., editor, *Time Resolution in Auditory Systems*, pages 141–158. Springer, Berlin.
- Eberl, D. F. (1999). Feeling the vibes: Chordotonal mechanisms in insect hearing. *Curr Opin Neurobiol*, 9:389–393.
- Eguíluz, V. M., Ospeck, M., Choe, Y., Hudspeth, A. J., and Magnasco, M. O. (2000). Essential nonlinearities in hearing. *Phys Rev Lett*, 84:5232–5235.
- Ermentrout, B. (1996). Type I membranes, phase resetting curves, and synchrony. *Neural Comput*, 8:979–1001.
- Estévez, O. and Spekreijse, H. (1982). The “silent substitution” method in visual research. *Vis Res*, 22:681–691.
- Evans, E. F. (1975). Cochlear nerve and cochlear nucleus. In Keidel, W. D. and Neff, W. D., editors, *Handbook of Sensory Physiology: Auditory Systems*, volume 5.2, pages 1–108. Springer, Berlin.

- Eyzaguirre, C. and Kuffler, S. W. (1955). Processes of excitation in the dendrites and in the soma of single isolated sensory nerve cells of the lobster and crayfish. *J Gen Physiol*, 39:87–119.
- Fettiplace, R. and Fuchs, P. A. (1999). Mechanics of hair cell tuning. *Annu Rev Physiol*, 61:809–834.
- Fleidervish, I. A., Friedman, A., and Gutnick, M. J. (1996). Slow inactivation of Na⁺ current and slow cumulative spike adaptation in mouse and guinea-pig neocortical neurones in slices. *J Physiol (Lond)*, 493:83–97.
- Florentine, M., Fastl, H., and Buus, S. (1988). Temporal integration in normal hearing, cochlear impairment, and impairment simulated by masking. *J Acoust Soc Am*, 84:195–203.
- French, A. S. (1984a). Action potential adaptation in the cockroach tactile spine. *J Comp Physiol A*, 155:803–812.
- French, A. S. (1984b). The receptor potential and adaptation in the cockroach tactile spine. *J Neurosci*, 4:2063–2068.
- French, A. S. (1988). Transduction mechanisms of mechanosensilla. *Annu Rev Entomol*, 33:39–58.
- French, A. S. (1992). Mechanotransduction. *Annu Rev Physiol*, 54:135–152.
- French, A. S., Korenberg, M. J., Jarvilehto, M., Kouvalainen, E., Juusola, M., and Weckstrom, M. (1993). The dynamic nonlinear behavior of fly photoreceptors evoked by a wide range of light intensities. *Biophys J*, 65:832–839.
- Friston, K. J., Penny, W., Phillips, C., Kiebel, S., Hinton, G., and Ashburner, J. (2002). Classical and Bayesian inference in neuroimaging: Theory. *Neuroimage*, 16:465–483.
- Fritsch, B., Beisel, K. W., and Bermingham, N. A. (2000). Developmental evolutionary biology of the vertebrate ear: Conserving mechanoelectric transduction and developmental pathways in diverging morphologies. *Neuroreport*, 11:R35–R44.
- Garner, W. R. (1947). The effect of frequency spectrum on temporal integration of energy in the ear. *J Acoust Soc Am*, 19:808–814.
- Geisler, C. D. (1998). *From Sound to Synapse: Physiology of the Mammalian Ear*. Oxford University Press, New York.
- Gerstner, W. and Kistler, W. (2002). *Spiking Neuron Models: Single Neurons, Populations, Plasticity*. Cambridge University Press, Cambridge.
- Gillespie, P. G. (1995). Molecular machinery of auditory and vestibular transduction. *Curr Opin Neurobiol*, 5:449–455.

- Gillespie, P. G. and Walker, R. G. (2001). Molecular basis of mechanosensory transduction. *Nature*, 413:194–202.
- Gollisch, T. and Herz, A. V. M. (2003a). Analyzing mechanosensory transduction by identifying invariant directions in stimulus space. *Neurocomputing*, 52–54:525–530.
- Gollisch, T. and Herz, A. V. M. (2003b). Uncovering the functional dynamics of biological signal-transduction modules. *Proc Idea-Finding Symposium, Frankfurt Institute for Advanced Studies*, pages 75–84.
- Gollisch, T. and Herz, A. V. M. (2003c). The “What” and “How” of temporal integration in an insect auditory system. *Proc Göttingen Neurobiol Conf*, page 395.
- Gollisch, T. and Herz, A. V. M. (2004a). Identification of sensory transduction chains *in vivo*. *Submitted for publication*.
- Gollisch, T. and Herz, A. V. M. (2004b). Input-driven components of spike-frequency adaptation can be unmasked *in vivo*. *J Neurosci*, in press.
- Gollisch, T., Schütze, H., Benda, J., and Herz, A. V. M. (2002). Energy integration describes sound-intensity coding in an insect auditory system. *J Neurosci*, 22:10434–10448.
- Göpfert, M. C. and Robert, D. (2001). Active auditory mechanics in mosquitoes. *Proc R Soc Lond B*, 268:333–339.
- Gray, E. G. (1960). The fine structure of the insect ear. *Philos Trans R Soc London [B]*, 243:75–94.
- Grothe, B. and Klump, G. M. (2000). Temporal processing in sensory systems. *Curr Opin Neurobiol*, 10:467–473.
- Hahnloser, R. H., Kozhevnikov, A. A., and Fee, M. S. (2002). An ultra-sparse code underlies the generation of neural sequences in a songbird. *Nature*, 419:65–70.
- Hardie, R. C. and Raghu, P. (2001). Visual transduction in *Drosophila*. *Nature*, 413:186–193.
- Hartley, H. (1958). Maximum likelihood estimation from incomplete data. *Biometrics*, 14:174–194.
- Hartwell, L. H., Hopfield, J. J., Leibler, S., and Murray, A. W. (1999). From molecular to modular cell biology. *Nature*, 402:C47–C52.
- Heil, P. and Neubauer, H. (2001). Temporal integration of sound pressure determines thresholds of auditory-nerve fibers. *J Neurosci*, 21:7404–7415.
- Heil, P. and Neubauer, H. (2003). A unifying basis of auditory thresholds based on temporal summation. *Proc Natl Acad Sci USA*, 100:6151–6156.

- Herz, A. V. M. (2004). How is time represented in the brain? In van Hemmen, J. L. and Sejnowski, T. J., editors, *Problems in Systems Neuroscience*. Oxford University Press, Oxford. In press.
- Hill, K. G. (1983). The physiology of locust auditory receptors. I. Discrete depolarizations of receptor cells. *J Comp Physiol A*, 152:475–482.
- Hodgkin, A. (1948). The local electric changes associated with repetitive action in a non-medullated axon. *J Physiol*, 107:165–181.
- Holt, J. R. and Corey, D. P. (2000). Two mechanisms for transducer adaptation in vertebrate hair cells. *Proc Natl Acad Sci USA*, 97:11730–11735.
- Hopfield, J. J. (1995). Pattern recognition computation using action potential timing for stimulus representation. *Nature*, 376:33–36.
- Hopfield, J. J. (1996). Transforming neural computations and representing time. *Proc Natl Acad Sci USA*, 93:15440–15444.
- Hopfield, J. J. and Brody, C. D. (2001). What is a moment? Transient synchrony as a collective mechanism for spatiotemporal integration. *Proc Natl Acad Sci USA*, 98:1282–1287.
- Hoppensteadt, F. C. (1997). *An Introduction to the Mathematics of Neurons, Modeling in the Frequency Domain*. Cambridge University Press, Cambridge, 2nd edition.
- Horch, K. (1991). Coding of vibrotactile stimulus frequency by Pacinian corpuscle afferents. *J Acoust Soc Am*, 89:2827–2836.
- Hubbard, S. J. (1958). A study of rapid mechanical events in a mechanoreceptor. *J Physiol (Lond)*, 141:198–218.
- Hudspeth, A. J. (1985). The cellular basis of hearing: The biophysics of hair cells. *Science*, 230:745–752.
- Hudspeth, A. J. (1989). How the ear's works work. *Nature*, 341:397–404.
- Hudspeth, A. J., Choe, Y., Mehta, A. D., and Martin, P. (2000). Putting ion channels to work: Mechanoelectric transduction, adaptation, and amplification by hair cells. *Proc Natl Acad Sci USA*, 97:11765–11772.
- Hudspeth, A. J. and Logothetis, N. K. (2000). Sensory systems. *Curr Opin Neurobiol*, 10:631–641.
- Hunter, I. W. and Korenberg, M. J. (1986). The identification of nonlinear biological systems: Wiener and Hammerstein cascade models. *Biol Cybern*, 55:135–144.
- Izhikevich, E. M. (2000). Neural excitability, spiking, and bursting. *Int J Bifurcation and Chaos*, 10:1171–1266.

- Jacobs, K. and Lakes-Harlan, R. (1999). Axonal degeneration within the tympanal nerve of *Schistocerca gregaria*. *Cell Tissue Res*, 298:167–178.
- Jacobs, K., Otte, B., and Lakes-Harlan, R. (1999). Tympanal receptor cells of *Schistocerca gregaria*: Correlation of soma positions and dendrite attachment sites, central projections and physiologies. *J Exp Zool*, 283:270–285.
- Jameson, D. and Hurvich, L. M., editors (1972). *Handbook of Sensory Physiology: Visual Psychophysics*, volume 7.4. Springer, Berlin.
- Jensen, O. and Lisman, J. E. (2000). Position reconstruction from an ensemble of hippocampal place cells: Contribution of theta phase coding. *J Neurophysiol*, 83:2602–2609.
- Kandel, E. R., Schwartz, J. H., and Jessell, T. M. (2000). *Principles of Neural Science*. McGraw-Hill, New York, 4th edition.
- Knudsen, E. I. (1980). Sound localization in birds. In Popper, A. N. and Fay, R. R., editors, *Comparative Studies of Hearing in Vertebrates*, pages 289–322. Springer, New York.
- Koch, C. (1999). *Biophysics of Computation*. Oxford University Press, New York.
- Köppl, C., Manley, G. A., and Konishi, M. (2000). Auditory processing in birds. *Curr Opin Neurobiol*, 10:474–481.
- Korenberg, M. J. (1973a). Cross-correlation analysis of neural cascades. *Proc 10th Rocky Mountain Biol Eng Symp*, pages 47–51.
- Korenberg, M. J. (1973b). Identification of biological cascades of linear and static nonlinear systems. *Proc Midwest Symp Circuit Theory*, 18.2:1–9.
- Korenberg, M. J. and Hunter, I. W. (1986). The identification of nonlinear biological systems: LNL cascade models. *Biol Cybern*, 55:125–134.
- Kössl, M. and Boyan, G. S. (1998a). Acoustic distortion products from the ear of a grasshopper. *J Acoust Soc Am*, 104:326–335.
- Kössl, M. and Boyan, G. S. (1998b). Otoacoustic emissions from a nonvertebrate ear. *Naturwissenschaften*, 85:124–127.
- Lamb, T. D. and Pugh, E. N. (1992). A quantitative account of the activation steps involved in phototransduction in amphibian photoreceptors. *J Physiol*, 449:719–758.
- Lang, F. (2000). Acoustic communication distances of a gomphocerine grasshopper. *Bioacoustics*, 10:233–258.
- Loewenstein, W. R. (1971). Mechano-electric transduction in the Pacinian corpuscle. Initiation of sensory impulses in mechanoreceptors. In Loewenstein, W. R., editor, *Handbook of Sensory Physiology*, volume 1, pages 269–290. Springer, Berlin.

- Loewenstein, W. R. and Mendelson, M. (1965). Components of receptor adaptation in a Pacinian corpuscle. *J Physiol (Lond)*, 177:377–397.
- Maass, W., Natschläger, T., and Markram, H. (2002). Real-time computing without stable states: A new framework for neural computation based on perturbations. *Neural Comput*, 14:2531–2560.
- Machens, C. K., Gollisch, T., Kolesnikova, O., and Herz, A. V. M. (2004). Optimal stimulus ensembles for efficient coding in sensory neurons. *Preprint*.
- Machens, C. K., Schütze, H., Franz, A., Kolesnikova, O., Stemmler, M. B., Ronacher, B., and Herz, A. V. M. (2003). Single auditory neurons rapidly discriminate conspecific communication signals. *Nat Neurosci*, 6:341–342.
- Machens, C. K., Stemmler, M. B., Prinz, P., Krahe, R., Ronacher, B., and Herz, A. V. M. (2001). Representation of acoustic communication signals by insect auditory receptor neurons. *J Neurosci*, 21:3215–3227.
- Madison, D. V. and Nicoll, R. A. (1984). Control of the repetitive discharge of rat CA 1 pyramidal neurones in vitro. *J Physiol*, 354:319–331.
- Markin, V. S. and Hudspeth, A. J. (1995). Gating-spring models of mechano-electrical transduction by hair cells of the internal ear. *Annu Rev Biophys Struct*, 24:59–83.
- Marmarelis, P. Z. and Marmarelis, V. Z. (1978). *Analysis of Physiological Systems: The White-Noise Approach*. Plenum Press, New York.
- Marmarelis, P. Z. and Naka, K. (1972). White-noise analysis of a neuron chain: An application of the Wiener theory. *Science*, 175:1276–1278.
- Martin, P. and Hudspeth, A. J. (1999). Active hair-bundle movements can amplify a hair cell's response to oscillatory mechanical stimuli. *Proc Natl Acad Sci USA*, 96:14306–14311.
- Martinac, B. (2001). Mechanosensitive channels in prokaryotes. *Cell Physiol Biochem*, 11:61–76.
- Martinac, B. and Kloda, A. (2003). Evolutionary origins of mechanosensitive ion channels. *Prog Biophys Mol Biol*, 82:11–24.
- Mason, A. C., Oshinsky, M. L., and Hoy, R. R. (2001). Hyperacute directional hearing in a microscale auditory system. *Nature*, 410:686–690.
- Matthews, B. H. C. (1931). The response of a single end organ. *J Physiol (Lond)*, 71:64–110.
- Matthews, B. H. C. (1933). Nerve endings in mammalian muscle. *J Physiol (Lond)*, 78:1–53.
- Matthews, P. B. C. and Stein, R. B. (1969). The sensitivity of muscle spindle afferents to sinusoidal stretching. *J Physiol*, 200:723–743.

- McEwen, B. S. and Wingfield, J. C. (2003). The concept of allostasis in biology and biomedicine. *Horm Behav*, 43:2–15.
- Meyer, J. and Elsner, N. (1996). How well are frequency sensitivities of grasshopper ears tuned to species-specific song spectra? *J Exp Biol*, 199:1631–1642.
- Michelsen, A. (1971a). The physiology of the locust ear. I. Frequency sensitivity of single cells in the isolated ear. *Z vergl Physiologie*, 71:49–62.
- Michelsen, A. (1971b). The physiology of the locust ear. II. Frequency discrimination based upon resonance in the tympanum. *Z vergl Physiologie*, 71:63–101.
- Michelsen, A. (1971c). The physiology of the locust ear. III. Acoustic properties of the intact ear. *Z vergl Physiologie*, 71:102–128.
- Michelsen, A. (1979). Insect ears as mechanical systems. *Am Sci*, 67:696–706.
- Michelsen, A. (1994). Directional hearing in crickets and other small animals. In Schildberger, K. and Elsner, N., editors, *Neural Basis of Behavioural Adaptations*, pages 195–207. Fischer, Stuttgart.
- Michelsen, A. and Rohrseitz, K. (1995). Directional sound processing and interaural sound transmission in a small and a large grasshopper. *J Exp Biol*, 198:1817–1827.
- Narusuye, K., Kawai, F., and Miyachi, E. (2003). Spike encoding of olfactory receptor cells. *Neurosci Res*, 46:407–413.
- Neal, R. M. and Hinton, G. E. (1998). A view of the EM algorithm that justifies incremental, sparse, and other variants. In Jordan, M. I., editor, *Learning in Graphical Models*, pages 355–368. Kluwer Academic Press, Dordrecht.
- Neuweiler, G. and Schmidt, S. (1993). Audition in echolocating bats. *Curr Opin Neurobiol*, 3:563–569.
- Nurse, P. (2003). Systems biology: Understanding cells. *Nature*, 424:883.
- Oshinsky, M. L. and Hoy, R. R. (2002). Physiology of the auditory afferents in an acoustic parasitoid fly. *J Neurosci*, 22:7254–7263.
- Plomp, R. and Bouman, M. A. (1959). Relation between hearing threshold and duration for tone pulses. *J Acoust Soc Am*, 31:749–758.
- Press, W. H., Teukolsky, S. A., Vetterling, W. T., and Flannery, B. P. (1992). *Numerical Recipes*. Cambridge University Press, Cambridge.
- Prinz, P. and Ronacher, B. (2002). Temporal modulation transfer functions in auditory receptor fibres of the locust (*Locusta migratoria* L.). *J Comp Physiol A*, 188:577–587.
- Proske, U. and Gregory, J. E. (2002). Signalling properties of muscle spindles and tendon organs. *Adv Exp Med Biol*, 508:5–12.

- Purali, N. and Rydqvist, B. (1998). Action potential and sodium current in the slowly and rapidly adapting stretch receptor neurons of the crayfish (*Astacus astacus*). *J Neurophysiol*, 80:2121–2132.
- Ricci, A. J., Wu, Y.-C., and Fettiplace, R. (1998). The endogenous calcium buffer and the time course of transducer adaptation in auditory hair cells. *J Neurosci*, 18:8261–8277.
- Rieke, F., Warland, D., de Ruyter van Steveninck, R. R., and Bialek, W. (1997). *Spikes: Exploring the Neural Code*. MIT Press, Cambridge.
- Rinzel, J. and Ermentrout, B. (1998). Analysis of neural excitability and oscillations. In Koch, C. and Segev, I., editors, *Methods in Neural Modeling: From Ions to Networks*, pages 251–292. MIT Press, Cambridge, 2nd edition.
- Robeles, L. and Ruggero, M. A. (2001). Mechanics of the mammalian cochlea. *Physiol Rev*, 81:1305–1352.
- Robert, D. and Göpfert, M. C. (2002). Novel schemes for hearing and orientation in insects. *Curr Opin Neurobiol*, 12:715–720.
- Römer, H. (1976). Die Informationsverarbeitung tympanaler Rezeptorelemente von *Locusta migratoria* (Acrididae, Orthoptera). *J Comp Physiol*, 109:101–122.
- Römer, H. (1985). Anatomical representation of frequency and intensity in the auditory system of Orthoptera. In Kalmring, K. and Elsner, N., editors, *Acoustic and Vibrational Communication in Insects*, pages 25–33. Paul Parey, Berlin.
- Ruggero, M. A., Narayan, S., Temchin, A. N., and Recio, A. (2000). Mechanical bases of frequency tuning and neural excitation at the base of the cochlea: Comparison of basilar-membrane vibrations and auditory-nerve-fiber responses in chinchilla. *Proc Natl Acad Sci USA*, 97:11744–11750.
- Russell, I. J. and Sellick, P. M. (1983). Low-frequency characteristics of intracellularly recorded receptor potentials in guinea-pig cochlear hair cells. *J Physiol*, 338:179–206.
- Sah, P. and Davies, P. (2000). Calcium-activated potassium currents in mammalian neurons. *Clin Exp Pharmacol Physiol*, 27:657–663.
- Schaette, R., Gollisch, T., and Herz, A. V. M. (2004). Spike-train variability in auditory neurons in vivo: Dynamic responses follow predictions from constant stimuli. *Submitted for publication*.
- Schiolten, P., Larsen, O. N., and Michelsen, A. (1981). Mechanical time resolution in some insect ears. *J Comp Physiol*, 143:289–295.
- Schwabe, J. (1906). Beiträge zur Morphologie und Histologie der tympanalen Sinnesapparate der Orthopteren. *Zoologica*, 50:1–154.

- Schwabe, L. and Obermayer, K. (2003). Modeling the adaptive visual system: A survey of principled approaches. *Neural Netw*, 16:1353–1371.
- Schwartz, O., Chichilnisky, E. J., and Simoncelli, E. P. (2002). Characterizing neural gain control using spike triggered covariance. In Dietterich, T. G., Becker, S., and Ghahramani, Z., editors, *Advances in Neural Information Processing Systems*, volume 14, pages 269–276. MIT Press, Cambridge.
- Sharpee, T., Rust, N. C., and Bialek, W. (2004). Analyzing neural responses to natural signals: Maximally informative dimensions. *Neural Comput*, 16:223–250.
- Shriki, O., Hansel, D., and Sompolinsky, H. (2003). Rate models for conductance-based cortical neuronal networks. *Neural Comput*, 15:1809–1841.
- Spekreijse, H. (1969). Rectification in the goldfish retina: Analysis by sinusoidal and auxiliary stimulation. *Vision Res*, 9:1461–1472.
- Spekreijse, H. and Oosting, H. (1970). Linearizing: A method for analysing and synthesizing nonlinear systems. *Kybernetik*, 7:22–31.
- Stephen, R. O. and Bennet-Clark, H. C. (1982). The anatomical and mechanical basis of stimulation and frequency analysis in the locust ear. *J Exp Biol*, 99:279–314.
- Storm, J. F. (1990). Potassium currents in hippocampal pyramidal cells. *Prog Brain Res*, 83:161–187.
- Stumpner, A. and Ronacher, B. (1991). Auditory interneurons in the metathoracic ganglion of the grasshopper *Chorthippus biguttulus*. I. Morphological and physiological characterization. *J Exp Biol*, 158:391–410.
- Stumpner, A., Ronacher, B., and von Helversen, O. (1991). Auditory interneurons in the metathoracic ganglion of the grasshopper *Chorthippus biguttulus*. II. Processing of temporal patterns of the song of the male. *J Exp Biol*, 158:411–430.
- Stumpner, A. and von Helversen, D. (2001). Evolution and function of auditory systems in insects. *Naturwissenschaften*, 88:159–170.
- Suga, N. (1960). Peripheral mechanism of hearing in locust. *Jpn J Physiol*, 10:533–546.
- Thurm, U. (1996). Mechanosensorik. In Dudel, J., Menzel, R., and Schmidt, R. F., editors, *Neurowissenschaft: Vom Molekül zur Kognition*, chapter 15, pages 331–351. Springer, Berlin.
- Torkkeli, P. H., Sekizawa, S., and French, A. S. (2001). Inactivation of voltage-activated Na(+) currents contributes to different adaptation properties of paired mechanosensory neurons. *J Neurophysiol*, 85:1595–602.
- Tougaard, J. (1996). Energy detection and temporal integration in the noctuid A1 auditory receptor. *J Comp Physiol A*, 178:669–677.

- Tougaard, J. (1998). Detection of short pure-tone stimuli in the noctuid ear: What are temporal integration and integration time all about? *J Comp Physiol A*, 183:563–572.
- Touryan, J., Lau, B., and Dan, Y. (2002). Isolation of relevant visual features from random stimuli for cortical complex cells. *J Neurosci*, 15:10811–10818.
- Van Rullen, R. and Thorpe, S. J. (2001). Rate coding versus temporal order coding: What the retinal ganglion cells tell the visual cortex. *Neural Comput*, 13:1255–1283.
- Vergara, C., Latorre, R., Marrion, N. V., and Adelman, J. P. (1998). Calcium-activated potassium channels. *Curr Opin Neurobiol*, 8:321–329.
- Vilin, Y. Y. and Ruben, P. C. (2001). Slow inactivation in voltage-gated sodium channels: Molecular substrates and contributions to channelopathies. *Cell Biochem Biophys*, 35:171–190.
- von Helversen, D. (1972). Gesang des Männchens und Lautschema des Weibchens bei der Feldheuschrecke *Chorthippus biguttulus*. *J Comp Physiol*, 81:381–422.
- von Helversen, O. and von Helversen, D. (1994). Forces driving coevolution of song and song recognition in grasshoppers. In Schildberger, K. and Elsner, N., editors, *Neural Basis of Behavioural Adaptations*, pages 253–284. Fischer, Stuttgart.
- Walker, R. G., Willingham, A. T., and Zuker, C. S. (2000). A *Drosophila* mechanosensory transduction channel. *Science*, 287:2229–2234.
- Watzl, S., Rokem, A., Gollisch, T., and Herz, A. V. M. (2003). Coding capacities of auditory receptor cells under different stimulus conditions. *Proc Göttingen Neurobiol Conf*, page 396.
- Zwislocki, J. J. (1965). Analysis of some auditory characteristics. In Luce, R. D., Bush, R. R., and Galanter, E., editors, *Handbook of Mathematical Psychology*, volume 3, chapter 15, pages 1–97. Wiley, New York.
- Zwislocki, J. J. (1991). What is the cochlear place code for pitch? *Acta Otolaryngol*, 111:256–262.

Deutschsprachige Zusammenfassung

Wir erfassen die Struktur unserer Umwelt mit Hilfe unserer Sinne. Die Verarbeitung von Sinnesreize, wie etwa Licht, Geräusche, Düfte etc., findet mit Hilfe elektrischer Signale im Nervensystem statt. Dazu muss zunächst der externe Reiz in ein internes elektrisches Aktivitätsmuster umgewandelt werden. Diese Transduktion geschieht in spezialisierten Rezeptorzellen, die die Schnittstellen zwischen Umwelt und Nervensystem darstellen. Dabei ist eine Kette von biophysikalischen Prozessen involviert, die das hereinkommende Signal sukzessive transformieren. So wird im Allgemeinen beim Hören zunächst der Schall von einer resonanzfähigen Membran, dem Trommelfell, aufgefangen. Die Vibrationen des Trommelfells werden mechanisch weitergeleitet und führen schließlich zu Deformationen an auditorischen Sinneszellen im Ohr. In diesen öffnen sich dadurch mechanosensitive Ionenkanäle, und die durch die Zellmembran strömenden elektrischen Ladungsträger führen zu einer elektrischen Depolarisation der Zelle. Anschließend kehrt das elektrische Potential wieder zu seinem Ausgangswert zurück, falls kein weiterer Reiz hinzukommt; übersteigt die Depolarisation jedoch eine bestimmte Stärke, führt das Öffnen spannungsabhängiger Ionenkanäle zu einem stereotyper Spannungspuls, einem Aktionspotential.

Ziel dieser Arbeit ist die quantitative Beschreibung der Vorgänge, die zur Signaltransduktion in auditorischen Rezeptorzellen führen. Der hierzu gewählte Ansatz zielt auf die Identifizierung und Charakterisierung der funktionalen Grundbausteine ("Module") in der oben beschriebenen Transduktionskette ab. Als experimentelles Modellsystem wird die auditorische Peripherie von Heuschrecken verwendet. Die Untersuchung der auditorischen Transduktion ist im Allgemeinen erschwert durch die Verletzlichkeit der mechanischen Strukturen im Ohr. Die im Rahmen dieser Doktorarbeit vorgestellten Experimente basieren daher ausschließlich auf elektrophysiologischen Ableitungen von einzelnen Nervenfasern im auditorischen Nerv der Tiere. In diesem Nerv werden die Aktionspotentiale vom Ohr zur Verarbeitung in zentraleren Bereichen des Nervensystems weitergeleitet, sodass der Nerv zugänglich ist, ohne dass im Ohr selbst eingegriffen werden müsste. Die hier gemessenen Aktionspotentiale stellen die "Ausgabe"-Seite der Signaltransduktionskette dar. Um von diesen Signalen auf die einzelnen Verarbeitungsschritte in den Sinneszellen zurückschließen zu können, sind neuartige Methoden der Datengewinnung und -analyse nötig, deren Entwicklung ein zentraler Aspekt dieser Arbeit ist.

Zunächst werden die Grundlagen der auditorischen Transduktionen und fundamentale Fragen der Prozessierung akustischer Signale in Kapitel 1 vorgestellt. Neben dem oben bereits erwähnten sequentiellen Charakter der Transduktionskette stehen dabei die zeitliche Struktur der akustischen Signale und die durch die Kodierung hervorgerufene Reduktion der Signaldimension im Mittelpunkt. Viele akustische Signale enthalten relevante Informationen auf unterschiedlichen Zeitskalen, von wenigen Mikrosekunden bis zu einigen Sekunden. Eine wichtige Frage ist insbesondere, wie die Rezeptorzellen das hohe Auflösungsvermögen im Bereich unter einer Millisekunde erreichen, zumal typische Membran-Zeitkonstanten von Neuronen im Bereich von einigen Millisekunden liegen. Weiterhin führt die große Vielfalt von akustischen Signalen dazu, dass einzelne Neurone

in ihren Antworten unterschiedliche Reizaspekte “zusammenfassen”, zum Beispiel indem sie über eine gewisse Reizdauer integrieren. Diese dimensionsreduzierende Signalintegration führt dazu, dass unterschiedliche Reize auf gleiche Weise kodiert werden.

Die für die Arbeit relevanten biologischen und methodologischen Hintergrundinformationen werden in den Kapiteln 2 und 3 vorgestellt. Zunächst werden die Kenntnisse einiger Arbeiten über die Anatomie und Physiologie des Hörgans (Tympanalorgan) der Heuschrecke zusammengefasst. Dabei werden auch neue, eigene Untersuchungen zum zeitlichen Auflösungsvermögen der Rezeptorzellen und zur Phasenankopplung der Aktionspotentiale an die Schallschwingung vorgestellt. Anschließend folgt in Kapitel 3 ein kurzer Überblick über Modellansätze und Analysemethoden, die im Rahmen der Theorie nichtlinearer Systeme verwendet werden. Einen Schwerpunkt bilden dabei die Eigenschaften von Kaskadenmodellen, die die Grundlage für die in dieser Arbeit vorgestellten Modelle darstellen. Die Grundbausteine dieser Modellklasse sind lineare zeitliche Filter und nichtlineare statische Transformationen, durch deren Verknüpfungen Kaskaden beliebiger Komplexität erzeugt werden können.

Die methodischen Grundlagen für die anschließenden experimentellen Untersuchungen werden in Kapitel 4 gelegt. Die hier vorgestellten Ansätze basieren auf der experimentellen Bestimmung unterschiedlicher Reize, die jeweils die gleiche neuronale Aktivität hervorrufen. Diese “iso-response sets” (IRS) genannten Reizkombinationen können zur Bestimmung von in der Transduktionskette vorkommenden nichtlinearen Transformationen verwendet werden. Weiterhin können im Rahmen einfacher Kaskadenmodelle die Komponenten einzelner linearer Filter durch quantitative Vergleiche innerhalb des IRS bestimmt werden (“CIRS”-Methode). Schließlich wird gezeigt, dass durch schnelles Wechseln zwischen zwei Reizen, die die gleiche Antwort liefern, Prozesse unterschieden werden können, die durch die Eingangssignale, bzw. die Ausgangssignale der Transduktionskette gesteuert werden (“DIRS”-Methode).

Anschließend werden in den Kapiteln 5 und 6 spektrale und zeitliche Integration in Rezeptorzellen von Heuschrecken experimentell untersucht. Die Untersuchung der spektralen Integration stellt die Frage, wie unterschiedliche Komponenten des Frequenzspektrums eines stationären akustischen Signals kombiniert werden und so die neuronale Aktivität, gemessen als Feuerrate, bestimmen. Die Messung von unterschiedlichen Tonkombinationen, die jeweils die gleiche Feuerrate einer Rezeptorzelle hervorrufen, zeigt, dass die Energie der Trommelfellvibrationen die eigentliche Signalgröße ist, die in den Feuerraten der Rezeptorzellen signalisiert wird. Die sich hieraus ergebende Modellvorstellung wird in den Experimenten zur zeitlichen Integration in Kapitel 6 erweitert. Hier wird die Frage gestellt, wie nacheinander kommende Signalkomponenten kombiniert werden, um gemeinsam ein Aktionspotential hervorzurufen. Dies wird experimentell untersucht, indem unterschiedliche Kombinationen von kurzen akustischen Klicks bestimmt werden, die zur gleichen Wahrscheinlichkeit für das Auftreten eines Aktionspotentials führen. Aus den Ergebnissen ergibt sich ein vierstufiges Kaskadenmodell. Der erste und zweite Schritt dieser Kaskade sind lineare Filter, die die Schwingung des Trommelfells und den Aufbau der elektrischen Spannung in der Zelle beschreiben. Der zweite Modellschritt ist eine nichtlineare Transformation, die durch die mechanosensorische Transduktion hervorgerufen wird. Diese Transformation lässt sich als einfache Quadrierung beschreiben, was der Berechnung der Schwingungsenergie entspricht. Mit einer weite-

ren nichtlinearen Transformation wird schließlich die Erzeugung von Aktionspotentialen erfasst. Die zeitlichen Verläufe der beiden linearen Filter können mit Hilfe der CIRS-Methode mit einer Genauigkeit von wenigen zehn Mikrosekunden bestimmt werden, und es stellt sich heraus, dass entsprechenden Verarbeitungsschritte auf Zeitskalen deutlich unter einer Millisekunde ablaufen.

Die aus den Untersuchungen zu spektraler und zeitlicher Integration resultierenden speziellen mathematischen Modelle werden in Kapitel 7 mit einem allgemeinen Kaskadenmodell in Verbindung gebracht. Dieses wird zunächst mathematisch beschrieben und anschließend verwendet, um die beiden speziellen Modellversionen formal herzuleiten. Daraus resultieren explizite Relationen zwischen den in den jeweiligen Modellen verwendeten Parametern. Bei den Herleitungen wird ein besonderes Augenmerk auf die nötigen mathematischen Annahmen und Näherungen gelegt, die Auskunft geben über Anwendbarkeit und Einschränkungen der Modellversionen.

In Kapitel 8 wenden wir uns der Untersuchung der Feuerraten-Adaptation in den Rezeptorzellen zu. Feuerraten-Adaptation ist die langsame, d.h. über mehrere 100 ms wirkende Reduzierung der neuronalen Aktivität trotz gleichbleibender Reizstärke. Insbesondere stellen wir hier die Frage nach dem Auslöser für Adaptationseffekte und unterscheiden zwischen Adaptationskomponenten, die durch das Eingangssignal (d.h. den Schallreiz selbst) bzw. das Ausgangssignal (die Aktionspotentiale) des Neurons hervorgerufen werden. Die experimentelle Untersuchung basiert auf der DIRS-Methode, wobei zunächst zwei unterschiedliche akustische Signale bestimmt werden, die die gleiche Feuerrate hervorrufen. Anschließend wird untersucht, wie die Feuerrate auf einen plötzlichen Umschalten von einem auf das andere Signal reagiert. Damit wird nachgewiesen, dass zumindest ein Teil der Feuerraten-Adaptation auf Prozesse, die direkt vom Eingangssignal abhängen, zurückzuführen ist. Aufgrund der bereits gewonnenen Erkenntnisse über die Transduktionskette lässt dies darauf schließen, dass die mechanische Struktur des Trommelfells für dieses Adaptationsphänomen verantwortlich ist.

Zusammenfassend erhalten wir damit eine mathematisch einfache und dennoch präzise Beschreibung der funktionalen Module, aus denen sich die auditorische Transduktionskette in Rezeptorzellen von Heuschrecken zusammensetzt. Die gefundenen schnellen Integrationsprozesse stimmen gut überein mit aus anderen Arbeiten bekannten zeitlich präzisen Aktivitätsmustern und hohen Informationsraten dieser Neurone. Das für die Beschreibung der Signalverarbeitung in den Zellen verwendete Modell eignet sich zudem für Erweiterungen durch Modellkomponenten, die die Refraktärzeit der Zellen und bestimmte Adaptationsprozesse erfassen. Die in dieser Arbeit vorgestellten Methoden stellen ein neues, allgemeines Werkzeug zur systemtheoretischen Analyse dar, das auch für etliche andere biologische Signalverarbeitungsketten anwendbar ist. Einige Erweiterungsmöglichkeiten der Methodik werden im abschließenden Ausblick der Arbeit diskutiert.

Lebenslauf

geboren am 18. 9. 1973 in Bad Oeynhausen

- 1980–1984 Grundschule Halle-Hörste
- 1984–1991 Kreisgymnasium Halle in Westfalen
- 1991–1992 Austauschschüler an der Amanda Clearcreek High School,
Lancaster, Ohio, USA
- 1992–1994 Städtisches Gymnasium Gütersloh
- 1994 Abitur
- 1994–1995 Zivildienst beim Paritätischen Wohlfahrtsverband, Bielefeld
- 1995–2000 Physikstudium an der Universität Heidelberg
- 1997 Vordiplom
- 1997 3-monatiges Forschungspraktikum am
California Institute of Technology, Pasadena, USA
- 1998 3-monatiges Forschungspraktikum am
Weizmann Institute of Science, Rehovot, Israel
- 2000 Diplom in Physik
- 2000 3-monatiger Forschungsaufenthalt an der
Hebrew University, Jerusalem, Israel
- seit 10/2000 Promotion bei Prof. Dr. Andreas Herz
- 2001 Sommerschule “Methods in Computational Neuroscience” am
Marine Biological Laboratory, Woods Hole, USA
- 2002 6-wöchiger Forschungsaufenthalt am
Laboratoire de Neurophysique, Paris, Frankreich
- 2002 “EU Advanced Course in Computational Neuroscience”,
Obidos, Portugal
- 2003 Sommerschule “Methods and Models in Neurophysics”,
Les Houches, Frankreich

Berlin, 19. März 2004

Veröffentlichungen

Artikel in Fachzeitschriften

bereits erschienen

- Gollisch, T. and Wetterich, C. (2001). Unique translation between Hamiltonian operators and functional integrals. *Phys Rev Lett*, 86:1–5.
- Gollisch, T. and Wetterich, C. (2002). Equation of state for helium-4 from microphysics. *Phys Rev B*, 65:134506.
- Gollisch, T., Schütze, H., Benda, J., and Herz, A. V. M. (2002). Energy integration describes sound-intensity coding in an insect auditory system. *J Neurosci* 22:10434–10448.
- Gollisch, T. and Herz, A. V. M. (2003). Analyzing mechanosensory transduction by identifying invariant directions in stimulus space. *Neurocomputing* 52–54:525–530.

weitere

- Gollisch, T. and Herz, A. V. M. (2004). Input-driven components of spike-frequency adaptation can be unmasked *in vivo*. *J Neurosci*, in press.
- Gollisch, T. and Herz, A. V. M. (2004). Identification of sensory transduction chains *in vivo*. *Submitted for publication*.
- Schaette, R., Gollisch, T., and Herz, A. V. M. (2004). Spike-train variability in auditory neurons *in vivo*: Dynamic responses follow predictions from constant stimuli. *Submitted for publication*.
- Machens, C. K., Gollisch, T., Kolesnikova, O., and Herz, A. V. M. (2004). Optimal stimulus ensembles for efficient coding in sensory neurons. *Preprint*.

Tagungsbeiträge

- Gollisch, T., Benda, J., Schütze, H., and Herz, A. V. M. (2001). Phenomenological model for sound-intensity coding in auditory receptor neurons of locusts. *Proc of the 28th Göttingen Neurobiology Conference*, page 360.
- Gollisch, T. and Herz, A. V. M. (2002). What invariant directions in stimulus space tell us about mechanosensory transduction. *Proc Berlin Neuroscience Forum*.

- Gollisch, T., Benda, J., Schütze, H., and Herz, A. V. M. (2002). The encoding of multi-frequency sound signals in locust auditory receptors. *Soc Neurosci Abs*, No. 162.2.
- Gollisch, T. and Herz, A. V. M. (2003). Uncovering the functional dynamics of biological signal-transduction modules. *Proc Idea-Finding Symposium, Frankfurt Institute for Advanced Studies*, pages 75–84.
- Gollisch, T. and Herz, A. V. M. (2003). The “What” and “How” of temporal integration in an insect auditory system. *Proc of the 29th Göttingen Neurobiology Conference*, page 395.
- Watzl, S., Rokem, A., Gollisch, T., and Herz, A. V. M. (2003). Coding capacities of auditory receptor cells under different stimulus conditions. *Proc of the 29th Göttingen Neurobiology Conference*, page 396.
- Schaette, R., Gollisch, T., Herz, A. V. M. (2003). Variability in spike trains of locust auditory receptor neurons under constant and dynamic stimulation. *Proc of the 29th Göttingen Neurobiology Conference*, page 398.

Erklärung

Hiermit erkläre ich, dass ich die Dissertation selbständig verfasst und keine anderen als die angegebenen Hilfsmittel benutzt habe.

Berlin, 19. März 2004

